FLAME STABILITY OF AN ULTRA-LEAN PREMIXED LOW-SWIRL BURNER

by

Julio Gustavo Strahman

A thesis submitted to
the Faculty of Graduate Studies and Research
in partial fulfillment of
the requirements for the degree of
Master of Applied Science

Ottawa-Carleton Institute for
Mechanical and Aerospace Engineering

Department of Mechanical and Aerospace Engineering
Carleton University
Ottawa, Ontario, Canada
September 2007

Your file Votre référence
ISBN: 978-0-494-33669-4
Our file Notre référence
ISBN: 978-0-494-33669-4

Abstract

Stringent emissions regulations have stimulated the development of technologies for stabilizing ultra-lean premixed flames as a means of lowering flame temperatures and reducing the formation of nitrogen oxides (NO_x). One such technology is the low-swirl burner (LSB) developed by Cheng and coworkers [1-3]. A laboratory LSB was constructed, in which the inner core flow and outer annular flow are independently controlled. Stability limits of flashback and blowoff were obtained for a wide parametric range of flowrates, equivalence ratios, and swirl numbers. A forward–backward scattering 3D particle image velocimetry system (stereoscopic PIV) was employed to quantify the swirling velocity in the reactant flow and to establish the mean flame front contour positions, which are related to stability. The current results show that the LSB stabilizes a freely propagating, turbulent flame. However the main effect of swirl is not on the creation or modification of flow divergence, but on the flowfield velocity and turbulence intensity. This determines flame position and stability limits.

Acknowledgements

I would like to thank my supervisor, Dr. M. R. Johnson, for sharing his knowledge in the subject. His feedback improved the quality of my work. Funding provided by Carleton University and NSERC was appreciated. Thanks to friends and colleagues for their assistance. I am grateful to my family for their support in this endeavour. Last but not least, I thank God for giving me health and strength.

Table of Contents

Abstract iii

Acknowledgements iv

Table of Contents v

List of Tables viii

List of Figures ix

Nomenclature xiii

Chapter 1: Introduction 1

1.1 Background 1
1.2 Premixed flame stabilization 5
1.2.1 Flammability limits 6
1.2.2 Extinction 6
1.2.3 Limits of the mixture flow: liftoff, blowoff, and flashback 7
1.3 Laminar premixed flame stabilization 7
1.4 Turbulent premixed flame stabilization 10
1.5 Flame regimes 12
1.5.1 Wrinkled laminar flames 13
1.5.2 Flamelets-in-eddies 14
1.5.3 Distributed reaction zone 14
1.6 Techniques for turbulent premixed flame stabilization 14
1.7 Objective and problem definition 17

Chapter 2: Literature Review **18**

2.1 Swirling flows and swirl induced recirculating flows 18

2.1.1 Characterization of swirling flows, the swirl number *S* 19

2.1.2 Classification of swirling flows 20

2.2 Development and applications of swirling flow 21

2.2.1 Background 21

2.2.2 Development and applications of the low-swirl burner (LSB) 24

Chapter 3: Experimental study **30**

3.1 The Low-Swirl Burner (LSB) 30

3.1.1 Introduction 30

3.1.2 LSB components 32

3.2 Data acquisition and control 41

3.3 Stability maps - Methodology 43

3.3.1 Test procedure 43

3.3.2 Data point identification 44

3.4 Particle image velocity (PIV) system 48

3.4.1 Introduction 48

3.4.2 PIV system components 50

3.5 Test implementation and data processing 55

Chapter 4: Results **61**

4.1 Stability maps 61

4.2 Velocity field and flame position 67

Chapter 5: Discussion and analysis **77**

Chapter 6: Conclusions **95**

References **97**

Appendix A: Selection of screens for the settling chamber **103**

Appendix B: Nozzle contour calculation **105**

Appendix C: Mass flow controllers calibration and setup **108**

Appendix D: PIV setup **112**

D.1 General arrangement 112

D.2 Calibration 118

D.3 Experiment setup 128

D.4 Results 131

Appendix E: Uncertainty of measurements **142**

List of Tables

Table 3-1 Testing schedule for determination of stability maps 47
Table 3-2 Cameras specifications 52
Table 4-1 PIV measurements; no flame 67
Table 4-2 PIV measurements; with flame 68
Table 5-1 Parameters for corresponding flowrates 94

List of Figures

Figure 1-1 Equilibrium adiabatic flame temperature vs. Φ, air-methane, from [4] 4
Figure 1-2 Laminar burning velocity S_L vs. Φ, air-methane, from [5] 8
Figure 1-3 Regions of premixed turbulent flames, from [4, 6] 13
Figure 1-4 Stabilization in high speed flows by a bluff body, from [7, 8] 15
Figure 2-1 Schematic of a generic tangential jet type swirl burner 18
Figure 2-2 Schematic of a generic axial vane type swirl burner 19
Figure 2-3 Diffusion flame burner stabilized by swirl, from [9] 24
Figure 2-4 Freely propagating flame stabilized in divergent flow 25
Figure 3-1 Burner components 31
Figure 3-2 Burner exploded view 31
Figure 3-3 Burner with mass flow controllers setup 32
Figure 3-4 Mesh of a screen 34
Figure 3-5 Outer and inner screens 35
Figure 3-6 Turbulence plate generator 37
Figure 3-7 Inner nozzle 38
Figure 3-8 Nozzles assembly 38
Figure 3-9 Swirler R-8 (left) and R-6 (right) 39
Figure 3-10 Vanes exit angle 39
Figure 3-11 Sleeves at the exit of the burner 40
Figure 3-12 Laskin nozzle 40
Figure 3-13 Seeders and dampers 41
Figure 3-14 Mass flow controllers and seeders setup 42
Figure 3-15 LabVIEW front Panel 43
Figure 3-16 Stable flame 44
Figure 3-17 Flashback 45

Figure 3-18 Blowoff 45
Figure 3-19 In burner 46
Figure 3-20 Stability map 46
Figure 3-21 3D stereoscopic setup 48
Figure 3-22 Real and transmitted image to the CCD of the camera 49
Figure 3-23 Timing for double frame / double exposure 52
Figure 3-24 Light sheet optics 53
Figure 3-25 Resolution and representation on the screen 55
Figure 3-26 PIV setup 56
Figure 3-27 Flowfield velocities 57
Figure 3-28 Mean flame front contour; intensities on the background 58
Figure 3-29 Mean flame front contour superimposed on the 3D velocity field 58
Figure 3-30 Flow-integrated swirl number, S, at different locations in (a) reacting and (b) non-reacting flow 59
Figure 3-31 Flow integrated swirl number, S, for different geometric swirl numbers, S_g, in reacting flow 60
Figure 4-1 Flame stability regime: constant inner flow velocity 62
Figure 4-2 Flame stability regime: constant thermal input power 63
Figure 4-3 Flame stability regime: constant total flowrate 63
Figure 4-4 Flame stability regime: varied burner exit sleeve 65
Figure 4-5 Flame stability regime: varied turbulent plate generator 66
Figure 4-6 Flame stability regime: different swirler 67
Figure 4-7 Effect of swirl number, S_g, in flame position and flowfield velocity 69
Figure 4-8 Flames position as swirl changes 70
Figure 4-9 Effect of equivalence ratio, Φ, in flame position and flowfield velocity 71
Figure 4-10 Flames position as equivalence ratio, Φ, changes 72
Figure 4-11 Effect of total flowrate, Q, in flame position and flowfield velocity 73
Figure 4-12 Flames position as total flowrate changes 74
Figure 4-13 Tangential velocity component, W, for different S_g 75
Figure 4-14 Tangential velocity component, W, for different Φ 75

Figure 4-15 Tangential velocity component, W, for different Q 76
Figure 5-1 Decay of the normalized velocity component, U, for different S_g 79
Figure 5-2 Decay of the normalized velocity component, U, for different Φ 80
Figure 5-3 Decay of the normalized velocity component, U, for different Q 80
Figure 5-4 Decay of the velocity component, U, for different S_g 82
Figure 5-5 Decay of the velocity component, U, for different Φ 82
Figure 5-6 Decay of the velocity component, U, for different Q 83
Figure 5-7 Flame front contour superimposed on velocity component U 84
Figure 5-8 Radial variation of the velocity component, U, for different S_g 86
Figure 5-9 Radial variation of the velocity component, U, for different Φ 87
Figure 5-10 Radial variation of the velocity component, U, for different Q 87
Figure 5-11 Radial variation of the turbulent velocity component, u', for several S_g 90
Figure 5-12 Radial variation of the turbulent velocity component, u', for several Φ 90
Figure 5-13 Radial variation of the turbulent velocity component, u', for several Q 91
Figure 5-14 Stability regimes and design region; air-methane mixture 93
Figure B-1 Inner nozzle contour for the R-6 swirler 107
Figure C-1 MFC calibration curves 111
Figure D-1 Images of tracers 117
Figure D-2 Seeded flow without the presence of flame 118
Figure D-3 Seeded flow in the presence of flame 118
Figure D-4 Effect of pixel size and field of view on the resolution 120
Figure D-5 Rotational PIV system with Scheimpflug criterion 122
Figure D-6 Imaging from both cameras during calibration 124
Figure D-7 Marks found on a calibration plate image 126
Figure D-8 Sheet light orientation during calibration 127
Figure D-9 Correction for light sheet misalignment, from [10] 127
Figure D-10 Raw image 132
Figure D-11 Corrected image 132
Figure D-12 Image after filtering 134
Figure D-13 Image after first binarization 135

Figure D-14 Images averaging 136
Figure D-15 Image after second binarization 137
Figure D-16 Final flame position 138
Figure D-17 Vector calculation with 50% overlap 138
Figure D-18 Multipass iteration to increase accuracy 139
Figure D-19 Correlation map at one point of the flowfield 140

Nomenclature

a	Screen mesh opening, or fluid acceleration
A	Area of an element of flame surface, or burner cross sectional area
A'	Geometric coefficient of the screen mesh
$\overline{A}$	Time-smoothed flame area
A_j	Tangential jets total area
B_i	Bias component of uncertainty
B_M	Parameter to calculate S_L, (eq.1-14)
B_2	Parameter to calculate S_L, (eq.1-14)
$B.R.$	Blockage ratio
C	Particles density number
C_p	Specific heat at constant pressure
d	Bluff body diameter, or diameter of wires in the mesh
d_A	Air tube inner diameter (ref. 9)
d_e	Particle image on the recording plane
d_F	Fuel tube inner diameter (ref. 9)
d_p	Particle diameter
dt	Time delay between two pulses in PIV
d_x	Pixel size
dx	Integer displacement in the x direction in PIV
dy	Integer displacement in the y direction in PIV
D	Cross sectional diameter of a passage, or burner diameter
Da	Damköhler number
Da^{-1}	Inverse Damköhler number (ref. 9)
D_{IW}	Interrogation window size
$f^{\#}$	f number of the lens system
F_i	In-plane loss of particle pairs
F_o	Out-of- plane loss of particle pairs
g	Gravitational acceleration
G_{ang}	Axial flux of the angular momentum
G_x	Axial flux of linear momentum (axial thrust)
I	Image intensity
k	Flame stretch factor, or turbulence kinetic energy
K	Pressure loss coefficient
Ka	Karlovitz number (also known as Karlovitz flame stretch factor)
Ka_c	Stretch due to curvature
Ka_s	Stretch due to strain

L	Characteristic length of the recirculation zone, or burner exit sleeve length, or nozzle length
Le	Lewis number
l_k	Kolmogorov turbulent length scale
l_o	Integral turbulent length scale
$\dot{m}$	Mass flowrate
M	Third-body collision partner, or mesh wires spacing (pitch), or lens magnification factor
Mn	Camera magnification
n	Order of the chemical reaction, or exponent for the formula of k, or size of the interrogation window in pixels, or number of images
N	Number of measurements
N_I	Particles image density
N_S	Particles source density
P	Pressure
P_i	Random component of uncertainty
P_{th}	Thermal input power
$P1,P2$	Correlation peaks (PIV)
Q	Volumetric flowrate, or peak ratio (PIV)
r	Radius as a variable (coordinate), or result of experiments
r_j	Radial location of the jets of the tangential jet type swirl burner
R	Radius of the burner, or spatial resolution of the PIV flowfield
Re	Reynolds number
Re_T	Turbulent Reynolds number
R_h	Radius of the hub of the axial vane type swirl burner (central core)
R_i	Radius of the nozzle at the inlet
R_{joint}	Radius of the nozzle at the joint point between the two cubics
R_o	Radius of the nozzle at the outlet
s'/s	Magnification factor
S	Swirl number
S_g	Geometric swirl number
S_L	Laminar flame speed (burning velocity)
S_L^o	Unstretched laminar flame speed
S_T	Turbulent flame speed (burning velocity)
t	Time
T	Temperature
u',v',w'	Turbulent velocity components on the axial, radial and tangential directions, respectively; equal to the rms of the respective fluctuating velocity component
U	Axial velocity component, or mean axial velocity component, or uncertainty of measurements
U_A	Axial air velocity at the throat of the burner, (ref. 9)
U_{CL}	Axial velocity of reactants on centerline, (ref. 9)
U_F	Axial fuel velocity at the fuel exit tube, (ref. 9)
U_g	Gravitational induced velocity
U_i	Inner axial velocity on the vane type and jet type swirl burners

U_j	Axial velocity on centerline induced by the fuel jet only, (ref. 9), or axial velocity through the jets on the jet type swirl burner
U_o	Outer axial velocity on the vane type swirl burner
U_p	Particle velocity
U_{RZ}	Vortex velocity (characteristic recirculation zone velocity), (ref. 9)
U_s	Lag velocity of the particle
U_v	Axial velocity on centerline induced by the recirculation vortex, (ref. 9)
U_∞	Reference velocity, or average velocity
U_θ	Characteristic angular velocity of air at the throat, equal to $U_A S$, (ref. 9)
$U_{\theta,C}$	Critical angular velocity at throat to create a recirculation zone, (ref. 9)
V	Radial velocity component
$\overline{V}$	Local velocity vector in PIV
W	Tangential velocity component
x	Axial coordinate, or distance from the screen
x_o	Empirical effective origin
X_1, X_n	Measured variables
Y_{dil}	Mass fraction of the diluents in the mixture

Greek Symbols

α	Thermal diffusivity, or exit angle of the swirler vanes, or jets angle, or angle between the lens and image planes
α_F	Thermal diffusivity of the fuel, (ref. 9)
α_S	Thermal diffusivity of the stoichiometric fuel-air mixture at the adiabatic flame temperature, (ref. 9)
β	Pressure exponent to calculate S_L, (eq.1-13), or porosity of a screen mesh
γ	Temperature exponent to calculate S_L, (eq.1-13)
δ_L	Laminar flame thickness
δ_L^o	Unstretched laminar flame thickness
$\delta(z)$	Depth of field
$\overline{\Delta X}$	Particle displacement (particle image shift) in PIV
ΔP	Pressure drop
Δz_o	Length of the volume containing particles
ΔT	Temperature difference for mass flow controllers
θ	Angle between the camera axis and the perpendicular to the object plane
θ_s	Mass fraction of the fuel for a stoichiometric mixture, (ref. 9)
λ	Wavelength of light
μ	Dynamic viscosity
ν	Kinematic viscosity
ρ	Density
σ	Solidity of the screen mesh
τ_s	Relaxation time
Φ	Equivalence ratio

Φ_M	Parameter to calculate S_L, (eq 1-14)
ψ	Stoichiometric air-to-fuel mass ratio, (ref. 9)

Subscripts

A	Air
ad	Adiabatic
avg	Average
b	Burned
c	Curvature
chem	Chemical
d	Downstream
F	Fuel
g	Gravitational
i	Inner
j	Jet
L	Laminar
o	Outer
p	Particle
ref	Reference state
s	Strain, or stoichiometric, or for lag velocity
T	Turbulent
u	Unburned, or upstream

Abbreviations

CCD	Charge-coupled device
DAQ	Data acquisition
FFT	Fast Fourier Transform
FGR	Flue gas recirculation
FOV	Field of view
GCF	Gas conversion factor
HSI	High-swirl injector
IW	Interrogation window
LSB	Low-swirl burner
LSI	Low-swirl injector
MFC	Mass flow controller
ppm	Parts per million (by volume)
PDF	Probability density function
PTU	Programmable timing unit
PIV	Particle image velocimetry
rms	Root-mean-square
slpm	Standard liters per minute
VI	Virtual instrument

Chapter 1: Introduction

1.1 Background

In 2006, the International Energy Agency reported that approximately 81 percent of the energy used on the planet came from the combustion of fossil fuels, including 21 percent from natural gas, 35 percent from oil and 25 percent from coal [11]. The major pollutants emitted by combustion are unburned hydrocarbons, nitrogen oxides (NO_x), carbon monoxide (CO), sulphur oxides (SO_2 and SO_3), soot and particulate matter [4]. NO_x gases include NO (nitric oxide) and NO_2 (nitrogen dioxide). Stringent regulations, specifically for NO_x emissions, encouraged the development of devices such as the ultra-lean premixed Low-Swirl Burner (LSB) [12].

In combustion, the primary nitrogen oxide is NO, and its formation occurs through a combination of the following four mechanisms [4, 13]:

1. The thermal, or Zeldovich, mechanism governs in high-temperature combustion and over a wide range of equivalence ratios, Φ. It becomes important above 1800 K and is the main NO formation mechanism beyond 2500 K [14]. Comparing time scales of fuel oxidation processes, this is a slow mechanism, although the reaction rate is exponentially dependent on temperature. It is a three step chain reaction:

$$O + N_2 \Leftrightarrow NO + N \qquad 1\text{-}1$$

$$N + O_2 \Leftrightarrow NO + O \quad 1\text{-}2$$

$$N + OH \Leftrightarrow NO + H \quad 1\text{-}3$$

2. The prompt, or Fenimore, mechanism is important in rich combustion. It dominates the rate of NO formation for temperatures below 2000 K [14]. The steps of this mechanism are

$$CH + N_2 \Leftrightarrow HCN + N \quad 1\text{-}4$$

$$C + N_2 \Leftrightarrow CN + N \quad 1\text{-}5$$

$$HCN + O \Leftrightarrow NCO + H \quad 1\text{-}6$$

$$NCO + H \Leftrightarrow NH + CO \quad 1\text{-}7$$

$$NH + H \Leftrightarrow N + H_2 \quad 1\text{-}8$$

$$N + OH \Leftrightarrow NO + H \quad 1\text{-}9$$

Reactions 1-6 to 1-9 correspond to equivalence ratios up to 1.2. From this point, more complex chemistry takes place [4, 13].

3. The N_2O-intermediate mechanism is important in lean combustion, (equivalence ratio $\Phi < 0.8$) and low temperature conditions. It follows these reactions,

$$O + N_2 + M \Leftrightarrow N_2O + M \quad 1\text{-}10$$

$$H + N_2O \Leftrightarrow NO + NH \quad 1\text{-}11$$

$$O + N_2O \Leftrightarrow NO + NO \quad 1\text{-}12$$

where M may be any molecule, referred as a third-body collision partner.

At lean conditions and low temperatures, thermal and prompt emissions are minimized [14]; however, due to the low activation energy required for reaction 1-10, the formation

rate of NO through the recombination of N_2O is unaffected by a lower temperature. An increase in pressure and air concentration favours this mechanism [15].

4. For fuels with bound nitrogen, the nitrogen recombines to form HCN (hydrogen cyanide) that later reacts as described in the Fenimore mechanism.

Controlling the key variables of these mechanisms, temperature, time, and composition, results in the reduction of NO. For thermal NO it is known that:

- the reaction rate for thermal NO formation, which is exponentially dependant on temperature, increases substantially above 1800 K;
- the amount of NO produced is approximately proportional to the residence time of combustion products; and
- elevated concentration of O-atoms, e.g., orders of magnitude greater than equilibrium concentration, substantially increases NO formation rates [4]. For adiabatic combustion, at either constant volume or pressure, the maximum equilibrium oxygen O-atom mole fraction required to form NO, is near an equivalence ratio of 0.9.

The prompt mechanism is faster than the thermal mechanism, and the values of NO are very significant for rich combustion. For premixed laminar combustion at Φ=1.32, close to 95% of the NO emissions at are formed via the prompt mechanism [16]. Regarding the third mechanism, Correa and Smooke [17] show that this is the major source of NO formation in lean premixed combustion. Concerning the fourth mechanism, it is not relevant for combustion with natural gas or gasoline, which contains essentially no fuel-bound nitrogen.

Premixed combustion allows better control of temperature compared to diffusion flames. At lean conditions, excess air acts as a heat sink, significantly reducing flame temperature. An intense turbulent premixing of the fuel and oxidizer also promotes uniform composition of the fuel-air mixture, which results in a homogeneous temperature of the combustion zone. Therefore, for ultra-lean premixed combustion of natural gas, only the N_2O-intermediate path remains as a significant NO emission source.

The effect of Φ on flame temperature is appreciated in Figure 1-1. The curve was determined using the software HPFLAME, from [4].

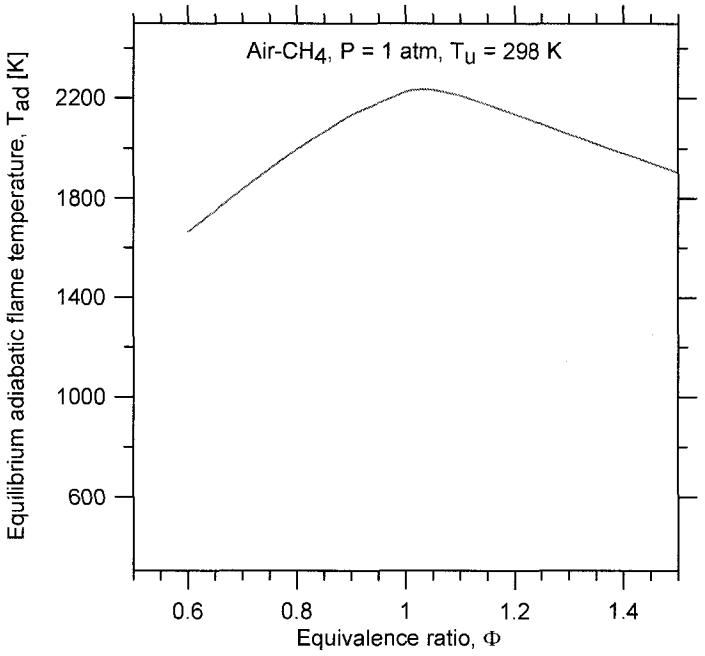

Figure 1-1 Equilibrium adiabatic flame temperature vs. Φ, air-methane, from [4]

It has traditionally been quite difficult to stabilize an ultra-lean premixed flame. One such technology that overcomes this limitation, is the LSB developed by Cheng and coworkers [1-3], which uses a weak swirling flow to stabilize a freely propagating, turbulent flame by creating flow divergence. The ultra-lean premixed LSB also

demonstrates the ability to increase the turn-down ratio of burners, which is defined as the ratio of maximum to minimum flowrates that produce stable flames.

Tests on an LSB with a 7.5 cm diameter showed NO_x emissions under 5 ppm (@ 3% O_2). Simultaneous emissions of less than 10 ppm CO and less than 15 ppm of NOx were achieved. The studies corresponded to atmospheric conditions, equivalence ratios from 0.58 to 0.95, and thermal inputs from 210 to 280 kW (average flow velocity U_∞ of 20 m/s) [18]. Johnson et al. [3] tested the concept of the LSB applied to gas turbine operating conditions ($20 < U_\infty < 50$ m/s; $230 < T_{inlet} < 430$°C; $6 < P_{inlet} < 15$ atm) with values of NO_x under 5 ppm (@ 15% O_2). In contrast with high-swirl burners, the flowfield of the LSB did not present the large dominant recirculation zone, which increases the residence time of the products and, accordingly, the NO emissions.

1.2 Premixed flame stabilization

In practical combustors, it is desirable to have a device that produces a particular type of flame, located at a certain position, under prescribed operational conditions. The term "stability" is used rather loosely in combustion science [19]. On some occasions, it describes the range of fuel-air ratios over which combustion can be obtained; in other cases it refers to a measure of the maximum air flowrate or velocity that the system can accept before flame extinction.

In general, flame stability includes

- Flammability limits.
- Extinction.
- Stability limits of the mixture flow, including liftoff, blowoff and flashback.

1.2.1 Flammability limits

For certain values of pressure and temperature, flammability limits identify the fuel-oxidizer mixture ratios, beyond which no flame will propagate [20]. The lower limit corresponds to the leanest mixture (Φ <1) and the upper limit describes the richest mixture (Φ>1). The values of these limits are determined experimentally and have been shown to be a function of the equipment characteristics. Hence, in spite of the fact that these limits depend on the fuel-oxidizer properties, they are not fundamental properties of the mixture.

1.2.2 Extinction

Flame extinction occurs due to thermal, chemical, or aerodynamic effects. Thermally induced extinction occurs when there is excessive heat loss from the flame and happens with the addition of diluents or when a flame passes through a narrow opening and loses heat to the walls. This latter example is known as quenching. The loss of heat and radicals (chain carriers) to the wall reduces the reaction rate, hindering flame propagation. The maximum value of the section that arrests flame propagation under specific parameters (fuel type, equivalence ratio, fuel velocity, burner geometry) is the quenching distance. Chemically induced extinction occurs through the addition of chemical components so as to eliminate radicals of the reactions.

Aerodynamics effects and the subsequent stretching of a flame lead to its extinction, in appreciable velocity gradients. Karlovitz et al. [21] performed one of the first studies of this phenomenon. Later, Lewis and Von Elbe al. [22] analyzed the stabilization of a flame above a burner rim and showed that the flame blows off when the flow velocity of

the mixture exceeds the burning velocity. They verified the opposite for the flashback condition.

1.2.3 Limits of the mixture flow: liftoff, blowoff, and flashback

Two of the major concerns in the design of a burner is to avoid the occurrence of flashback, and liftoff. Flashback occurs when the flame propagates upstream into the burner tube without quenching [4]. This can ignite the volume of the gas contained in the mixer, and may produce an explosion. Often, during burner shut-down, the reduction of the flow velocity allows flashback to occur.

In a conventional burner, liftoff occurs when the flame detaches from the burner and positions itself at some distance downstream. Typically, if the local burning velocity is lower than the mixture flow velocity everywhere along the flame, the flame lifts. For a classical burner, any small change to the flow in the vicinity of a lifted flame can further displace the flame and lead to blowoff. This occurs when the flame propagates far enough downstream that it extinguishes.

1.3 Laminar premixed flame stabilization

For a laminar flame to be stable the laminar speed, S_L, must equal the local fuel-air flow velocity, which is normal to the flame front [14]. The unstrained, one-dimensional laminar flame speed is a fundamental parameter in premixed combustion science, and for a given fuel type it varies strongly with temperature and pressure. One of the most accepted correlations for S_L is from Metghalchi and Keck [23], and is

$$S_L = S_{L,ref} \cdot \left(\frac{T_u}{T_{u,ref}} \right)^{\gamma} \cdot \left(\frac{P}{P_{ref}} \right)^{\beta} \cdot \left(1 - 2.1 \cdot Y_{dil}\right) \qquad 1\text{-}13$$

where $S_{L,ref}$ is given by

$$S_{L,ref} = B_M + B_2 \cdot (\Phi - \Phi_M) \qquad 1\text{-}14$$

The values of the constants γ and β are functions of the equivalence ratio, Φ, and the values for B_M, B_2, and Φ_M depend on the type of fuel. T_u is the temperature of the unburned mixture and the correlation is valid for $T_u \geq 350$ K. The reference values for temperature, T, and pressure, P, are 298 K and 1 atm, respectively. The term Y_{dil} is the mass fraction of the diluents in the mixture, e.g., recirculated combustion products. Figure 1-2, calculated from [5], shows the effect of Φ on S_L, for an air-methane mixture.

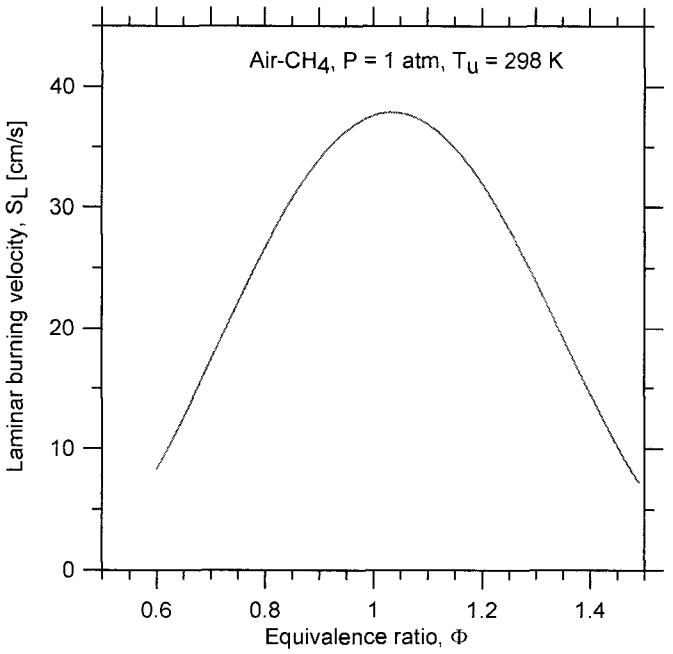

Figure 1-2 Laminar burning velocity S_L vs. Φ, air-methane, from [5]

As this graph shows, Φ influences S_L, which has a major impact in the stabilization phenomenon. Varying Φ, allows flame stability under different flows regimes.

Other important parameters in premixed combustion are the flame stretch factor k and the Karlovitz number Ka, which characterize aerodynamic factors that influence the

flame; these are namely flow non-uniformity, flame curvature, and unsteadiness [15]. Flame stretching occurs when there are strong velocity gradients in the reactant stream, so that a flame propagating in the non-uniform flow is affected by strain and curvature that lead to changes in the frontal area.

The flame stretch factor, k, is defined as the relative rate of change of flame surface area

$$k = \frac{1}{A}\frac{dA}{dt} \qquad 1\text{-}15$$

where A is the area of the element of flame surface and dA/dt is its rate of change. Since it has units of [1/seconds], k is the reciprocal of the characteristic time for flame stretching. Positive stretch reduces the flame thickness, and increases reactant consumption per unit of area. High values of stretch may lead to extinction [20]; hence, stretch is directly related to flame stabilization. The Karlovitz number is defined as

$$Ka = k\frac{\delta_L^\circ}{S_L^\circ} \qquad 1\text{-}16$$

where δ_L° and S_L° are the unstretched laminar flame thickness and burning velocity respectively. Since the ratio $\delta_L^\circ / S_L^\circ$ represents the time for the gases to pass through the unstretched flame, Ka is the ratio of two times:

$$Ka = \frac{\text{Transit time of the gases across the flame}}{\text{Flame stretching characteristic time}} \qquad 1\text{-}17$$

Sometimes this factor is written as a function of two terms, one due to strain denoted with the subscript (s) and the other due to curvature, with the subscript (c) [14]:

$$Ka = Ka_s + Ka_c \qquad 1\text{-}18$$

1.4 Turbulent premixed flame stabilization

For the combustion process to take place, fuel and oxidizer must mix at the molecular level. Turbulence, by facilitating the mixing process, greatly accelerates the combustion process, since molecular mixing happens at the interface between small eddies [24]. LeChâtelier and Mallard saw this during the late 1800's; however, the research by Damköhler provides concrete results of turbulent flame speed, S_T, as a function of Reynolds numbers [25]. Damköhler realized that the small eddies increase the transfer rates of heat and mass within the wave, so S_T should be higher than S_L [22]. The turbulent flame speed, S_T, is commonly defined as [4]

$$S_T = \frac{\dot{m}}{\overline{A}\,\rho_u} \qquad 1\text{-}19$$

where $\overline{A}$ is the time-smoothed flame area, $\dot{m}$ is the reactant mass flowrate, and ρ_u is the unburned gas density.

The reaction zone in a turbulent flame is quite thin; in the order of 1 mm for hydrocarbon-air flames [20]. However, the mean turbulent flame brush, which includes the different positions of the instantaneous flame, is considerably thicker. From many studies an expression for S_T as a function of S_L is available. In general, from theoretical and experimental results [20]:

- S_T is always greater than S_L.
- S_T increases with augmentation of turbulence upstream of the flame.
- In some experiments S_T shows insensitivity with respect to the turbulence scale of the approaching flow.

- The variation of S_T is similar to that of S_L. It is common to see data of S_T normalized by S_L.

The first model for S_T was given by Damköhler [26]:

$$S_T = S_L + u' \tag{1-20}$$

where u' is the turbulent component of velocity (root-mean-square of the fluctuating velocity component, U). Of the expressions for S_T, one of the most recent, by Peters [27], is

$$\frac{S_T}{S_L} = 1 - \frac{0.39}{2}\frac{l_o}{\delta_L}\left[\left(\frac{0.39}{2}\frac{l_o}{\delta_L}\right)^2 + 0.78\frac{u' l_o}{S_L^o \delta_L}\right]^{\frac{1}{2}} \tag{1-21}$$

where l_o represents the integral turbulent length scale, δ_L is the laminar flame thickness, and S_L^o is the burning velocity of the unstretched planar flame. Plessing et al. [28] measured values of S_T, for different intensities of turbulence and various air-methane lean flames stabilized by low swirl. The theoretical equation was in good agreements with the experimental results.

A second critical parameter in turbulent combustion is the Damköhler number Da defined as

$$Da = \frac{\text{Characteristic flow or mixing time}}{\text{Characteristic chemical time}} = \frac{t_{flow}}{t_{chem}} \tag{1-22}$$

For fast chemical reactions, $Da >> 1$, and increases as turbulence decreases. The definition as in [4] in terms of flame parameters, is

$$Da = \frac{(l_o/u')}{(\delta_L/S_L)} = \left(\frac{l_o}{\delta_L}\right)\left(\frac{S_L}{u'}\right) \tag{1-23}$$

As cited by Glassman [20], Klimov [29] and Williams [30] demonstrate that laminar flame propagation exists in turbulent flow when the *Ka* number is less than unity. According to [20], the Karlovitz number for stretch in turbulent flames is

$$Ka = \left(\frac{\delta_L}{l_k}\right)^2 \qquad 1\text{-}24$$

where l_k is the Kolmogorov turbulent length scale. Hence, the condition for the existence of laminar flames in turbulent flow is

$$\delta_L \leq l_k \qquad 1\text{-}25$$

When the effect of stretch wrinkles a flame, the total flame surface area $A_{flamelets}$, increases. If the local flame speed remains constant and equal to S_L, then for a certain value of turbulent burning rate, $\overline{A}\, S_T = A_{flamelets}\, S_L$ [4]. This relationship explains the fact that S_T is higher than S_L. Another definition for the Karlovitz number is provided by Peters, [24],

$$Ka = \left(\frac{u'}{S_L}\right)^{3/2}\left(\frac{\delta_L}{l_o}\right)^{1/2} \qquad 1\text{-}26$$

Glasmann [20], analyzes the effect of stretch and also describes another fundamental instability. It derives from the difference between mass and heat diffusivities through the flame, and yields a non-unity Lewis number, *Le*.

1.5 Flame regimes

Visualization of flame propagation suggests that the primary effect of turbulence is to wrinkle the flame front. The relationship between δ_L, l_k (smallest eddies), and l_o (largest eddies), controls the structure of the turbulent flame.

Turbulent flames can be classified as

- Wrinkled laminar flames: $\delta_L \leq l_k$,
- Flamelets-in-eddies: $l_o > \delta_L > l_k$,
- Distributed reactions: $\delta_L > l_o$.

A log-log plot of *Da* versus the turbulent Reynolds number, Re_T, illustrates these flame regimes.

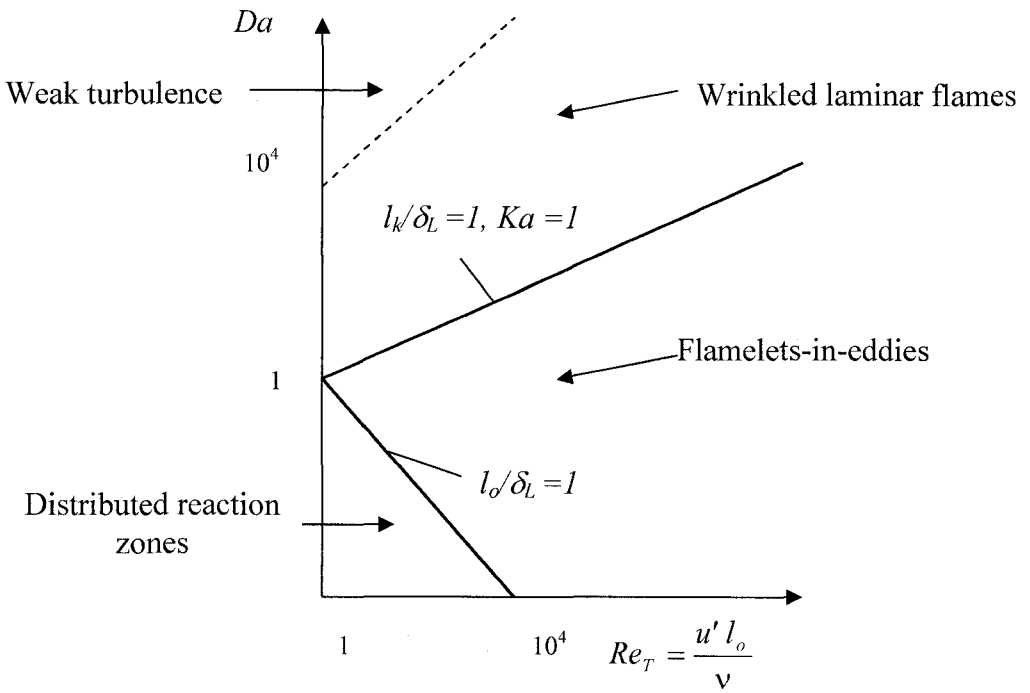

Figure 1-3 Regions of premixed turbulent flames, from [4, 6]

1.5.1 Wrinkled laminar flames

Wrinkled laminar flames, also known as reaction sheets, occur when the reaction takes place in thin sheets. Mathematically, this takes place for Damköhler numbers higher than unity. Physically, this indicates that in this regime the chemical reactions occur relatively quickly and the area of the flame limits flame propagation, which fluid mixing enhances.

1.5.2 Flamelets-in-eddies

In the flamelets-in-eddies regime (sometimes called mixed mode), the combustion burning rate depends on the eddy turnover time u'/l_o. The eddy-breakup concept attempts to explain the phenomenon, considering that the rate of combustion increases when pockets of unburned reactants are broken down (more rapidly) into smaller pockets, that increases the area of contact between hot gases and unburned reactants [4]. The basic idea is that turbulent mixing governs combustion rates, rather than chemical reaction rates.

1.5.3 Distributed reaction zone

Within a distribute reaction zone, all turbulent length scales can be found. The flame loses coherence and the area is thick with reactant eddies immersed in the products [31]. For combustion to exist in this regime, the Damköhler number should be small ($Da < 1$), and reaction times must be longer than eddy lifetimes. In practice, distributed reaction zones are very difficult, if not impossible, to achieve.

1.6 Techniques for turbulent premixed flame stabilization

Turbulent premixed flames are essential to many practical applications including gas burners, gas turbine combustors, and spark-ignition engines. In some cases, pilot flames are used. Nevertheless, the use of recirculating combustion products into the zone of the fresh mixture is sometime preferable, as the mixture self-ignites. This is done especially for fast turbulent flow [20]. A well known method to attain this type of stabilization is by the use of a bluff body that interferes with reactant flow. Sudden expansions in the flow

duct region, as in the so-called dump combustor [7, 20], also generates separation and recirculation.

Solid obstacles in the stream (bluff body stabilization)

These devices create a strong recirculation zone downstream, behind the flame holder. Theoretical models are consistent with the principle that recirculating hot gases liberate a critical amount of energy towards the unburned mixture. The blowoff velocity value is given by [4]

$$U_{blowoff} = 2\rho_b L\left(\frac{S_L^2}{\rho_u \alpha_T}\right) \qquad 1\text{-}27$$

where ρ_u and ρ_b are the unburned and burned gas densities respectively, L is a characteristic length of the recirculation zone, and a_T is the turbulent thermal diffusivity. Figure 1-4 illustrates the system.

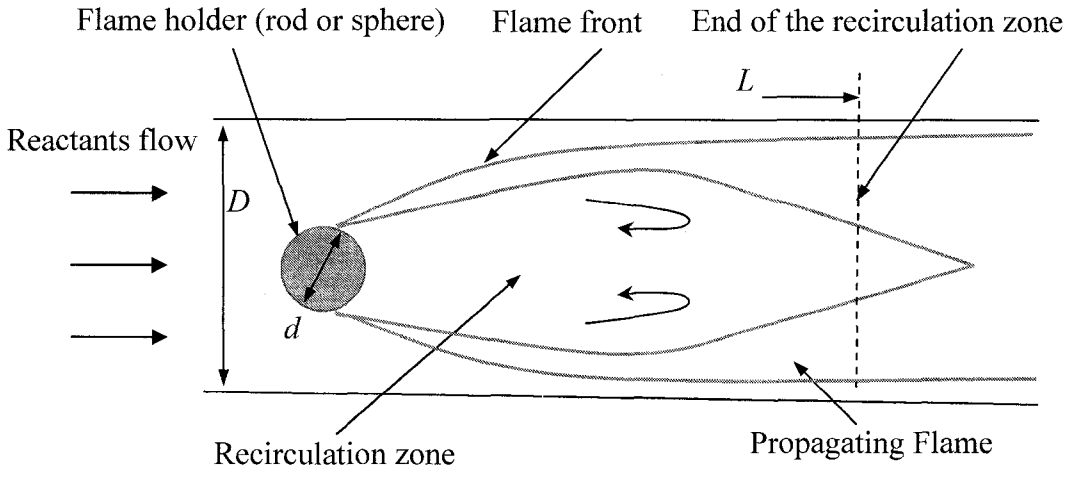

Figure 1-4 Stabilization in high speed flows by a bluff body, from [7, 8]

In many cases, multiples bodies are in the same combustion chamber to hold the flame. This reduces the length of the combustion zone; however, a trade-off is that they increase the pressure loss, which is already produced by burning. The physics behind a bluff body and the recirculation zone can be explained as follows [32, 33]: from the solid surface of the blockage, the reactants flow velocity U increases outward with a distribution according to a certain gradient from the boundary of the object. Therefore, the combustion wave stretches. Then heat, which diffuses out of an element of the wave, does not return to the same element due to the convection effects. However, the heat reservoir of the recirculation zone compensates for the heat loss, which avoids blowoff. Under the assumption that the vortex region of the wake is "well stirred" it is shown that for the blowoff (or extinction) velocity [32]

$$\frac{U_{extinction}}{P^{n-1}d} = constant \qquad 1\text{-}28$$

where p is the pressure of the gas, d is the diameter of the body, and n is the order of the chemical reaction [32]. In consequence, the blowoff velocity increases with the diameter of the body. Experiments show that the major influence of the blockage ratio $B.R.=(d/D)^2$, is on the length of the recirculation zone [32].

The comparison of the fluid mechanics of the cold flow past a cylinder with that of the combustion products [20], shows that in the last case, instead of having eddies being shed in the wake, a well-defined steady vortex takes place. This change is believed to be caused by the reduction of the turbulent Reynolds number, due to the decrease in kinematic viscosity, generated by the temperature rise [20]. Bovina, [34], cited by Beér and Chigier, [32], concludes that the residence time of particles in the recirculation zone

increases up to eight times due to combustion, and is independent of the mixture ratio. These observations show that this method of flame stabilization does not reduce NO production. Bespalov [35] also shows that with combustion, stability limits increase with a rise in the initial and final temperature of the mixture. However, as explained previously, a rise in temperature favours the thermal NO formation mechanism.

1.7 Objective and problem definition

Although the LSB is successful in a variety of industrial applications, choosing the burner geometry (e.g. diameter ratio of inner core and outer annulus, turbulence level, and swirl vane angle) and appropriate operating conditions (e.g. rate of swirl and exit velocities) remains a largely empirical process. It is also apparent that the swirl number, S, developed by Beér and Chigier [32], does not alone define a range of flame stability. This motivated a three-dimensional study of the flowfield stabilized by the LSB, with a particle image velocimetry system in 3D also known as stereoscopic PIV.

The objectives of this study are twofold. The first is to investigate scaling parameters and guidelines for the optimal design of LSBs, from laboratory to industrial size. The second is to understand better the stabilization phenomenon, for the LSB and for subsequent applications as well. This continues the research by Johnson et al. [3] on low emission gas turbines, where typical production high-swirl injector (HSI) for gas turbine combustors were modified to operate in a novel low-swirl mode (LSI).

Chapter 2: Literature Review

2.1 Swirling flows and swirl induced recirculating flows

Swirling flows have been widely used in industrial burners, furnaces, and gas turbine combustors to improve blowoff characteristics, ignition stability, mixing enhancement, flame stabilization, and pollutant reduction [36]. Figure 2-1 represents a swirl burner where tangential jets inject part of the mixture. Due to the rotary motion, the resultant velocity vector of the fluid leaving the burner has a tangential component besides the radial and axial components [32]. This process creates a low pressure region in the core along with adverse pressure gradients in the radial and axial directions. If the value of the swirl is sufficiently high, the flow reverses its direction and generates a recirculation zone.

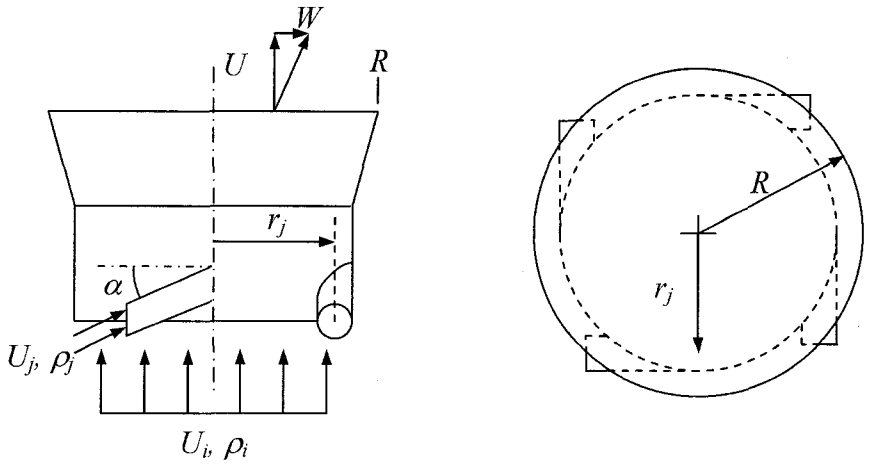

Figure 2-1 Schematic of a generic tangential jet type swirl burner

2.1.1 Characterization of swirling flows, the swirl number *S*

Possibly the most common definition of the swirl number, *S*, as a non-dimensional criterion of swirl intensity, was proposed by Chigier and Beér [37],

$$S = \frac{\text{axial flux of angular momentum}}{\text{axial thrust} \cdot R} = \frac{G_{ang}}{G_x \cdot R} \qquad 2\text{-}1$$

where G_{ang} is about the axis of the burner, R is the throat radius of the burner, and G_{ang} and G_x are the radial integrals over a plane perpendicular to the burner axis. The swirl number, *S*, can be determined via the integration of the velocity field according to:

$$S = \frac{\int_0^\infty \rho U W r^2 dr}{R \int_0^\infty \rho\left(U^2 - \frac{1}{2}W^2\right) r dr} \qquad 2\text{-}2$$

where U and W are axial and tangential (angular) velocity components and ρ is the fluid density. In general, it is more convenient to define a geometric swirl number, S_g, for a particular burner based on measured inlet conditions or flows, and take into account the geometry of the burner. Vanes can also create swirling flows as in Figure 2-2.

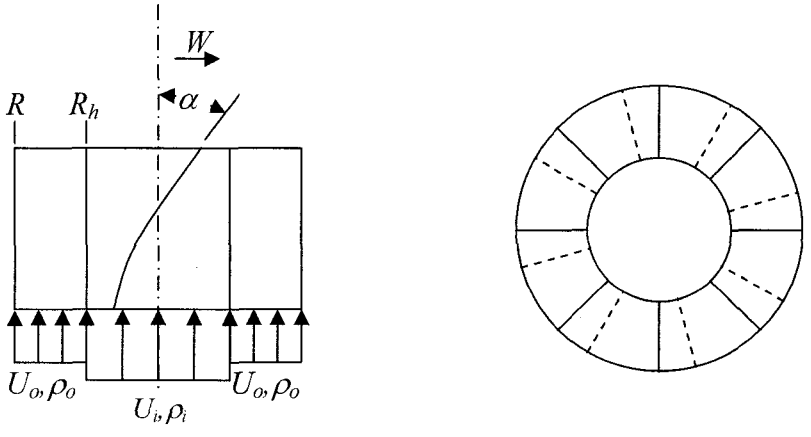

Figure 2-2 Schematic of a generic axial vane type swirl burner

The following equations, as Johnson proposed [38] for the value of S_g, consider both possibilities. For the jet type swirler,

$$S_g = \frac{\pi r_j R \dot{m}_j^2 \cos\alpha}{\left(\dot{m}_i + \dot{m}_j\right)\left(\dot{m}_i \frac{\rho_j}{\rho_i} + \dot{m}_j\right) A_j} \qquad 2\text{-}3$$

where $\dot{m}_i$ and $\dot{m}_j$ are the mass flowrates and A_j is the total area of the tangential jets.

In the case of the vane type swirl burner,

$$S_g = \frac{\frac{2}{3}\tan\alpha\left(1 - \frac{R_h^3}{R^3}\right)}{\left(1 - \frac{R_h^2}{R^2} + \frac{\rho_i U_i^2}{\rho_o U_o^2}\frac{R_h^2}{R^2}\right)} \qquad 2\text{-}4$$

2.1.2 Classification of swirling flows

Beér and Chigier [32] divided flows according to the degree of swirl in two groups: flows of weak swirl for S up to 0.6, and strong swirl above this value.

For weak swirl flows, the low axial pressure gradient is not strong enough to cause recirculation of the flow. However, in high swirl flows, the adverse pressure gradient along the flow axis is large enough to overcome the kinetic energy of the fluid particles, and creates a recirculation zone with a shape of a toroidal vortex. Combustion stability uses this mechanism, due to the fact that the recirculating flow acts as a heat reservoir of the active species, which constantly reignites the fresh mixture. The nature of the method is similar to that of bluff body stabilization previously described.

2.2 Development and applications of swirling flow

2.2.1 Background

In their work, Feikema et al. [9] investigated blowoff limits of non-premixed (diffusion) flames stabilized by large amounts of swirl. The theoretical analysis presents an extension towards swirling flow; regarding previous non-swirling flame blowoff theory. Experimentally, blowoff data was collected and collapsed to a single general curve. Instead of the classical swirl number *S*, Feikema and coworkers present an inverse Damköhler number, based on swirl velocity as the governing parameter, to define stability. The generality of their conclusion derives from data obtained for different fuel types and burner geometries.

Aspects of Feikema's approach and conclusions are applicable to the design of premixed low-swirl burners, and contribute to our research.

For their study, flame blowoff included three cases:

- The excessive fuel velocity limit (or rich limit).
- The excessive swirl and or air velocity (or lean limit).
- The minimum swirl limit that eliminates the recirculation zone.

This study summarizes the effect of swirl as [9],

- Swirl increases the turbulent burning velocity of the base of a lifted flame so it can accept an increase in fuel jet velocity without blowoff. This is due to the increase in the local velocity fluctuation and the creation of more local premixed regions.

- The recirculation vortex is a heat source moving hot products upstream to mix with reactants. Excessive swirl entrains cool surrounding air with the opposite effect.
- The effect of swirl is similar to that of bluff body flame holders, due to the presence of stagnation points.
- Excessive swirl greatly increases the rate of strain on a flame due to an increase in velocity gradients, and causes blowoff.

Kalghatgi [39], in his work, formulated the first blowoff theory for non-swirling flow. He postulates a dimensionless parameter for blowoff that includes the fuel velocity U_F, directly related to the heat release of the burner. Kalghatgi considers that flame blowoff occurs when the local gas velocity of the reactants close to the centerline U_{CL}, is higher than the local turbulent burning velocity, S_T, of the flame base, assuming the flow is already partially premixed. The non dimensional relation for the blowoff velocity U_F is

$$\frac{U_F/d_F}{S_L^2/\alpha_F} = 0.017\left(\frac{\alpha_F}{\nu_F}\right)\left(\frac{\rho_A}{\rho_F}\right)\left[\frac{4}{\theta_S}\left(\frac{\rho_F}{\rho_A}\right)^{1/2} - 5.8\right] \qquad 2\text{-}5$$

where θ_s is the mass fraction of the fuel for a stoichiometric mixture, d_F is the fuel tube inner diameter, and α_F and ν_F are the thermal diffusivity and kinematic viscosity of the fuel. Feikema et al. [9] consider the parameter derived by Kalghatgi as an inverse Damköhler number:

$$\frac{U_F/d_F}{S_L^2/\alpha_F} = Da_{KAL}^{-1} \qquad 2\text{-}6$$

Hence, the solution of the previous equations yields the value of the velocity U_F at blowoff, if fuel-air mixture characteristics are predetermined.

The second approach given by Broadwell et al. [40] (called BDM due to the other authors names: Dahm, and Mungal), assumes that blowoff occurs when the local fluid mechanical mixing rate is higher than the chemical reaction rate. This idea also generates an inverse Damköhler number to predict blowoff:

$$\frac{U_F/d_F}{S_L^2/\alpha_F} = Da_{BDM}^{-1} \tag{2-7}$$

$$Da_{BDM}^{-1} = \frac{(1+\psi)^2}{4.8}\left(\frac{\rho_F}{\rho_A}\right)^{1/2}\frac{\alpha_F}{\alpha_S} \tag{2-8}$$

where ψ is the stoichiometric air-to-fuel mass ratio, α_S is the thermal diffusivity of the stoichiometric fuel-air mixture at the adiabatic flame temperature, and α_F is the thermal diffusivity of the fuel at the inlet temperature.

Based on the conclusions for non-swirling flows, and after experimentation on swirling flows, Feikema and colleagues arrive at a form of an inverse Damköhler number, to characterize blowoff conditions in the presence of swirling flows. Their Da^{-1} is a function of $U_\theta = U_A S$, which is the characteristic angular velocity,

$$Da_{FEIK}^{-1} = f\left\{\frac{(U_A S - U_{\theta,c})/d_A}{S_L^2/\alpha_F}\right\} \tag{2-9}$$

where U_A is the axial air velocity at the throat of the burner, and $U_{\theta,C}$ is the critical value of angular velocity to create a recirculation zone. The validity of this relation is verified through experimental data. Blowoff curves obtained for different burner geometries, fuels and swirl numbers, are found to collapse on a single linear curve. It is mentioned

that swirl allows the experimental burner to provide up to five times the heating power with the same fuel tube diameter. The physical reason is shown in Figure 2-3. Swirl increases the vortex velocity, U_{RZ}, (stabilizing), that is opposite to the fuel jet velocity, U_F (destabilizing), reducing the final axial centerline velocity U_{CL}. U_j and U_v represent the axial velocities on centerline induced by the fuel jet and the recirculation vortex, respectively.

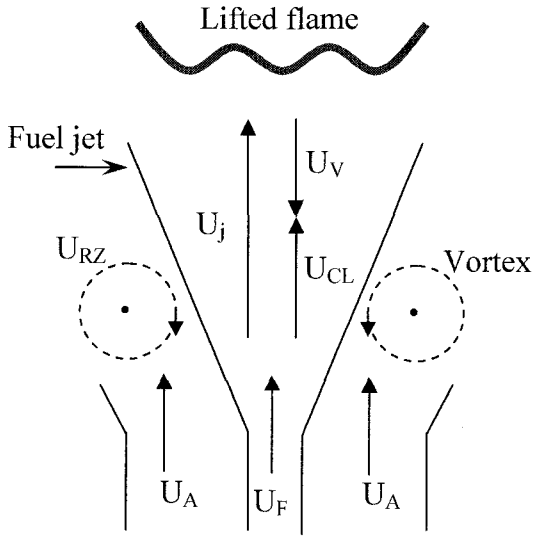

Figure 2-3 Diffusion flame burner stabilized by swirl, from [9]

2.2.2 Development and applications of the low-swirl burner (LSB)

The work of Chan et al. [1] introduced the use of weak swirl to stabilize freely propagating open premixed turbulent flames. For their experiments, they used a jet type swirl burner similar to that previously described. The most distinct characteristic that they observe is that flame stabilization is not based on flow recirculation, something typical of high swirling flows. The centrifugal forces induced by the weak swirl create radial pressure gradients that generate flow divergence at the exit of the burner. Hence, the moving flame settles where the local mass flux balances the burning rate. Chan and

colleagues verified the lack of a reversal flow area that proves that recirculation is not essential to flame stabilization. The flame zone and its properties are not affected by shear associated with swirl. The flames in their experiments show characteristics found in wrinkled laminar flames and the flame speed is based on the centerline velocity vector which is locally normal to the flame brush. Weak swirl stabilized flames are considered as freely propagating, but stationary.

Cheng [41] confirms that the stabilization mechanism of freely propagating flames in divergent flow is similar to that of stagnation flow stabilized flames, with the stagnation point far downstream of the flame zone. The operation range of the LSB is larger than other burners. The flow velocity upstream of the flame zone is higher than the flame velocity, and the flow velocity downstream is lower, which prevents flashback and blowoff. Figure 2-4 illustrates the concept:

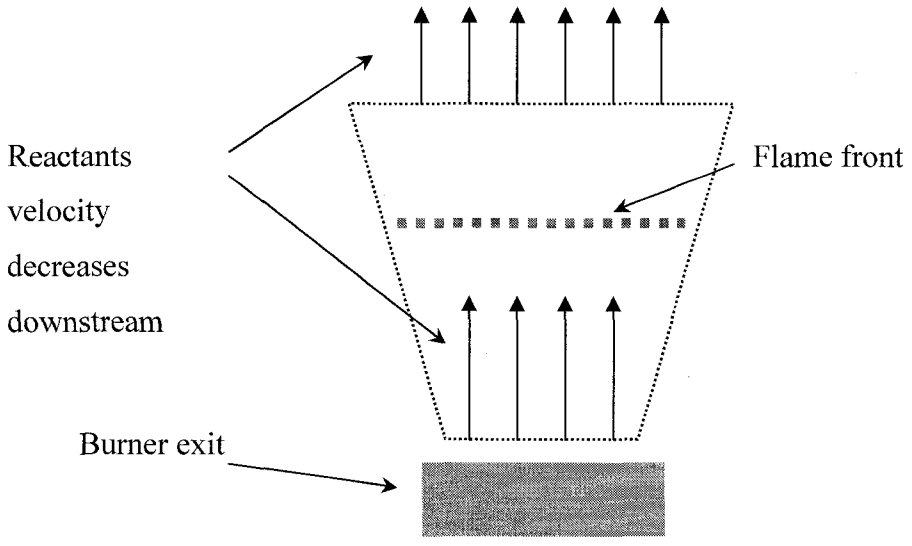

Figure 2-4 Freely propagating flame stabilized in divergent flow

Another limitation of the LSB used is a lean air-methane limit of $\Phi = 0.57$, close to the laminar flammability limit. In comparison with non-swirling flow, swirl reduces the local flow velocity, but increases the turbulent velocity component u'. The effect of Φ shows an increase in u' and in the mean axial velocity. The flames exist either in the wrinkled laminar flame zone, or in the flamelet regime, even under high levels of turbulence. In this work, the authors contemplate the hypothesis of swirl number as a parameter to define a range for flame stabilization independently of flowrates.

Bedat and Cheng [42] demonstrate the ability of the LSB to stabilize premixed flames in intense isotropic turbulence. They verify the lack of the recirculation zone and the associated mean shear. The weak swirl generates slightly divergent flow whereas the mean axial velocity decreases almost linearly. The tangential velocity component is limited to the outer annular region, which leaves the center flow undisturbed. The mean strain rates (and the stretching) are much lower, particularly because the flame is not affected by the recirculation zone.

Yegian and Cheng [2] describe their tests on the jet type LSB for practical applications. The burner radius is of 26.4 mm, and it has perforated screens with holes of 3.2 mm in diameter to generate turbulence. The LSB permits a turn-down ratio higher than 10 to 1. The exit tube varies from 20 to 120 mm. Blowoff and flashback limits are recorded on a graph of the equivalence ratio, Φ, varying with the geometric swirl number, S_g. Longer exit tubes offer a larger stability region that is attributed to the residence time that both flows (central and swirling) have for mixing. They observe that blowoff limits are insensitive to Φ, while flashback limits decrease with an increase in

Φ. The LSB operates below the threshold for the toroidal recirculation zone of $S = 0.6$. The reacting and non-reacting flow comparison verifies that the difference is mainly downstream of the flame where combustion induced flow acceleration takes place. This study also shows that an LSB adapts well to enclosures of different sizes. The LSB does not present large shear stresses in its flowfield, and Reynolds stresses are close to zero. This is different from the high swirling stabilization mechanism where high shear stresses in the recirculation zone may produce quenching.

Hsieh et al. [43] state the difficulties in burner scaling. In their work they present an analytical approach contemplating NO_x emissions and discuss the results for a reduced model. Cheng et al. [18] tackle the problem of scaling for low emission furnaces and boilers. Two types of burner are investigated: the jet swirl burner and a new vane swirl burner. The vane type LSB includes a central bypass that leaves part of the reactant unswirled, and it includes a screen-type turbulence plate generator. This plate serves to balance the pressure drops across the bypass and the swirl vanes, and helps to maintain a uniform radial flow distribution. It should be noted that their burner has a single chamber that only split the flow into swirling flow and core flow at the entry of the LSB.

In general, for a classical premixed burner, a scaling formula for thermal input uses a reference velocity U_∞, the mass flow rates of air and fuel, and the cross sectional area of the burner A.

$$U_\infty = \frac{\left(\dot{m}_{air}/\rho_{air} + \dot{m}_{fuel}/\rho_{fuel}\right)}{A} \qquad 2\text{-}10$$

Once an operating range (blowoff - flashback) is determined for U_∞, a constant velocity scaling criterion applies. With a thermal input as a datum, the flow rates are calculated; and with a constant velocity, the area of the burner is established.

In their study [18], the authors verify the constant velocity scaling criterion for the burner diameter, in order to accept higher thermal inputs. However the swirl number needed for stable operation should be scaled separately using a constant residence time criterion. For the same value of equivalence ratio, Φ, they find a swirl number almost constant for stabilization that is independent of U_∞. NO_x emissions are independent of thermal input, rather they are only a function of Φ.

Plessing et al. [28] use an LSB to study the turbulent burning velocity, S_T. They confirm that the flame, which stabilizes itself close to the burner exit, is not affected by recirculating flow, and that the mean strain rates are much lower when compared with similar flow patterns of stagnation point flames. Shepherd et al [44] prove that the main effect in increasing turbulence is the augmentation of the burning rate.

Littlejohn et al. [12] describe their tests on an LSB for industrial boilers combined with flue gas recirculation (FGR). The flame speed at the leading edge of the flame brush scales linearly with the turbulent fluctuating velocity u'. For operability, a minimum value of $S = 0.4$ is detected.

Johnson et al. [3] perform a detailed comparison of the flowfields and emissions of high and low swirl injectors (HSI with $S = 0.73$, LSI with S = 0.5) for lean premixed gas turbines using an LSB and a PIV system. A 60% reduction in the NO_x emission in the LSI is noticed and attributed to the lack of recirculating flow in the flowfield, which leads

to shorter residence time. Only the non-reacting flow shows a weak recirculation zone in the far field that disappears in the presence of combustion.

Recently, Littlejohn and Cheng [45] show tests on a gas turbine LSI, based on the LSB concept for different fuels. They prove its capability of supporting various hydrocarbons. The comparison of the velocity field between reacting and non-reacting flow indicates that the overall effect of the flame is equivalent to an aerodynamic blockage towards the flow supplied by the LSI. They also verify a linear correlation between the turbulent flame speed S_T and turbulence intensity. At the exit of the LSI, in the nearfield, they observe a linear velocity decay along the centerline. Finally, the radial representation of the velocity profile of the LSI shows a relative flat central region.

Chapter 3: Experimental study

3.1 The Low-Swirl Burner (LSB)

3.1.1 Introduction

The basic LSB consists of a turbulent, 1D inner core flow surrounded by a swirling annular flow. For the current research, a fully controlled laboratory LSB has been constructed to control the inner core flow and outer annular flow independently. Figures 3-1, 3-2, and 3-3 illustrate the apparatus.

Premixed methane and air enter separate concentric settling chambers at the base of the burner that contains small diameter lead shots, which act to break up the incoming jets, and as a flame arrestor in the event of flashback. The flow then passes through two sets of concentric settling screens to eliminate turbulence and promote a uniform velocity profile before the flow enters two concentric cubic-contoured nozzles. A perforated plate inserted at the exit of the inner nozzle only, creates a desired amount of grid turbulence upstream of the swirler. Two different inner nozzles can alter the inner flow and outer flow diameter ratio of the burner.

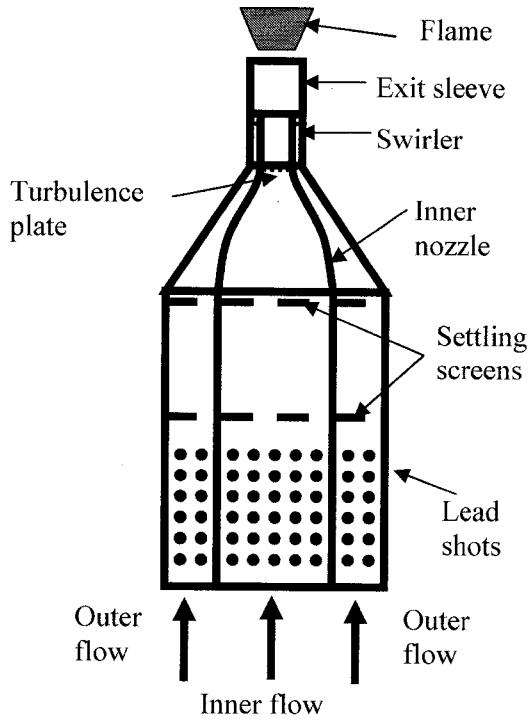

Figure 3-1 Burner components

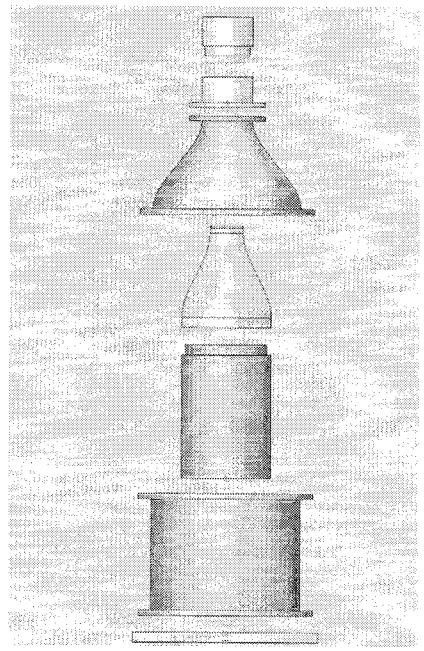

Figure 3-2 Burner exploded view

Figure 3-3 Burner with mass flow controllers setup

3.1.2 LSB components

The screens in the settling chamber

In order to study the LSB flowfield, it is best to have the flow arriving at the swirler with a high degree of uniformity and without the presence of irregular fluctuations. Screens are suitable for this purpose; they are equivalent to those installed in the settling chamber of a wind tunnel, which have a smoothing effect on the velocity profile [46].

Screens also reduce turbulence by destroying the upcoming eddies with size larger than the screen mesh size. The large eddies are broken down into smaller ones, which are more easily dissipated, due to the effect of viscous forces produced by local friction. Actually, screens eliminate disturbances and create new ones, but of less energy. The screen generated turbulence kinetic energy decay, k, follows this empirical law [47]:

$$\frac{k}{U^2} \cong A'\left(\frac{x-x_o}{M}\right)^{-n} \quad for \quad \frac{x}{M} > 10 \tag{3-1}$$

where U is the mean axial velocity, x is the distance from the screen, x_o is an empirical effective origin, M is the spacing of the wires, A' is a coefficient function of the geometry of the screen mesh close to $3M$, and the exponent n is in the range of 1.4 to 1.2. However, nearly all data are consistent with n = 1.3 [48]. As other flow management devices, screens are defined by the solidity, σ,

$$\sigma = \frac{\text{projected blocked area}}{\text{projected total area}} = 1 - \left(\frac{a}{M}\right)^2 \tag{3-2}$$

or sometimes by the porosity, β, which is

$$\beta = 1 - \sigma = \left(\frac{a}{M}\right)^2 \tag{3-3}$$

The next figure describes a screen mesh, where a is the opening, d is the diameter of the wire (for cylindrical obstructions) and M is the spacing of the wires, also referred as the pitch (number of wires per inch or mm).

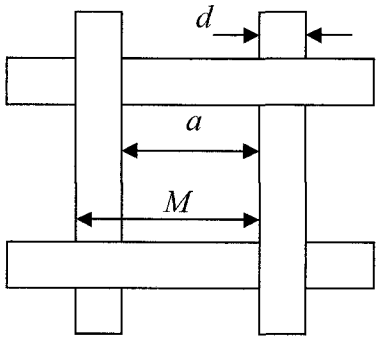

Figure 3-4 Mesh of a screen

A critical parameter that defines the screen behaviour is the pressure loss coefficient, K,

$$K = \frac{\Delta P}{\frac{1}{2}\rho U^2} \qquad 3\text{-}4$$

where ΔP is the pressure loss across the screen, ρ is the density of the fluid, and U is the fluid velocity. K is a function of the Reynolds number and the geometry (the solidity) of the screen. Different equations exist to determine K. One of the most representative is [46, 49]

$$K = \left(0.52 + \frac{17}{Re}\right)\frac{\sigma(2-\sigma)}{(1-\sigma)^2} \qquad 3\text{-}5$$

As mentioned by Metha and Bradshaw [50], a screen with a $K = 2$ removes practically all the variation in the longitudinal mean velocity. The design principles and the selection of screens for this research are described in Appendix **A**.

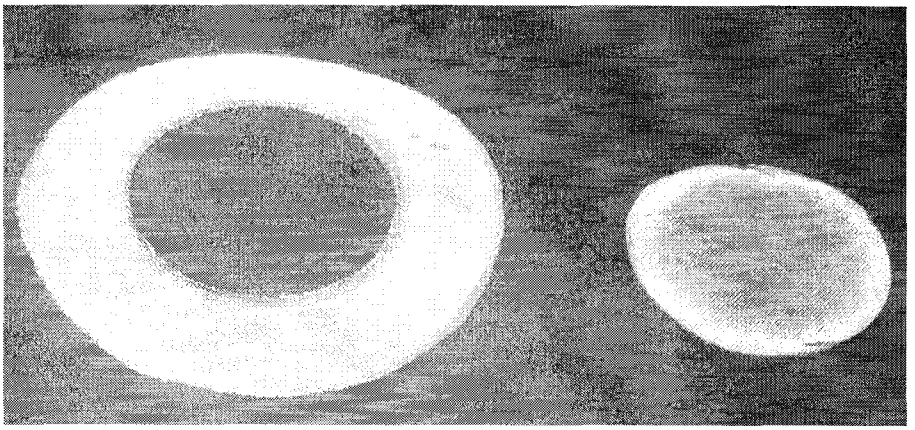

Figure 3-5 Outer and inner screens

The turbulence generator plate

A perforated plate, which acts as a turbulence grid generator, located at the exit of the inner nozzle and at the bottom of the swirler, creates homogeneous and isotropic turbulence. This kind of turbulence is easier to use, since it eliminates possible variables, and it is studied the most [46]. In this case, the properties are independent of position and direction.

This type of turbulence normally comes from passing a stream through a perpendicular array of equally spaced obstruction, such as rods, honeycomb grids, or from plates with equidistant perforations. The work exerted by the blockage rods of the screen on the upcoming flow, creates turbulence, with the subsequent production of swirls downstream. It is demonstrated that turbulence generated by these methods, is fairly homogeneous on the plane perpendicular to the main stream and isotropic after a distance of ten times the spacing, M, of the grid [51]. The two fundamental macroscopic parameters of isotropic turbulence are the turbulence intensity and the turbulent integral length scale [46]. This length scale is nominally the length beyond which various fluid

mechanical quantities become essentially uncorrelated [20]. It characterizes the large eddies; those eddies of low frequencies and long wavelengths.

It is known that turbulence generated by these methods produces a component of u' that is actually 20% higher than v' and w'. This has been solved by Comte-Bellot [52]; when they introduced a contraction after a distance of 18 M that render all components equal. For the revolution-type geometry of our burner it is verified that perforated plates with circular holes centered in a hexagonal layout work very well [53].

In his work, Roach [54] finds that for perforated plates, the turbulence generated is not particularly influenced by the Reynolds number. Liu et al [55] confirms this conclusion. The main parameter that affects the performance of the plate is the solidity σ. Formally, a range of σ between 30 and 38% is considered acceptable [46]; nevertheless higher values, below 50%, have been used successfully. Solidity can not be increased indefinitely to generate the required turbulence. Elevated values of solidity can create instabilities in the flow and the turbulence generated becomes anisotropic and non-homogeneous.

Liu et al. [55] also observe an increase in turbulence level with an increase in solidity. A plate with 35% solidity shows a good degree of homogeneity regarding the uniformity of the turbulence intensity along the cross-section. The solidity of circular perforated plates is

$$\sigma = 1 - \frac{\pi}{4}\left(\frac{d}{M}\right)^2 \qquad 3\text{-}6$$

where d is the diameter of the holes and M is the spacing amongst them. In our case, the plates had circular holes of 3.5 mm in diameter, arranged in a symmetrical pattern about

the center, as Figure 3-6 displays. In this study, the plates tested have solidities of 40, 48 and 56%.

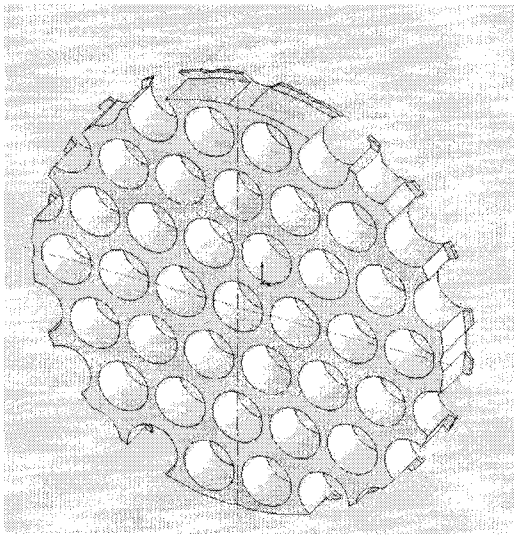

Figure 3-6 Turbulence plate generator

The nozzles

Two nozzles are at the top of the burner. The inner nozzle conducts the flow towards the turbulence plate mounted at the bottom of the swirler. Between both nozzles, the flow accelerates towards the vanes of the swirler. Flow contractions have two major effects: an increase in the uniformity in the flow direction, and a reduction of the streamwise turbulence intensity level (defined as the standard deviation of the streamwise fluctuations divided by the local mean velocity) [46]. Appendix **B** shows the procedure followed to determine the nozzle contours.

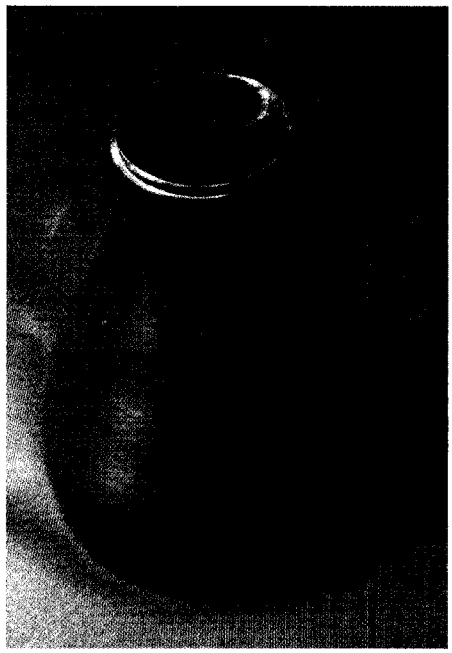

Figure 3-7 Inner nozzle

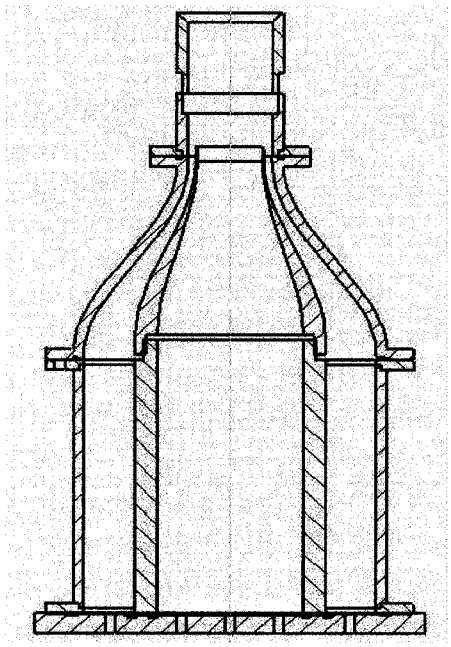

Figure 3-8 Nozzles assembly

The swirlers

The swirler consists of 8 curved vanes surrounding the inner core of the burner that imposes an annular swirling flow around a non-swirling central core flow. The swirl vanes are aligned with the burner axis at the inlet and they have and exit angle of 37°. Figures 3-9 and 3-10, show two different swirlers with inner diameters of 80% (R-8) and 60% (R-6) of the 50 mm external diameter.

Figure 3-9 Swirler R-8 (left) and R-6 (right)

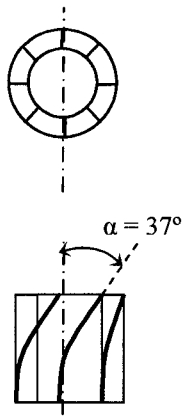

Figure 3-10 Vanes exit angle

The exit sleeves

The exit sleeves of the burner, shown in Figure 3-11 are of 50 mm and 80 mm in length.

Figure 3-11 Sleeves at the exit of the burner

The seeders and its components

For PIV measurements, small (~1-5 μm) droplets of olive oil are seeded into both the inner and outer reactant air flow. For this, a set of canisters with four Laskin Nozzles each are inserted on the air line. The tips of the nozzles are submerged in the olive oil and air is forced out through the orifices producing microscopic bubbles. As the bubbles rise to the surface and burst, micrometer-sized aerosol droplets are produced. This method reduces the chances of having large particles since they can not be sustained by the bubbles [56]. A set of secondary canisters (called dampers) ensure that any larger droplets are removed through impaction onto an inverted angle plate.

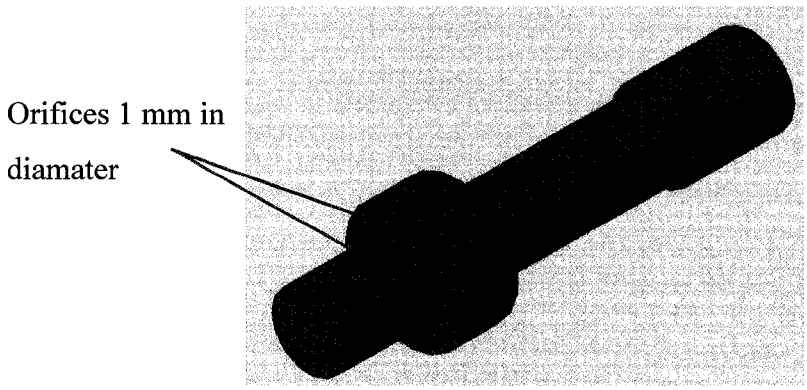

Figure 3-12 Laskin nozzle

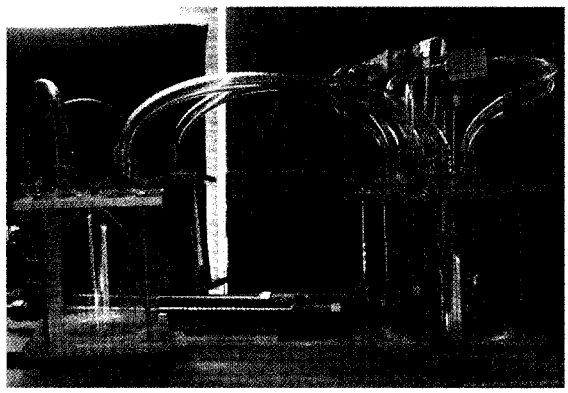

Figure 3-13 Seeders and dampers

3.2 Data acquisition and control

As illustrated in Figure 3-14, a system of six mass flow controllers (MFC) regulate the following parameters:

- Inner and outer mixture flowrates, velocities, and power.
- Equivalence ratio, Φ, of the air-methane mixture.
- Geometric swirl number, S_g.
- Percentage of seeding flow to be used during PIV.

The calibration and operation procedures of the MFC are in appendix **C.**

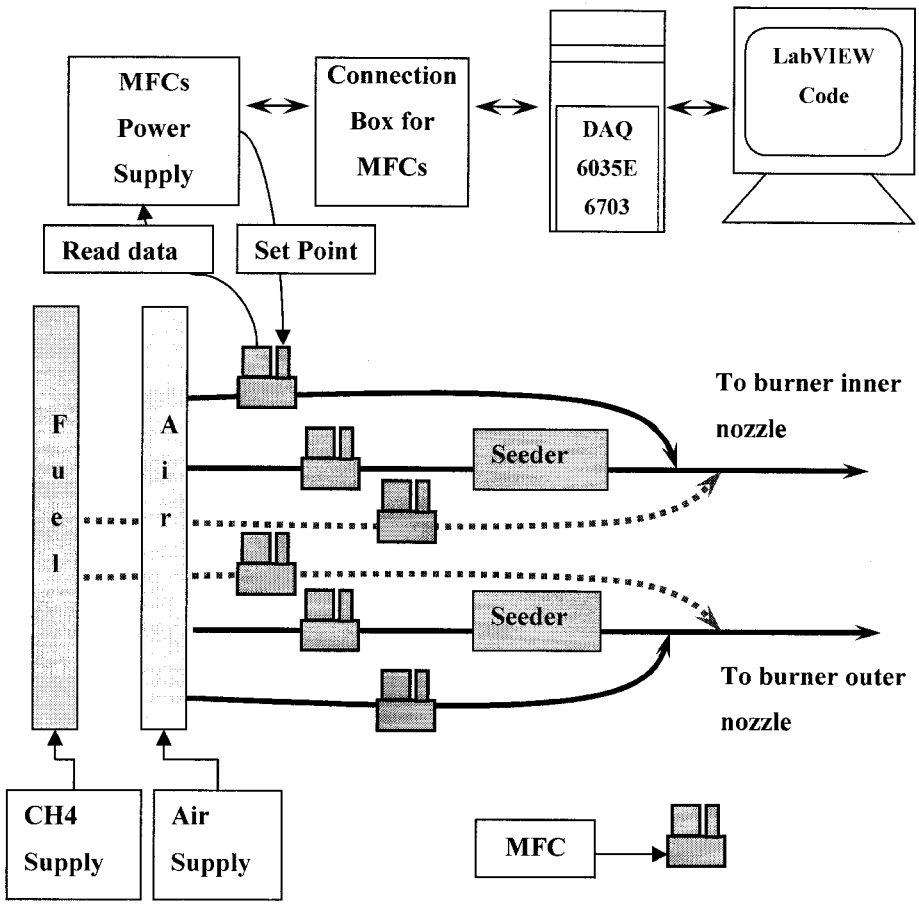

Figure 3-14 Mass flow controllers and seeders setup

Data Acquisition (DAQ)

The DAQ includes a Pentium processor computer with National Instrument data acquisition boards 6703 and 6035E. Specially shielded cables guarantee the data transmission. A code in LabVIEW written by Johnson [38] is used. Each MFC is represented by a virtual instrument (VI) in the LabVIEW code, which includes the calibration equations. The MFCs are calibrated for various gases, to attain higher precision than using the gas conversion factor (GCF) tables. Figure 3-15 illustrates the front panel to control the MFCs system.

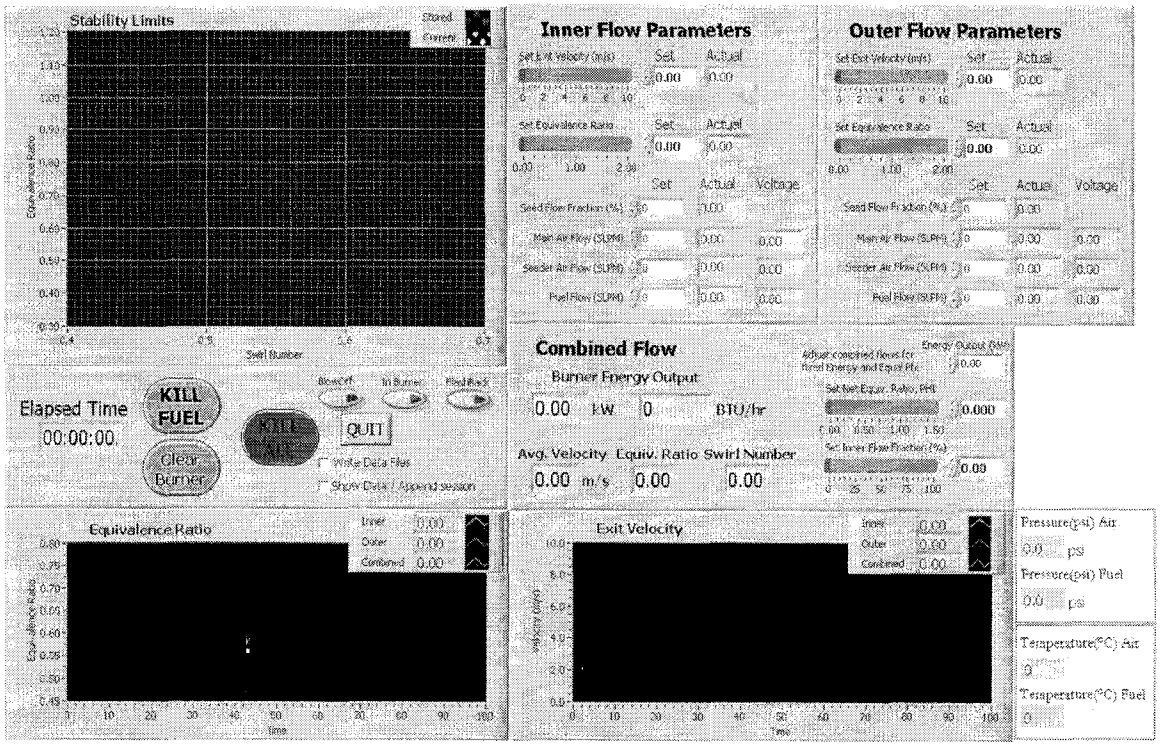

Figure 3-15 LabVIEW front Panel

3.3 Stability maps - Methodology

3.3.1 Test procedure

1. A schedule of test combinations is defined including geometrical variables: types of swirlers, turbulence plate generators, and exit sleeves.
2. Constant physical parameters are selected: thermal input power (P_{th}), total volumetric flowrate (Q), and velocity of the inner core flow (U_i).
3. The data acquisition and control device (DAQ) are calibrated.
4. Constant parameters (e.g., Power of 40 kW) are set on the code.
5. The air-methane mixture valve is opened and the flame is lit.
6. The swirl number, S_g,, and the equivalence ratio, Φ, are varied.
7. The points of flashback and blowoff are recorded.

8. In some cases where the flame does not flash back, a previous condition is recorded instead, which is called "in burner".

3.3.2 Data point identification

Figures 3-16 to 3-20 show each condition of the flame and a typical stability map registered on the code front panel. Since the determination of each point is performed through the observation of the flame, repeatability test for each condition (flashback, in burner and blowoff) are performed in order to establish the random component of the uncertainty of measurement. Results are in Appendix **E**

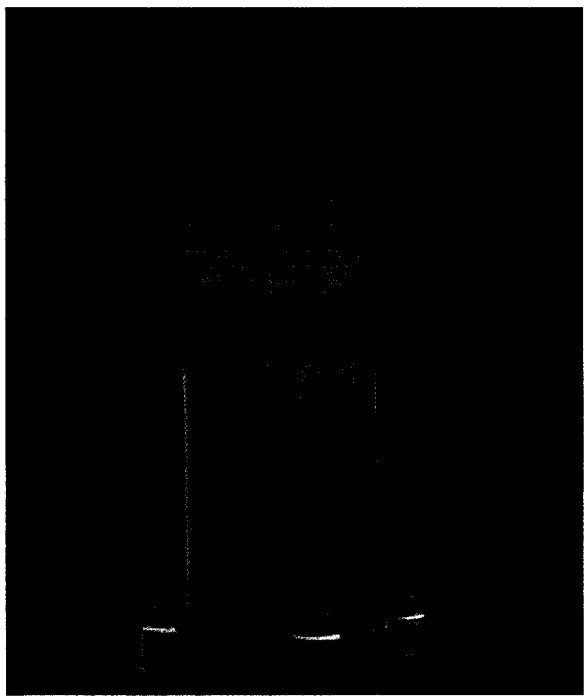

Figure 3-16 Stable flame

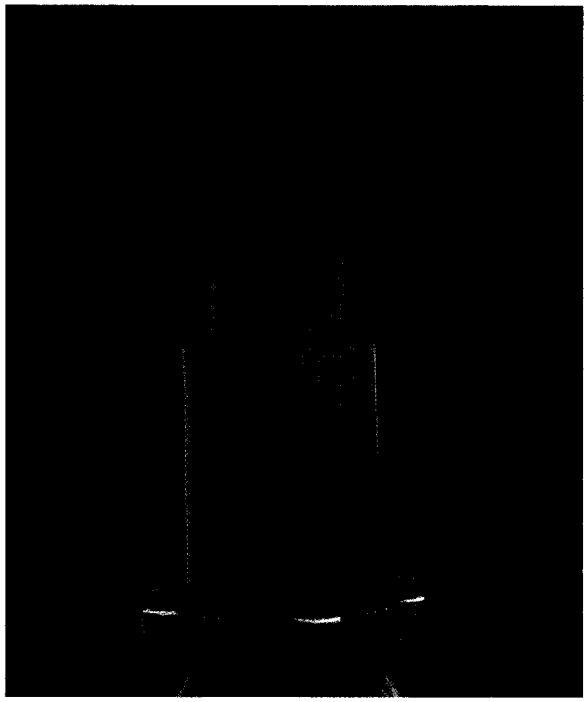

Figure 3-17 Flashback

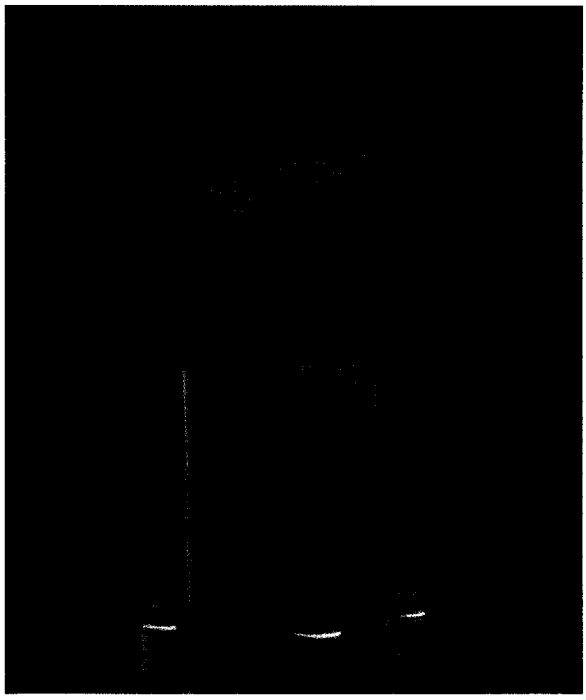

Figure 3-18 Blowoff

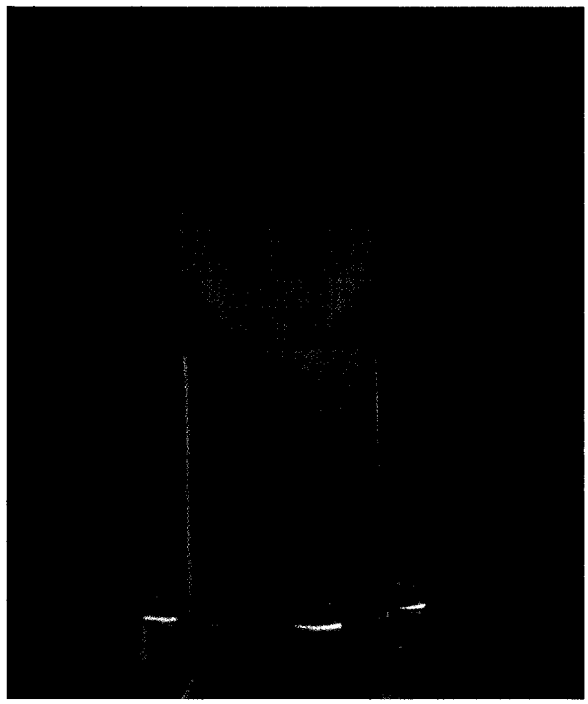

Figure 3-19 In burner

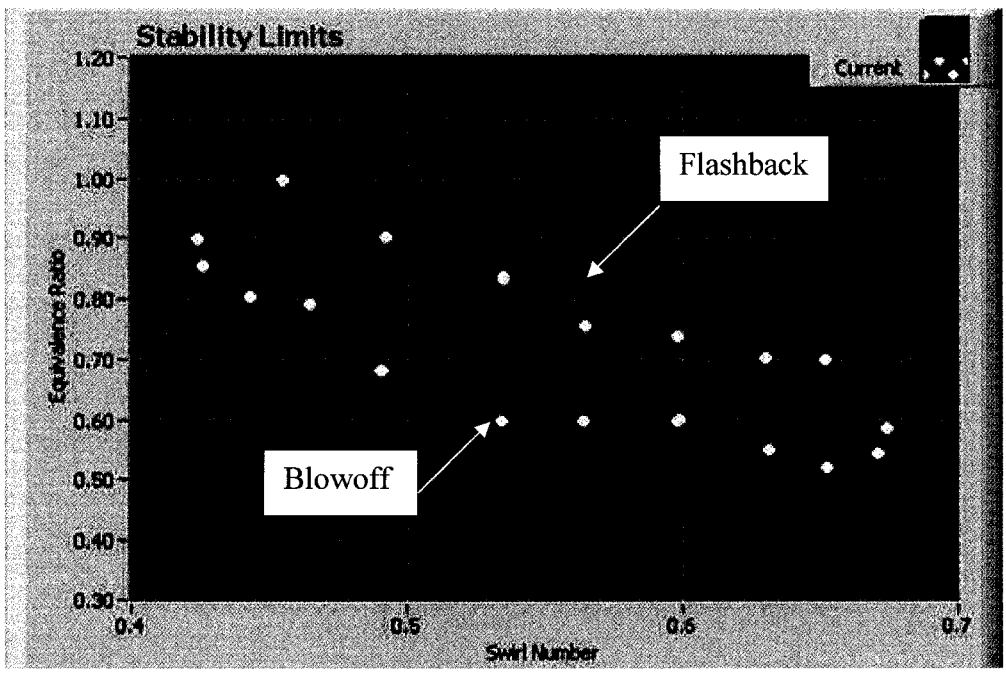

Figure 3-20 Stability map

Table 3-1 describes the measurement routine. The experiments are performed so that one variable changes at a time. After each set of data is recorded, it is analyzed, and the most influential variable is varied in the next set of measurements.

Table 3-1 Testing schedule for determination of stability maps

	Power [kW]	Exit sleeve length [mm]		Turbulence generator solidity, σ [%]		
		50	80	40	48	56
Thermal input power (P_{th})	10		X		X	
	20		X		X	
	40		X		X	
	80		X		X	
	10	X			X	
	40	X			X	
	20	X				X
	40	X				X
	20	X		X		

Velocity of the inner core flow (U_i)	Velocity [m/s]	Exit sleeve length [mm]		Turbulence generator solidity , σ [%]		
		50	80	40	48	56
	2	X		X		
	4	X		X		
	6	X		X		

Total flowrate (Q)	Flowrate [slpm]	Exit sleeve length [mm]		Turbulence generator solidity, σ [%]		
		50	80	40	48	56
	400	X		X		
	800	X		X		
	1600	X		X		

3.4 Particle image velocity (PIV) system

3.4.1 Introduction

PIV allows instantaneous vector velocity measurement throughout a plane of the flowfield. This non-intrusive technique measures two velocity components in the illuminated cross section of the flow. The technique is based on the measurements of the displacements of particles seeding the flow, between two consecutive light pulses. The third velocity component can be determined by a stereoscopic PIV setup. PIV requires one camera for 2D and two for stereoscopic 3D. In 3D, the reconstruction of a 2D-3C (components) vector field is computed once the 2D-2C vectors have been determined for each camera. Figure 3-21 describes the setup.

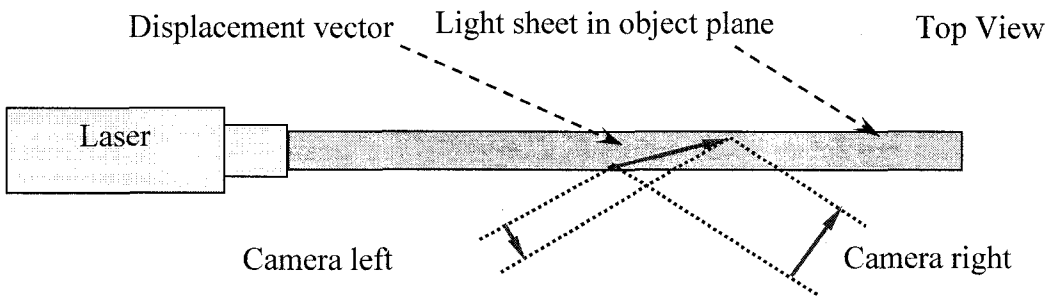

Figure 3-21 3D stereoscopic setup

The geometry required to reconstruct the 3D displacement field from two projected, 2D displacement fields, is in [57]. The current development status of PIV is in [58].

The cameras register the images given by each light pulse on the illuminated flowfield plane. Once the exposures are recorded, they are divided into so-called interrogation windows (IW). By means of statistical tools (correlation techniques) one local displacement vector is calculated for each IW on the CCD (charge-coupled device)

of the camera. The correlation produces a signal peak that identifies the average displacement. The arrangement is depicted in Figure 3-22, from [59].

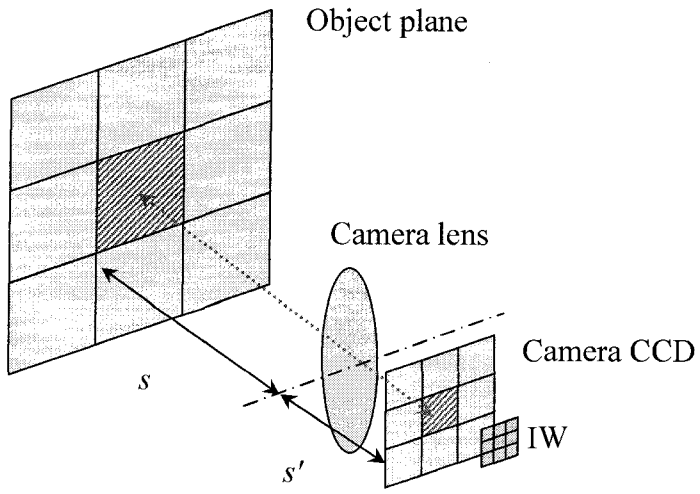

Figure 3-22 Real and transmitted image to the CCD of the camera

Since the operator defines the time step of the system, the local velocity vector is

$$\overline{V} = \frac{\overline{\Delta X}}{dt} \qquad 3\text{-}7$$

The statistical techniques for the equipment include auto-correlation (single frame/ double exposure) and cross-correlation (double frame / double exposure). For the first technique, there are particles images from both exposures in the same frame. Hence, the sign of the displacement can not be detected because it is not possible to tell what particles are illuminated first. For a reversed flowfield this ambiguity can be problematic. Thus, in these experiments, the cross correlation technique was selected.

3.4.2 PIV system components

The Laser

A La Vision system with softwares DaVis and FlowMaster [10] was used for our experiments. The system hardware includes an Nd:YAG New Wave Solo PIV laser, with a maximum energy per pulse of 120 mJ. This laser has two rods, so each emits a pulse for the double exposure effect. Both pulses combine through a set of mirrors so they leave the laser lens on the same plane and direction. A Q-switch allows for the stored energy to be released in a very short pulse of few nanoseconds, so it is considered an instantaneous pulse of light. The fundamental wavelength, of 1064 nm, generated inside the laser, is processed internally to provide a green visible light of 532 nm. The programmable timing unit (PTU) controls the firing of the laser which allows setting the critical separation time *dt* (in microseconds) between two laser flashes. This time depends on the camera, laser, and correlation techniques used. For a certain velocity field, and a magnification factor s'/s, the delay, *dt*, defines the separation of the particles images on the CCD. The loss of particles that travel out of the interrogation window during the time delay *dt,* limits the selection of *dt*.

In general, for cross-correlation, the separation of particle images, $\overline{\Delta X}$, defined in pixels should be higher than the resolution of the system and smaller than 25% of the IW size [60, 61]. It is approximately

$$0.1\ pixel < \overline{\Delta X} < \frac{1}{4} D_{IW} \qquad 3\text{-}8$$

The deviation of the particle separation within one IW should be smaller than the particle diameter, d_p. All of the previous conditions influence the selection of the IW size, D_{IW}, and the delay, dt, according to the flow velocity.

The cameras

Two CCD cameras are used for the 3D PIV. They are of the progressive scan interline transfer CCD type. The cameras can work in a double-shuttered mode, called "frame straddling". Each pixel is partially masked during the first exposure. The charge of the exposed part of the chip is immediately shifted to the masked part, which acts as a storage. While the first exposure is read out, the second exposure is recorded. After the complete read out of the first exposure, the second image is shifted to the storage region from where is also read out [10]. The exposure time of each frame is quite different. For the first frame it is around few microseconds, since the charge is rapidly transferred to the storage masked area. For the second frame is in the order of hundred milliseconds, since the charge can not be transferred to the storage masked pixel area until the charge from the first exposure is read out to the computer. The time-length of the laser flash is around 5 nanoseconds. In combustion the possibility exists that for the second exposure, a mechanical shutter is required to avoid the light that the flame itself emits. Table 3-2 describes the essential features of the cameras used for these measurements.

Table 3-2 Cameras specifications

Imager Intense	Imager Pro 2M
Number of pixels 1376 (h) x 1040 (v)	Number of pixels 1600 (h) x 1200 (v)
Pixel size : square, 6.45 μm	Pixel size : square, 7.4 μm
A/D converter: 12 Bit	A/D converter 12 Bit

Figure 3-23 shows a timing scheme described by the manufacturer La Vision [60], of a PIV recording:

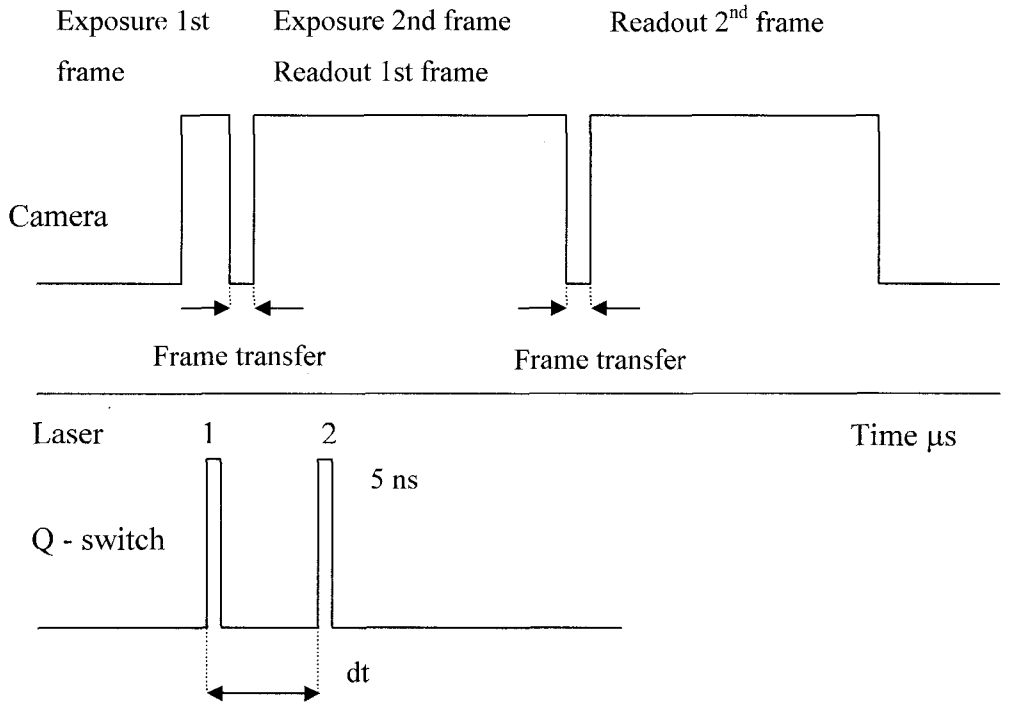

Figure 3-23 Timing for double frame / double exposure

Band pass filter

The band pass filter eliminates background light, since the only light required is that scattered by the tracer particles. Band pass filters of 532.5 nm are installed on each

camera. Two types are normally available: a bandwidth of either 10 or 3 nm. For combustion experiments, the last is preferred to avoid light projection from the flame.

Light sheet optics

The light projected as a cylindrical small beam by the laser has to be transformed into a plane sheet of certain height and thickness. This is accomplished by a plano-concave (normal) lens (f = 38 mm, height = 26 mm) that diverges the beam and then a symmetric-convex lens (f =1000 mm, diameter = 100 mm).

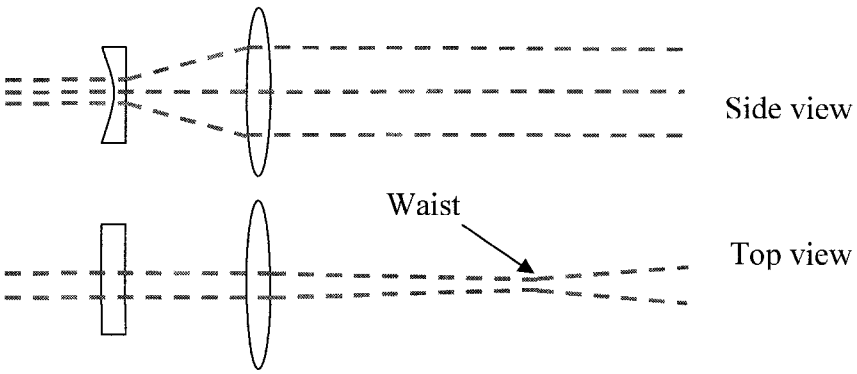

Figure 3-24 Light sheet optics

The software

The LaVision system includes the General Image Software DaVis 7.1, and PIV software DaVis FlowMaster. This software uses the standard cyclic Fast Fourier Transform algorithm that calculates a cyclic correlation of the interrogation window IW, and is similar but not exactly the same as the mathematical true correlation:

$$C(dx,dy) = \sum_{x=0,y=0}^{x<n,y<n} I_1(x,y)I_2(x+dx,y+dy), \quad -\frac{n}{2} < dx,dy < \frac{n}{2} \qquad 3\text{-}9$$

where I_1 and I_2 are the image intensities of the first and second IW. The resultant 2D array, C, provides the correlation strength for the integer displacements (dx,dy) between

the two IWs, where n is the size of the IW. Actually, except for a very small IW, the algorithm computes the 2D Fast Fourier Transform (FFT) from the two IWs. Then they are multiplied by the complex conjugated and the inverse FFT is obtained, which produces the cycle correlation function. This is much faster (up to 50 times) than using the above equation [60]. Mathematically denoting cross-correlation with "*" and the complex conjugate with a minus sign, for a 2D array of data:

$$(f * g) = FFT^{-1}\left[\, FFT(f) \cdot FFT(-g) \,\right] \qquad 3\text{-}10$$

Resolution

In general, the resolution of an image refers to the extent of details that the image can show. One image has more resolution than another if it possible to observe more lines, or pixels, in the first image than in the second. In this system, the image buffer may contain light intensity values from 0 up to 65535 counts, which have to be displayed with a palette of 256 colours on the screen. Hence, the software maps the 65536 intensity values to the 256 colours. For example, if a resolution of 512 counts of intensity is chosen, this means that for every 2 counts of light intensity (512/256 = 2 counts/colour), there will be a different colour on the screen. If the resolution is set to 8K (8192) counts of intensity, a new colour will show for every 32 counts, that is 8192/256 = 32 counts/colour. Continuing, if the image light intensity has maximum spots of light intensity in the vicinity of 2100 counts on the camera CCD, a resolution of 2K is considered appropriate. For this example, if a resolution of 512 is selected, there will be saturation in all points above the value of 512, without any extra information. On the

contrary, if the user chooses a resolution of 8K, the image is poor, with minor changes in colour representing large changes of light intensity on the original image.

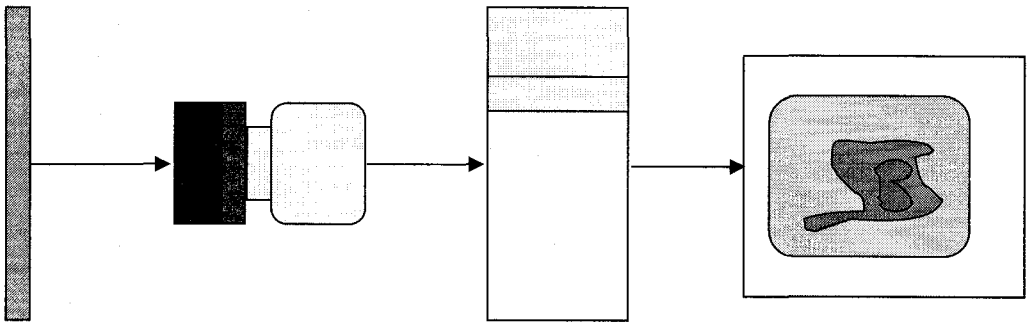

Figure 3-25 Resolution and representation on the screen

3.5 Test implementation and data processing

As described, a forward–backward scattering 3D (stereoscopic PIV) is employed for the determination of the reactant velocity field as shown in Figure 3-26. The double-pulsed Nd:YAG laser supplies 120 mJ per pulse at a wavelength of 532 nm and two frame-straddling 12-bit, CCD cameras fitted with 532 nm band pass filters record pairs of particle images for correlation. Small (~1-5 μm) droplets of olive oil are seeded into both the inner and outer reactant air flow with a Laskin nozzle arrangement. The fine droplets are rapidly consumed at the flame front and also serve as a marker of instantaneous flame position. Attention is given to optimizing light sheet thickness, seed particle density, image resolution, and laser timing to ensure 3D vectors could be obtained with a minimum uncertainty [57, 61]. To obtain appropriate spatial resolution of particle images (to avoid peak-locking effects), the field of view (FOV) is optimized over one-half of the

radially symmetric flowfield (from the burner centerline radially outward to a distance of 85mm). The off-axis angle, θ, of each camera is set to 28°, in order to balance out-of-plane vector errors with uniformity in magnification [62], and Scheimpflug mounts are on the camera lenses. Data analysis reveals that for each given flame condition, a minimum of 600 up to a maximum of 1000 image pairs are required to produce statistically significant mean flowfield data.

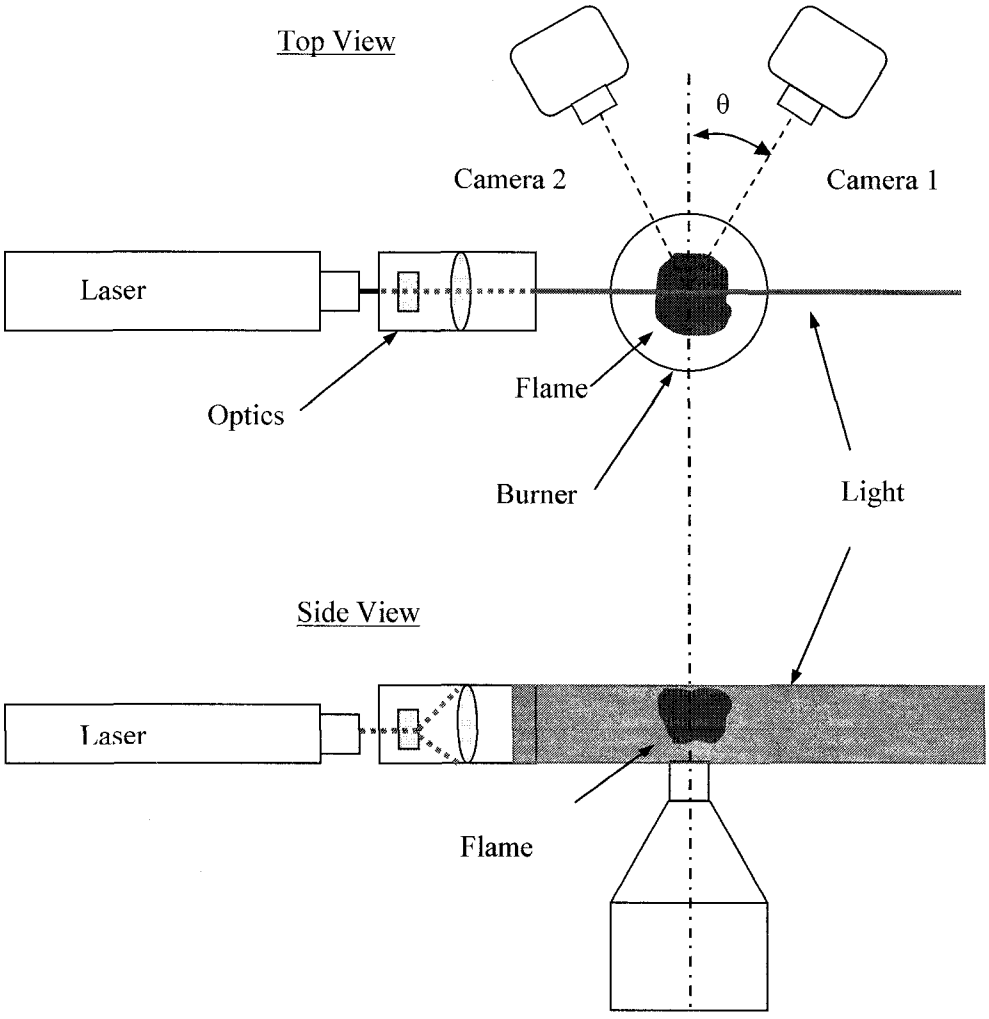

Figure 3-26 PIV setup

Figure 3-27 depict a typical flowfield, where vectors show the in-plane velocity components U and V, and the coloured contour plot represents the swirling velocity W.

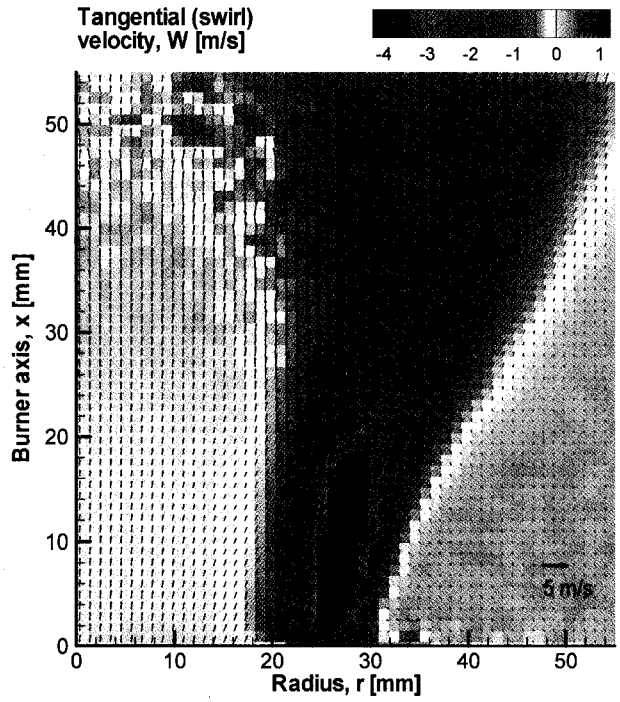

Figure 3-27 Flowfield velocities

Digital image processing is performed on the raw PIV particle images, from the spatially mapped field of view. This allows the definition of the position of the instantaneous flame front. In this process, images are first smoothed with a 9x9 pixel linear filter and subsequently binarized with a fixed threshold intensity value to separate reactants and background image noise. Experimentation shows that the results are not at all sensitive to the chosen threshold value within a wide range of values.

For each flame condition, the full set of instantaneous binarized images is then averaged, and the 0.5 intensity contour extracted. Finally the use of binarization and Laplace edge detection permits the computation of the position of the mean flame front

contour, as shown in Figure 3-28. Figure 3-29 shows the result of the mean flame front contour, superimposed on the 3D velocity field. The complete PIV implementation and data processing are in Appendix **D**

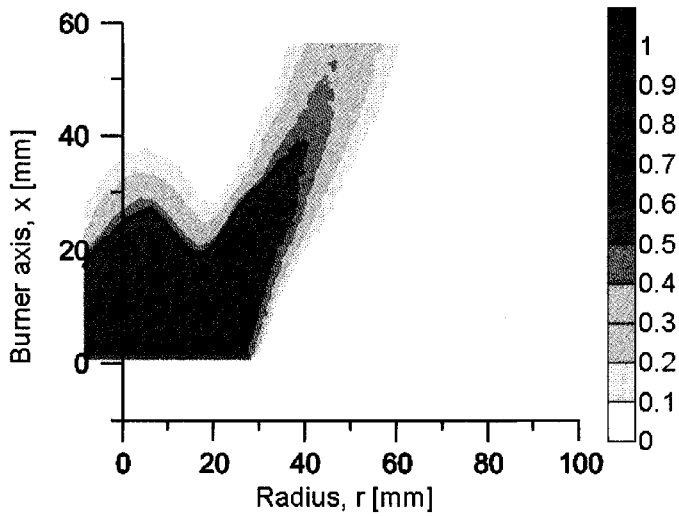

Figure 3-28 Mean flame front contour; intensities on the background

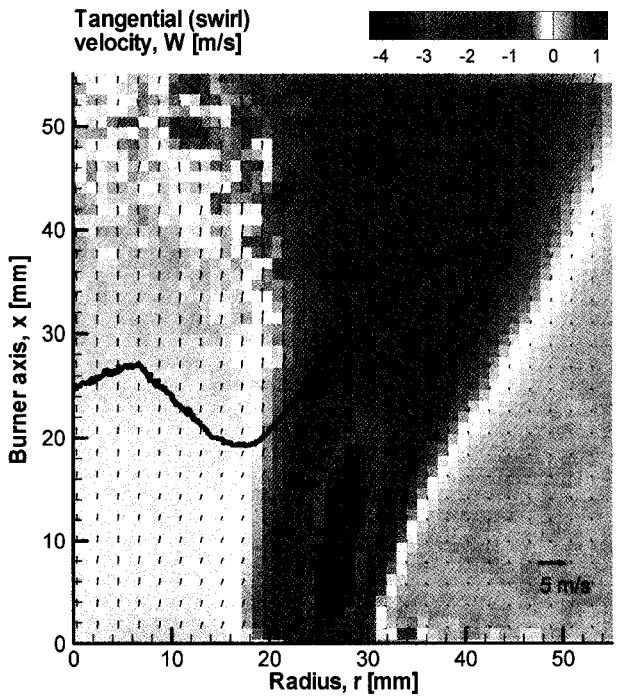

Figure 3-29 Mean flame front contour superimposed on the 3D velocity field

Actual flow swirl number, *S*, vs. geometric swirl number S_g

In Figures 3-30 and 3-31, the actual flow swirl number, *S*, is calculated at different locations by integrating numerically the mean three-component velocity field. The flow swirl number decreases away from the exit of the burner. The value at the burner exit is greater than the computed geometric swirl number, S_g, based on flow inputs. This can be attributed to the fact that the exit angle of the flow when it leaves the swirler is not necessarily the same as the exit angle of the vanes of the swirler. Nevertheless, the difference between *S* and S_g is consistent for all of the measured flowfields as shown in Figure 3-31. Thus the geometric swirl number, S_g, is a useful surrogate for the actual flow integrated swirl number, *S*.

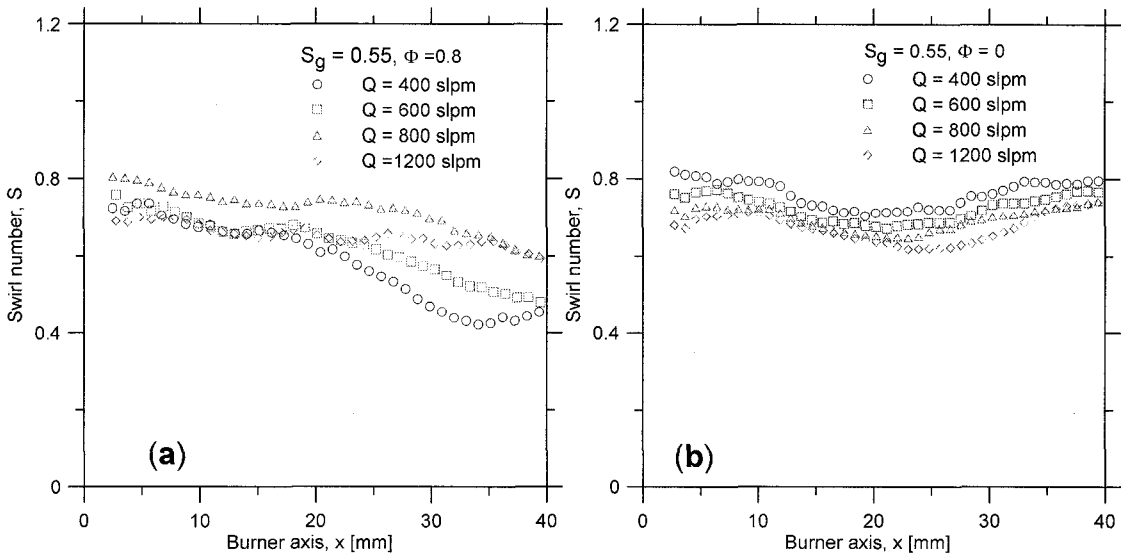

Figure 3-30 Flow-integrated swirl number, S, at different locations in (a) reacting and (b) non-reacting flow

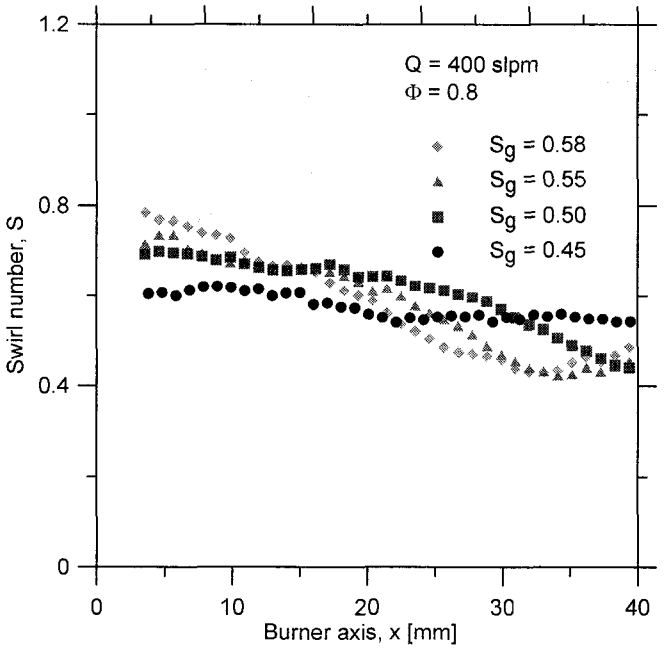

Figure 3-31 Flow integrated swirl number, S, for different geometric swirl numbers, S_g, in reacting flow

Chapter 4: Results

4.1 Stability maps

Stability maps of blowoff and flashback limits were obtained for the two different LSB geometries, R6 and R8, for a range of fixed thermal input power, P_{th}, total flowrate, Q, and velocity of the inner core flow, U_i. Tests were conducted to include variation of the geometric swirl number, S_g, and the equivalence ratio, Φ. For the fixed thermal input tests, the amount of fuel was constant and the amount of air varied, to accommodate for the change in Φ. For the fixed total flow and fixed inner velocity experiments, different Φ values were achieved through changes in both, air, and fuel flows. For each of the three operational parameters, P_{th}, Q, and U_i, different regimes were selected. For instance, a test included fixed values of P_{th} (10, 20, 40, and 80 kW), while Q and U_i varied.

The objective of these experiments was to study the stabilization mechanism while isolating effects due to combustion (and its underlying chemical nature) and fluid mechanics. Fixed thermal input closely equated to a constant energy release. For a fixed total flowrate, the effects of varied swirl were, in part, isolated from other flow effects. Lastly, for tests with a constant inner velocity, the core flow turbulence intensity was maintained, which in turn is a component of the turbulent flame speed, S_T.

As mentioned in Chapter 2, the swirl number S was considered a governing parameter for swirling flow. However, it was not clear if stability limits could be predicted by the use of S, or whether it could serve as a universal scaling parameter.

Figures 4-1, 4-2 and 4-3 show plots for the same burner geometry (identical swirler, exit sleeve and turbulence generator), where stability limits were represented by the equivalence ratio, Φ, and the geometric swirl number, S_g. While the occurrence of blowoff was distinctly identifiable, flashback was somewhat subjective to define and was often anticipated by the flame positioning itself below the exit plane of the burner; this condition was denoted as "in burner" on the plots.

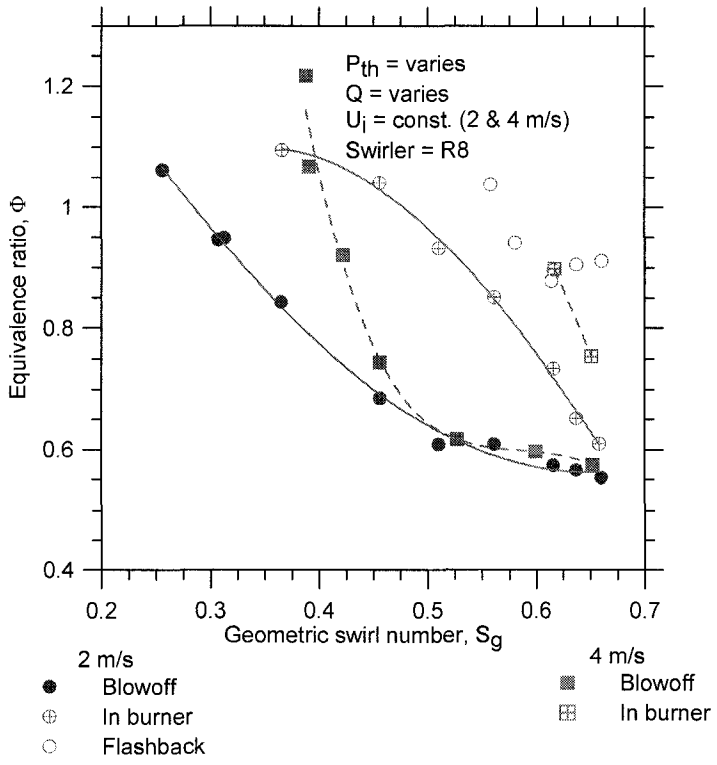

Figure 4-1 Flame stability regime: constant inner flow velocity

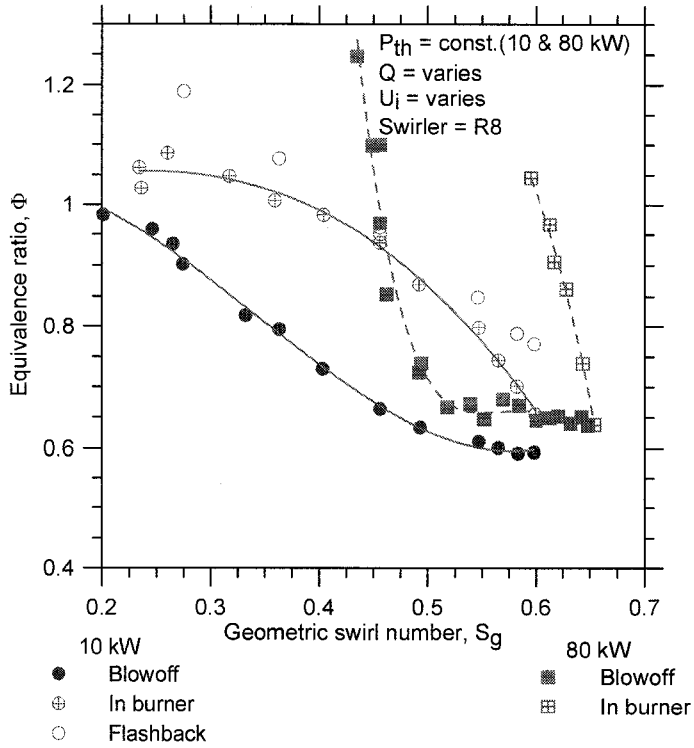

Figure 4-2 Flame stability regime: constant thermal input power

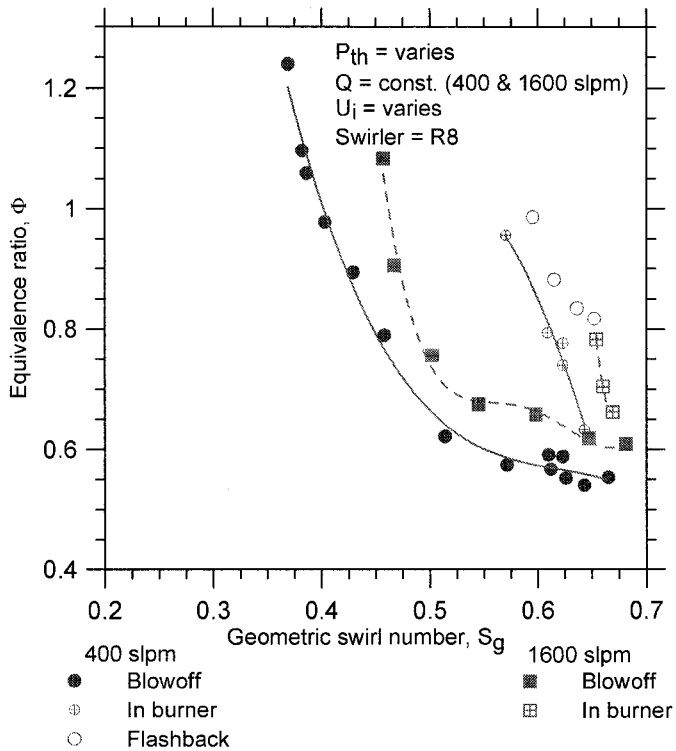

Figure 4-3 Flame stability regime: constant total flowrate

It is clear from these plots that the geometric swirl number alone is not sufficient to correlate the data, and the stability region shift, as inner flow velocity, thermal input power, or total flowrate changes. Thus, these results invalidated the hypothesis presented by Cheng [41], where the small change in swirl number for a difference in flowrate of 60% suggested that the swirl number for flame stabilization may be independent of the flowrate. As stated before, Yegian and Cheng [2] reported that blowoff limits occurred at a fixed swirl number independent of Φ. Figures 4-1 to 4-3 show that this is not universally true. However, at higher flow rates and energy inputs (e.g. stability limits at 80 kW in Figure 4-2), the limiting curves for blowoff and flashback are vertical. In this specific case, the stability range is independent of S_g for a range of Φ.

Figures 4-4 and 4-5 compare different measured stability limits for identical flow conditions and different burner geometries (burner exit sleeve length, L, and turbulence generator solidity, σ). The results did not show a major influence of these parameters in determining the stability limits of the tested burner. These results disagree with the observations reported in [2], regarding the length L. Nevertheless, they based their results on a jet type swirler where only air was injected through the tangential jets. In the current test, for the vane type swirler, all the mixing of fuel and air was done before the reactants entered the exit sleeve. This diminished the influence of the length. Also, for the same burner diameter, D, their change in L was from 20 to 120 mm (0.4 to 2.4 D), much larger than in this study, from 50 to 80 mm, (1 to 1.6 D). From a physical point of view, Cheng et al. [18] considered that L/U_∞ represented the transport time that outer (swirling) and inner flows have for mixing; and the swirl number needed for stable operation should be scaled independently using a constant residence time criterion. As a

conclusion, in this setup, moderate changes in L did not produce a substantial effect on stability limits, however in other configurations (e.g., burners with air-jet induced swirl), L/U_∞ may still be useful for scaling purpose.

For a perforated plate turbulence generator, the integral scale is approximately determined by the size of the holes [53], which in our case was the same (3.5 mm) for all the cases. This implied that only a drastic change in spacing between holes, affecting solidity, would impact significantly the stability limits. Thus, as observed in Figure 4-5, in the current range of tests, the choice of turbulence plate was not a critical parameter in determining stability limits.

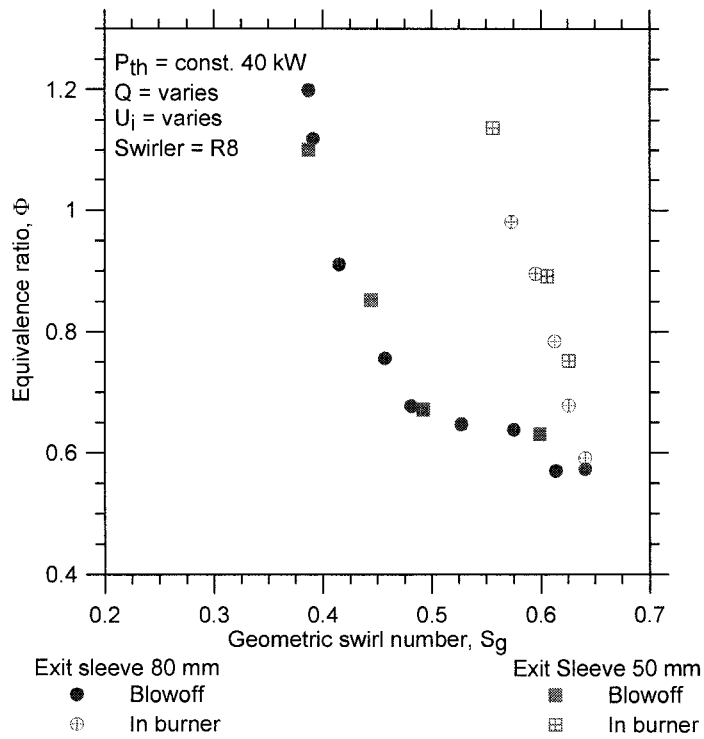

Figure 4-4 Flame stability regime: varied burner exit sleeve

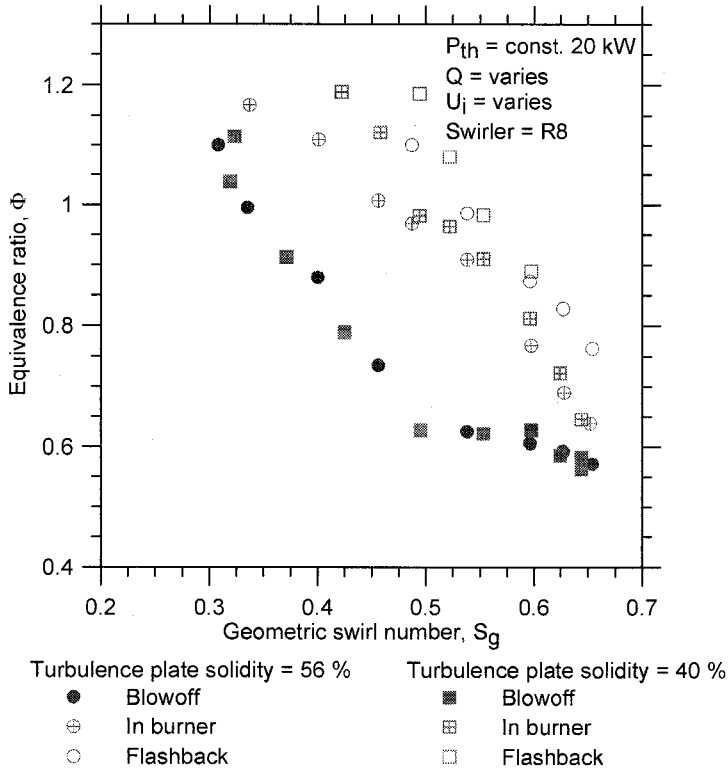

Figure 4-5 Flame stability regime: varied turbulent plate generator

As shown in Figure 4-6, reducing the inner diameter of the burner (increasing the depth of the annular swirl vanes) had a noticeable effect on the blowoff limit, but had no observable effect on the flashback limit at a fixed thermal input of 20 kW. It was noteworthy that in all Figures (1 through 6), the majority of the stable operating range occurred at swirl numbers below 0.6, which is often considered a characteristic threshold for the onset of swirl induced recirculation in the flowfield [38]. Also the value for the lean methane-air limit was very close to $\Phi = 0.57$, in agreement with Cheng [41].

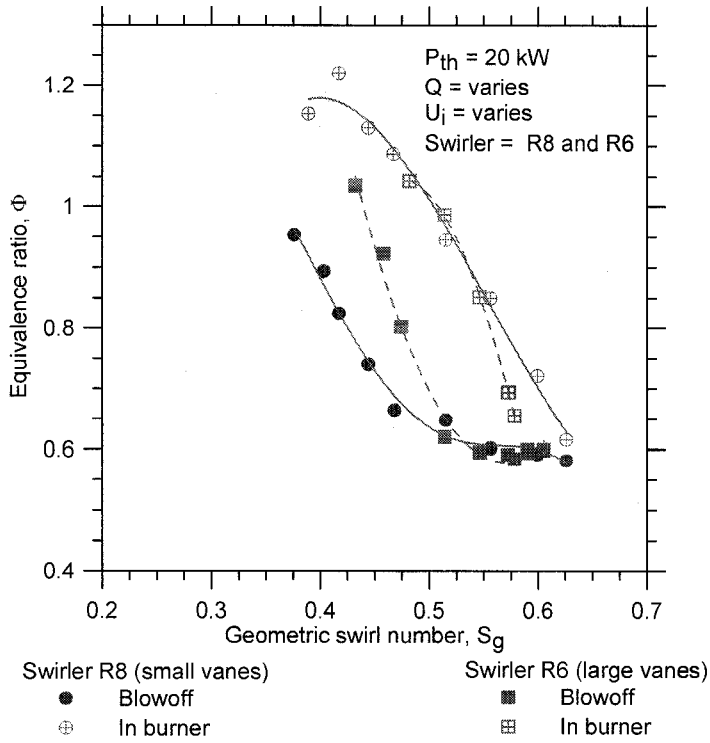

Figure 4-6 Flame stability regime: different swirler

4.2 Velocity field and flame position

Tables 4-1 and 4-2 show the range of flow measurements performed with the PIV system. Similar to the stability experiments summarized above, tests conducted helped isolate the effects of individual variables. Values of velocities obtained through PIV were compared to values determined by means of other methods, as explained in Appendix **E;** uncertainty of measurements.

Table 4-1 PIV measurements; no flame

Type of flow	Flowrate Q [slpm]	Φ				S_g			
		0	0.7	0.8	0.9	0.45	0.50	0.55	0.58
Non reacting	400	X X X X				X	X	X	X

Table 4-2 PIV measurements; with flame

Type of flow	Flowrate Q [slpm]	Φ				S_g			
		0	0.7	0.8	0.9	0.45	0.50	0.55	0.58
Reacting	400			X		X			
				X			X		
				X				X	
				X					X
	400		X					X	
					X			X	
	600			X				X	
	800			X				X	
	1200			X				X	

The mean velocity field in 3D along with the superimposed mean flame front contours are depicted in Figures 4-7, **a** through **d**, with only S_g varied. Vectors describe the in-plane velocity components U and V, and the background contour plot shows the out-of-plane component, W. From the figures it was clear that the central core flow was relatively one-dimensional, with no appreciable recirculation zone typical of high swirling flows, and there was an overall mean flow divergence upstream of the flame. This was in agreement with published data by Johnson et al. [3]. Two points of interest were observed, marked in Figure 4-7a as **I** and **II,** called the anchor points of the flame. These are points where the tangent to the flame edge is parallel to the horizontal axis, r. Anchor point two is particularly significant as it is the most upstream position of the mean flame front. Adjacent to Point I, almost all the velocity corresponded to the axial component, U (1D), whereas for the Point II, the velocity vector had appreciable axial and radial components, U and V (2D).

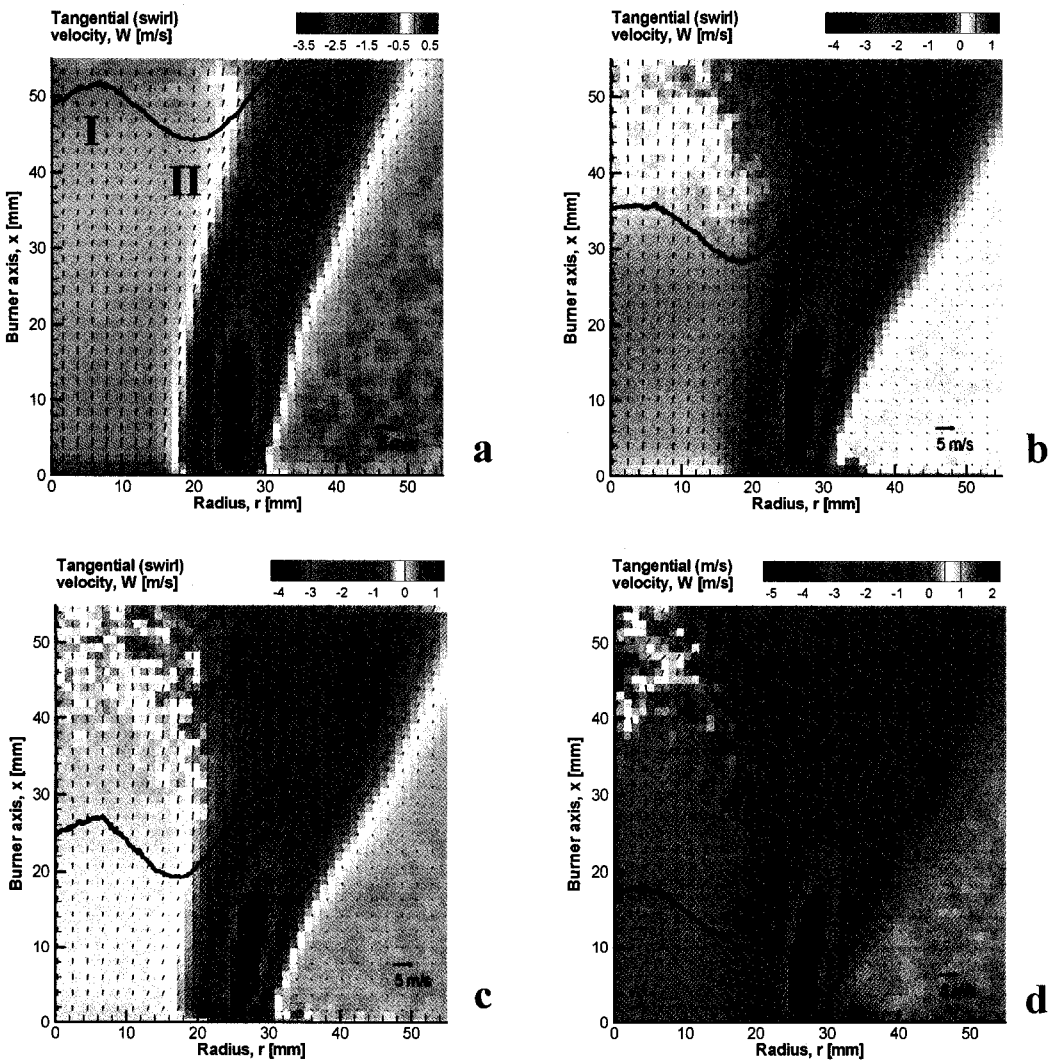

Figure 4-7 Effect of swirl number, S_g, in flame position and flowfield velocity

Mean flame contour superimposed on 3D flowfield. Q = 400 slpm, $\Phi = 0.8$, S_g varies

(**a**) $S_g = 0.45$; (**b**) $S_g = 0.50$; (**c**) $S_g = 0.55$; (**d**) $S_g = 0.58$.

Figure 4-8 allows a direct comparison among all the flame front positions in Figures 4-7, as swirl changed. For higher values of S_g, the freely propagating flame moved upstream toward the burner until it settled. The average component of velocity U, normal to the leading edge of the flame front (anchor point II) was similar in all four cases, with a value of 0.95 ± 0.05 m/s.

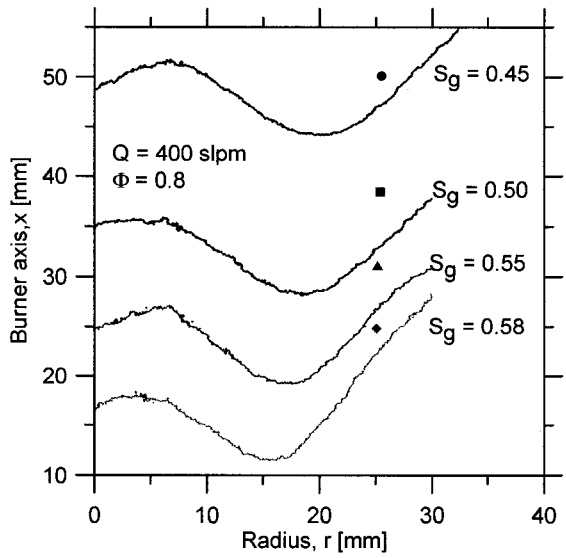

Figure 4-8 Flames position as swirl changes

Figures 4-9, **a** through **d**, show the effect of changing the equivalence ratio, Φ. Figure 4-9 a corresponds to non-reacting flow (Φ=0). For this case the flow was still divergent; however, the angle of the cone formed by the flow was much lower than for the combustion case. This result agreed with that of Littlejohn and Cheng [45], who presented the combustion zone as an aerodynamic blockage for the reactant flow.

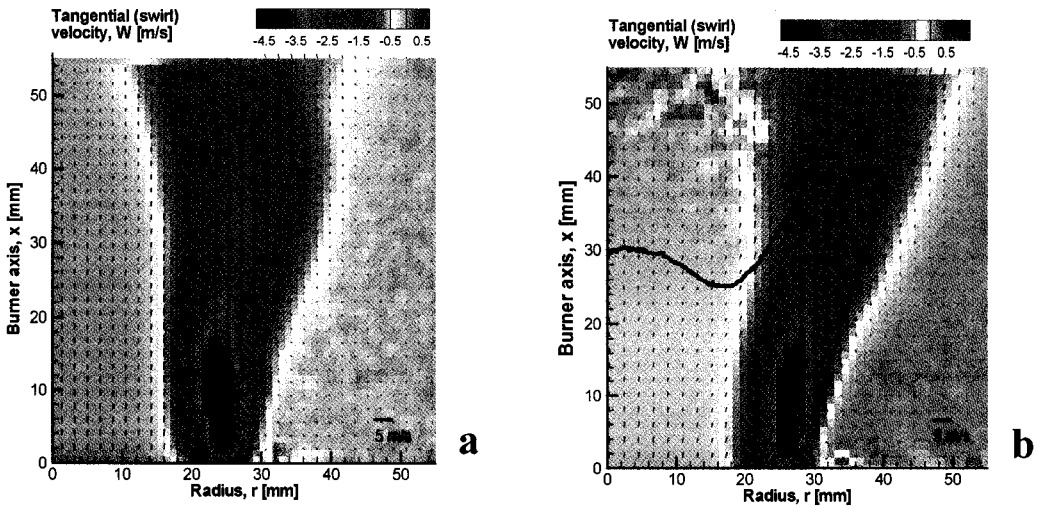

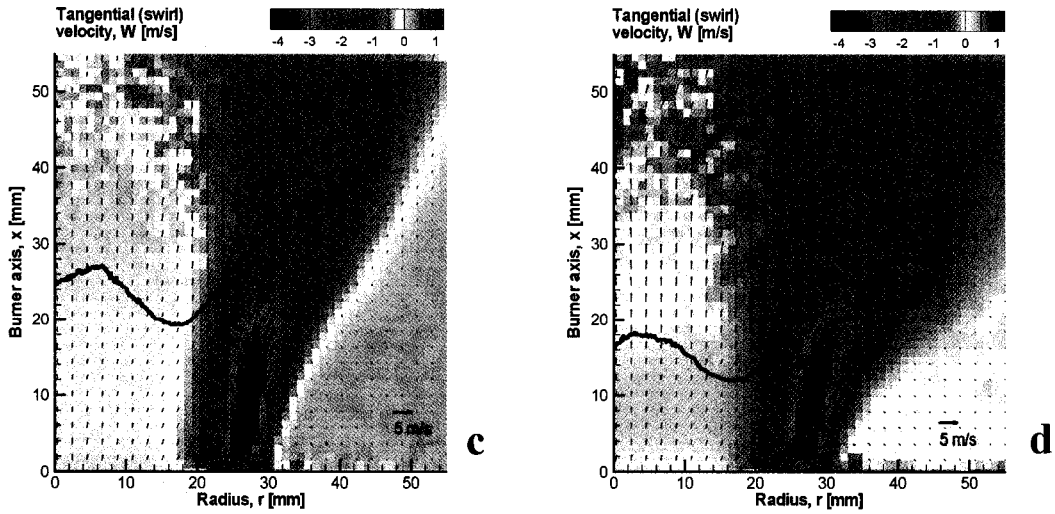

Figure 4-9 Effect of equivalence ratio, Φ, in flame position and flowfield velocity

Mean flame contour superimposed on 3D flowfield. Q = 400 slpm, S_g = 0.55, Φ varies (**a**) Φ = 0 (non-reacting); (**b**) Φ = 0.7; (**c**) Φ = 0.8; (**d**) Φ = 0.9.

The flame positions of Figures 4-9, **a** through **d**, plotted together on Figure 4-10, allow a direct comparison as Φ changed. The flame position varied with increased Φ, moving toward the burner exit and approaching flashback. The effect on flame displacement was equivalent to an augmentation in S_g. However, the physical nature of the phenomenon was different: the average component of velocity U at respective anchor points was not constant, but increased as Φ increased. For example, for anchor Point II the U component of velocity went from 0.65 m/s at Φ = 0.7 up to 1.11 m/s at Φ = 0.9. This was explained due to the higher value of S_T, at a higher value of Φ. As a result, the anchor point shifted upstream toward higher values of U for stabilization purpose.

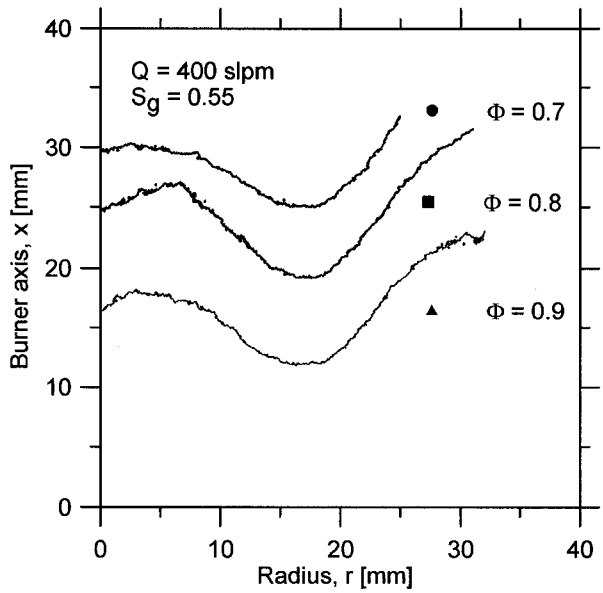

Figure 4-10 Flames position as equivalence ratio, Φ, changes

Figures 4-11, **a** through **d**, describe the effect as total flowrate, Q, was changed. Higher flowrates moved the flame away from the burner, and increased the tendency to blowoff. This displacement effect was opposite to the increase of S_g or Φ. There was also a considerable change in the shape of the flame.

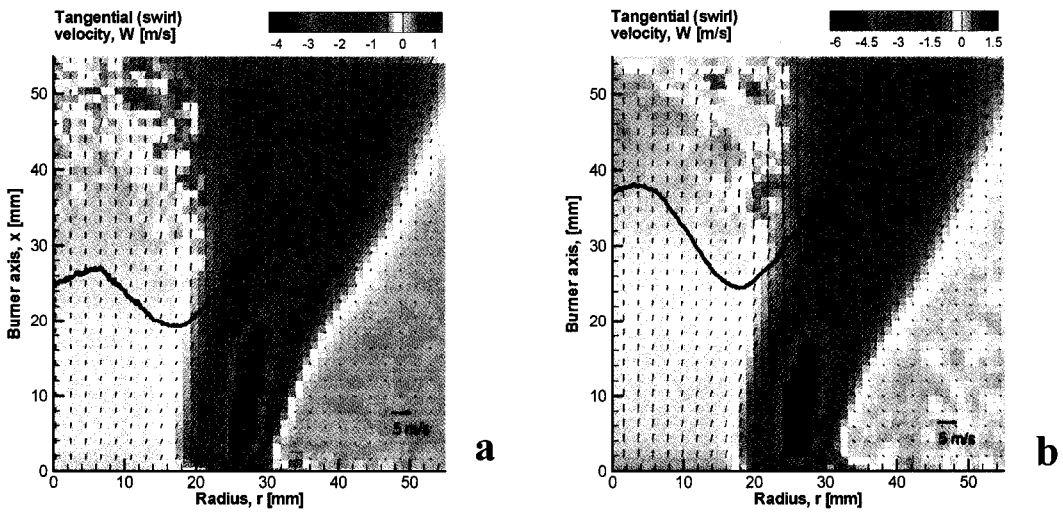

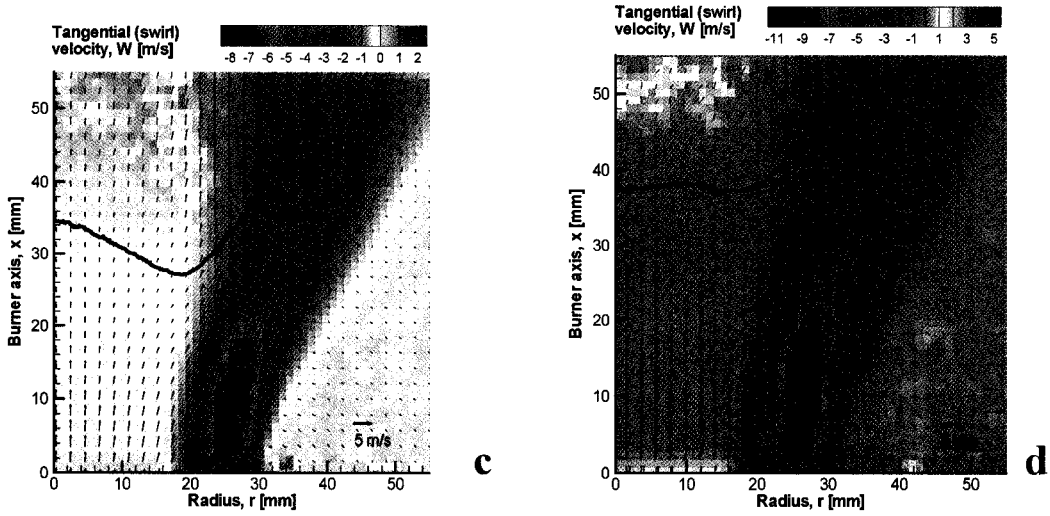

Figure 4-11 Effect of total flowrate, Q, in flame position and flowfield velocity

Mean flame contour superimposed on 3D flowfield. $S_g = 0.55$, $\Phi = 0.8$, Q varies

(**a**) Q = 400 slpm; (**b**) Q = 600 slpm; (**c**) Q = 800 slpm ; (**d**) Q = 1200 slpm.

The flame positions for varied Q are plotted together on Figure 4-12 for direct comparison. For the flow of 600 slpm, the central anchor Point I was above that of 800 slpm. This interesting result was believed to be a consequence of the increase in the flowrate. As the flow velocity increased, the flame tended to be pushed away from the burner. However, the increased flow rate also lead to an increase in the turbulence intensity, which had an opposite effect on flame position. The combination of both effects defined the position of the flame, which was not linear with the value chosen for Q. This result was in contrast to that reported by Littlejohn and Cheng [45], where the flame position did not change with different flow velocities. This difference could be due to differences in the performance of the turbulence generators between the two setups, which affected the final position of the flame.

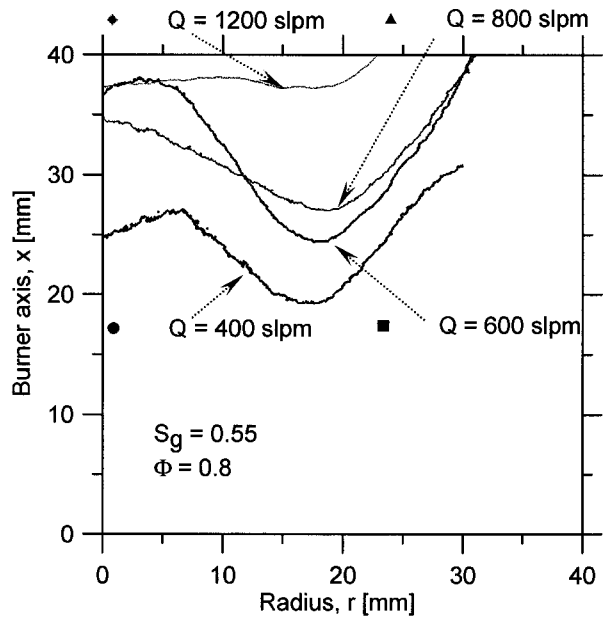

Figure 4-12 Flames position as total flowrate changes

Figures 4-13, 4-14 and 4-15 present the value of the tangential (swirling) velocity component, W, as a function of the radius of the burner. Each plot corresponds to the x-coordinate along the burner axis of the respective second anchor Point II of the flame, for that condition of S_g, Φ, and Q. On Figure 4-13 the effect of the decrease in S_g was a reduction in the value of W in the outer region, as expected, by the reduction in the value of the outer exit velocity. As the flame settled further downstream, the velocity peak was also displaced outward, which was due to the divergent nature of the flow. This condition was compared with the case on Figure 4-15. Here, at a constant S_g, an increase in flowrate, Q, moved the flame downstream, but as the core flow velocity increased due to higher Q, so did the outer velocity, so as to maintain S_g constant by keeping the ratio of inner and outer velocities fixed. Hence, the peak velocity increased instead. Also, due to flow divergence, the peak was displaced outward when the flame position moved downstream. As was stated, the value of W at the center core for all the figures was close

to zero. The comparison between reacting and non-reacting flow on Figure 4-14 confirmed the remark that the combustion phenomenon behaves as an aerodynamic obstruction to the flow, as described in [45].

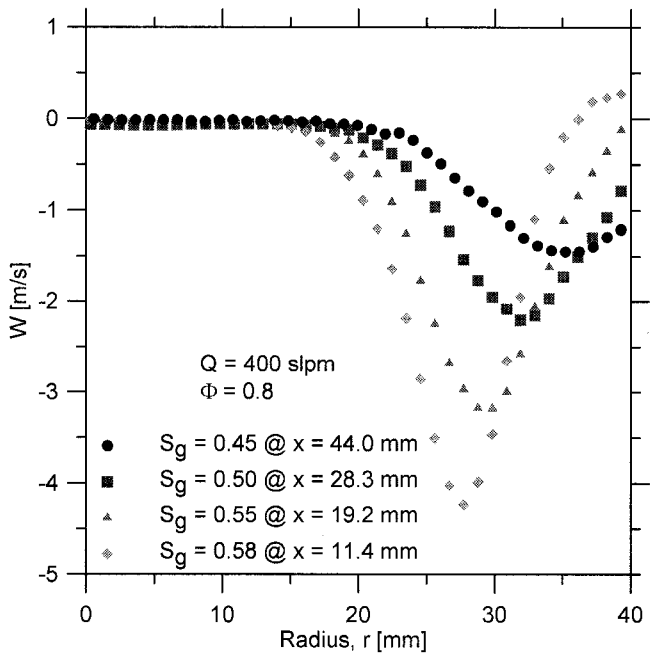

Figure 4-13 Tangential velocity component, W, for different S_g

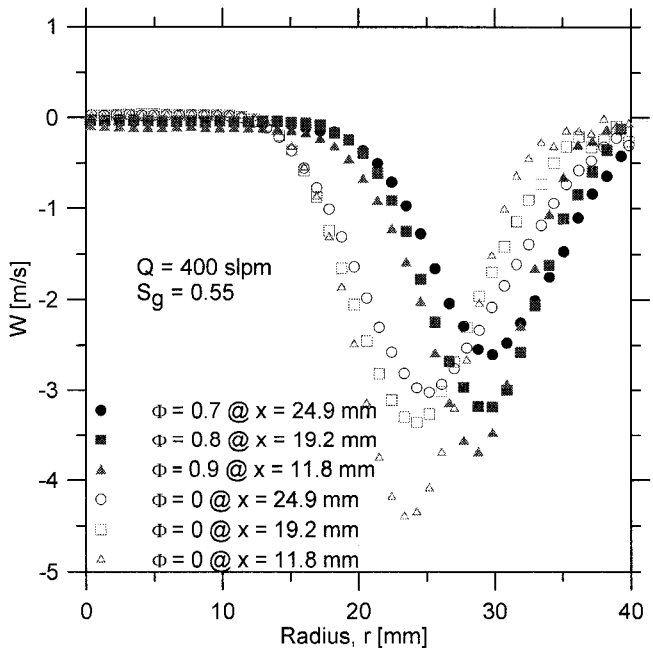

Figure 4-14 Tangential velocity component, W, for different Φ

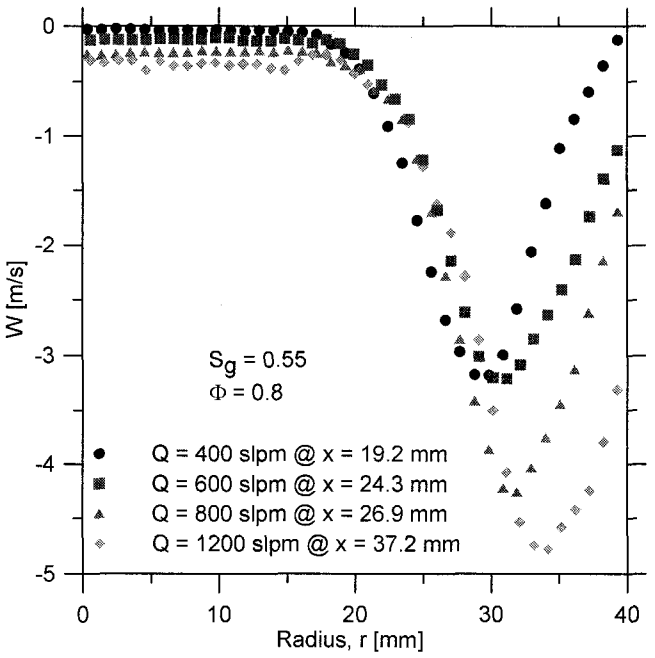

Figure 4-15 Tangential velocity component, W, for different Q

Chapter 5: Discussion and analysis

Figures 5-1, 5-2, and 5-3 show the normalized mean axial velocity component, *U/Uexit*, of the reactant flow corresponding to the radial location of anchor Point II, as a function of the burner axis, x. In each case, the curve has been drawn so that it ends at the position of the mean flame front contour.

Figure 5-1 shows, for constant Q and Φ, a similar rate of linear decay for all reacting cases. Surprisingly, changing the swirl number does not change the rate of decay. An exception corresponds to $S_g = 0.45$, which decelerates less quickly. However, this is an extreme condition for the lowest attainable value of swirl intensity immediately before inducing blowoff.

Figure 5-2 exhibits, for constant Q, and S_g, and for the non-reacting case ($\Phi = 0$) that the flow accelerates in the near field of the burner exit and reaches a peak, from where linear decay initiates. At the value of S_g plotted, the velocity in the vane section is considerably higher than in the core flow. Since the radial coordinate of the graph corresponds to anchor Point II, very close to the outer annulus, it is inferred that the flow is initially accelerated as it leaves the burner when it mixes with the outer flow. The flow velocity then reaches a maximum from where the decay initiates.

The reaction zone acts as an aerodynamic blockage, which decelerates more rapidly the incoming flow, as observed for the reacting cases. However, this type of blockage is

a different phenomenon than the blockage produced by a physical obstruction inserted in the flowfield; such as a bluff body. In combustion, it is the volume expansion of the hot gases that induces the blockage effect observed. Analyzing the reacting flows, as Φ increases, so does the rate of deceleration of the flow, hence the flow blockage effect is proportional to combustion intensity.

Figure 5-3 illustrates, for fixed Φ and S_g, a similar degree of initial deceleration for higher flowrates (Q = 600, 800, and 1200 slpm). The rate of deceleration for Q = 400 slpm is slightly larger, possibly an indication of a different flow regime.

Littlejohn and Cheng [45], in their most recent paper, report experimental results on a low-swirl burner with fixed inner to outer flow ratio, hence, fixed value of S_g. They show that under these conditions, for different values of Q and Φ, there was a consistent degree of linear decay along the centerline, and the flame brush remains stationary within the flow with increasing values of U. Such a stationary position can be useful for scaling the burner among different applications. However, as noted above, the current results show that the flow characteristics are not necessarily so simple. While the rate of decay of velocity is linear at the burner exit, the slope is not consistent for all cases. Moreover, the flame position is found to vary with both Q and Φ even when the swirl number is fixed, in contrast with [45].

It is important to note that the current burner differs from that of [45], in that it permits variations of S_g through the independent control of inner and outer flow, which are separated through the inner and outer nozzle. The differences in flame shapes from the "W", observed predominantly in the present experiments, and the relatively flat

central profile, reported by [45], is attributable to variations in S_g. Differences could also be attributed to dissimilar performance of the turbulence generator for each case, which influences S_T and the final shape of the flame. Nevertheless, the behaviour of the reacting zone, similar to a blockage in the reactants stream, is in agreement with [45]. Overall, Figures 5-1 to 5-3 show that for a fixed Φ, the swirl number scales the rate of flow deceleration upstream of the flame for different flowrates, Q. However, the mean position of the flame is not dictated by these parameters alone.

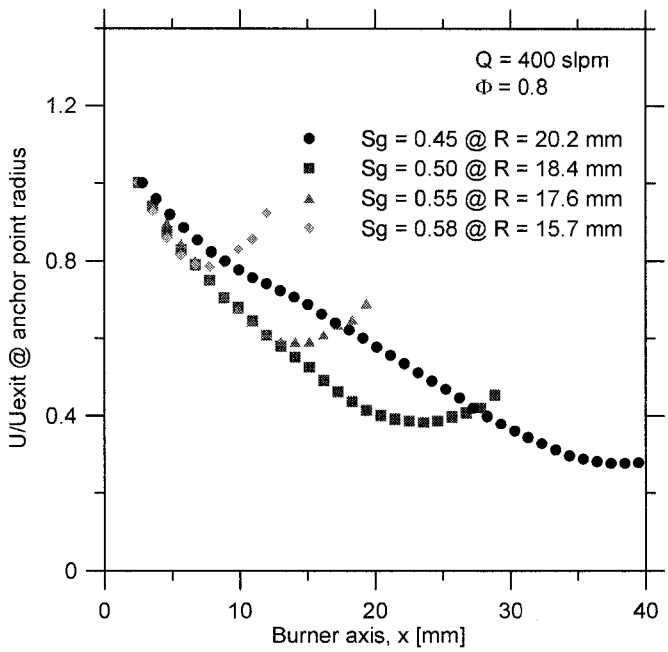

Figure 5-1 Decay of the normalized velocity component, U, for different S_g

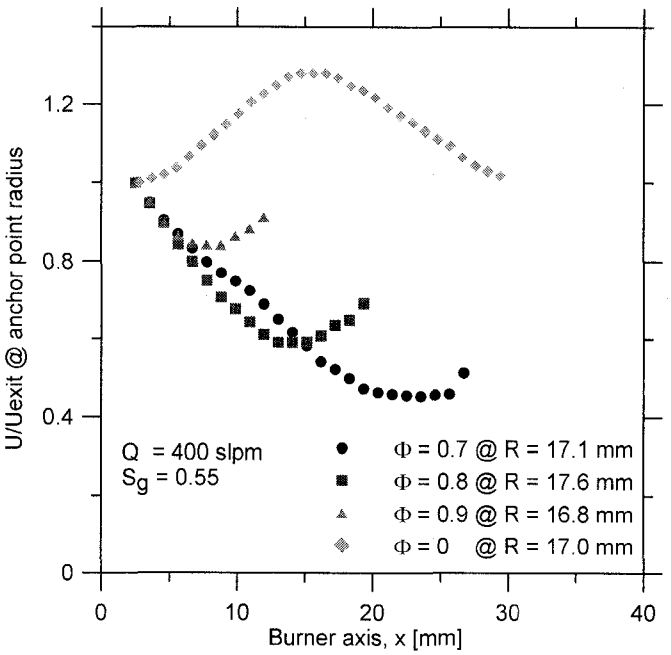

Figure 5-2 Decay of the normalized velocity component, U, for different Φ

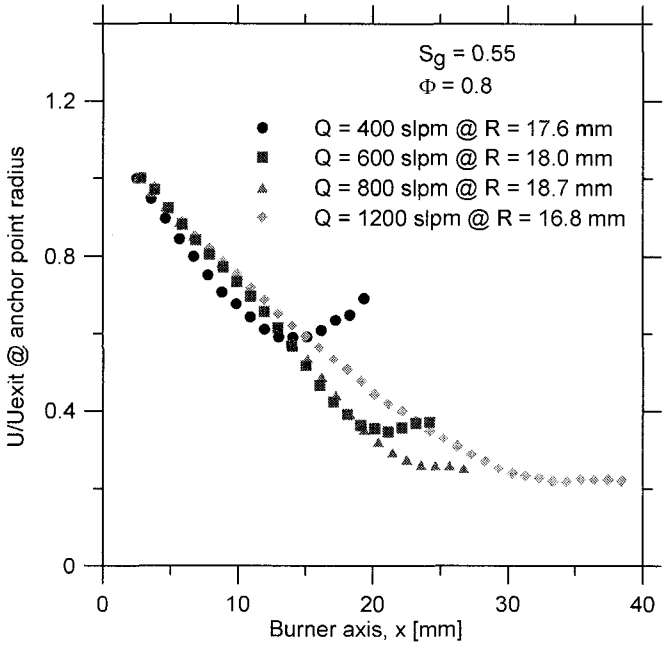

Figure 5-3 Decay of the normalized velocity component, U, for different Q

Figures 5-4, 5-5, and 5-6 represent the magnitude of the mean axial velocity component *U* along the x-direction, from the burner exit to the flame location, at a fixed radial

position corresponding to the location of the flame anchor Point II. Figure 5-4 shows, for constant Q and Φ, that the position of the flame along the x-axis is shifted until a similar value of U, approximately 0.95 m/s, is achieved in all cases. As expected, if Q is held constant while swirl is increased by diverting more flow to the outer annulus of the burner, the exit velocity in the core region decreases considerably at the burner exit. In Figure 5-5, for constant Q and S_g, the velocity of reactants entering the flame does vary. This is understandable since S_T varies with S_L which is a function of Φ.

As explained above, the initial acceleration of the flow in the non-reacting case is due to mixing with the faster moving annular flow. However from Figure 5-5 it is apparent that in the reacting cases, the increased divergence pushes the annular flow radially outward so that for the same fixed radial position, the plotted vertical velocity contours show only a simple linear decay. This decay showed a more pronounced slope compared with the non-reacting cases. This increased deceleration is attributable to the aerodynamic blockage effect caused by the volume expansion through the flame.

Figure 5-6 shows, for fixed values of S_g and Φ at anchor Point II, that the value of U at the flame position, is similar for lower flowrates (Q = 400, 600, and 800 slpm). The different value of U at the flame position for the highest exit velocity (at a flowrate Q = 1200 slpm), suggests that the value of S_T is affected by a higher level of turbulence for that flow regime.

Comparing Figure 5-4 with Figure 4-8 (flame positions as swirl changes), it is expected that since swirl creates a divergent flow, as swirl increases, the divergence angle increases. Then, the slope of the velocity decay should be steeper for higher swirl numbers. Nonetheless, the flame positions for different S_g show that the qualitative

change in flow divergence angle is not significant. This surprising result suggests that the main effect from a change in swirl values is not a change in flow divergence but a significant variation in core flow velocity where all anchor points are located.

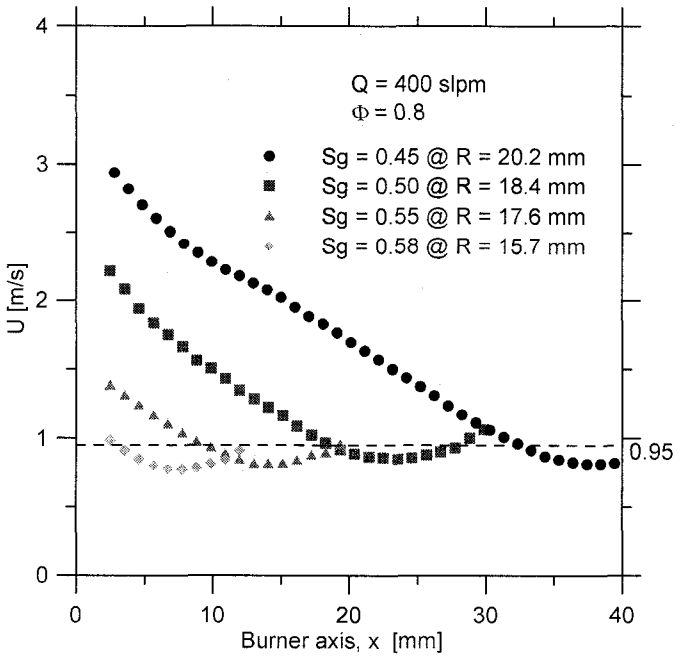

Figure 5-4 Decay of the velocity component, U, for different S_g

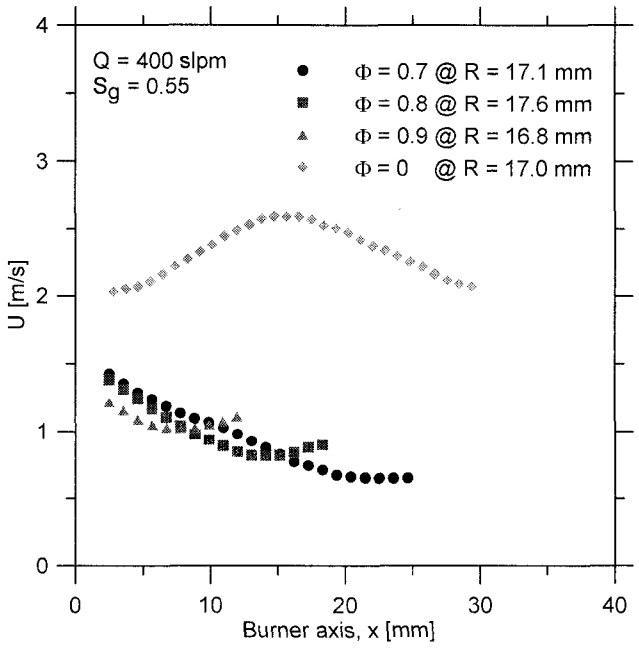

Figure 5-5 Decay of the velocity component, U, for different Φ

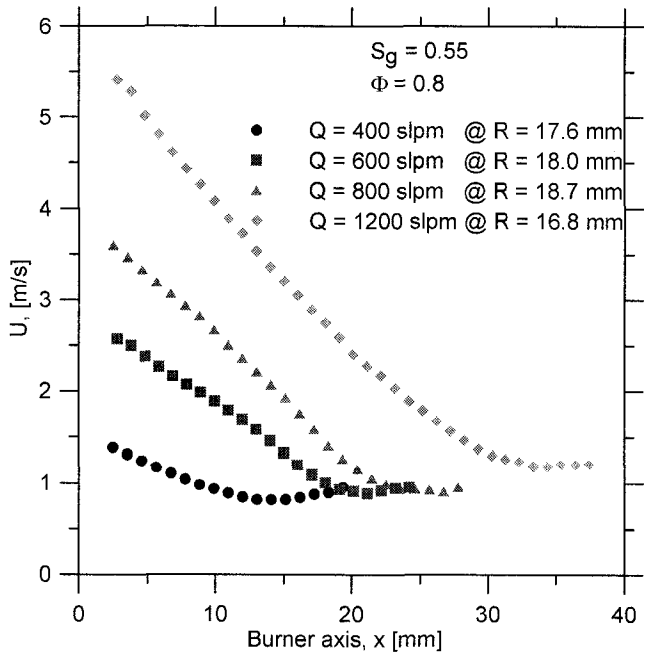

Figure 5-6 Decay of the velocity component, U, for different Q

In Figure 5-7, the mean axial velocity component U corresponding to anchor Point II at radius coordinate (18.4 mm), is plotted on the same graph along with the mean flame front contour for that particular flow condition (S_g = 0.5, Q = 400 slpm, Φ= 0.8). The intersecting point corresponds to the value of S_T at that anchor point. For reference, this velocity profile is one of the four plotted in Figure 5-4. From the observation of the velocity curve shape, an interesting conclusion is that the same value of U corresponding to the anchor point is found previously at an x-coordinate close to 20 mm.

After the decay previously analyzed, and from a minimum value, U increases shortly until it reaches the anchor point of the flame. Re-examination of previous Figures, 5-1 to 5-6 for reacting cases, shows the same trends. This effect is moderated as the position of the flame moves downstream, as shown in Figure 5-3. This phenomenon can be attributed to a higher degree of influence of the flame, on mean characteristics of the

upstream reactant flow. This differs partially from [45], where the same shape of velocity curves are reported, but the leading edge of the turbulent flame zone is always considered where profiles deviate from a linear decay trend. As stated by Chan et al. [1], the flame speed, S_T, can be estimated according to the flow velocity vector, which is locally normal to the flame brush. As explained by [45], the stabilization mechanism of the LSB relates directly to the value of S_T. This is because the flame settles where the mean flow velocity is equal and opposite to S_T. Hence, the value of U in the flow is representative of the value of S_T.

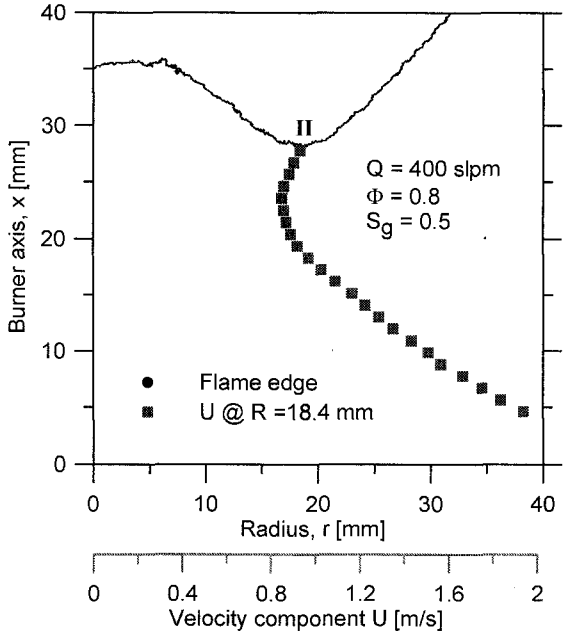

Figure 5-7 Flame front contour superimposed on velocity component U

Figures 5-8, 5-9, and 5-10 depict the values of the mean axial velocity component U plotted against increasing radius, at the burner axis x-coordinate of the particular anchor Point II for each condition. In Figure 5-8, for fixed Q and Φ, and in the core flow region up to a radius of 18 mm, velocity profiles collapse onto each other. However, this is not the result of a drastic change in flow divergence, but a confirmation that the decay

observed in Figure 5-4 for the radial coordinate of anchor Point II, is extended along the core region.

Beyond approximately 18 mm, the value of U increases substantially, affected directly by the action of the outer flow. As expected, the peak of U is lower as S_g is decreased; however, the peak is also displaced outward. This is due to the change in the ratio of outer and inner velocities, necessary to change the value of S_g, which implies an increase in the inner velocity and its influence, as the outer velocity decreases.

Figure 5-9 shows, for reactant flow with fixed values of Q and S_g in the central region, that the value of U increases according to an increment in Φ. This is attributed to the effect of an increase in combustion intensity, due to the change in Φ. This graph portrays how the flame propagates in each case, until the new value of S_T, affected by Φ, matches the local flow velocity. In addition, the peaks of velocity increase as Φ increases, however the radial coordinate is the same because Q and S_g do not affect the flowfield. For the case of $\Phi = 0$, there is a displacement of the velocity profile inward, which is expected as there is no flame to block the stream of reactants.

In Figure 5-10, for constant S_g and Φ at different Q, the velocity profiles in the central region are quite similar, as it is observed in Figure 5-8 where Φ is fixed too. In the outer region, the values of the peak velocities are higher, and are displaced outward as Q increases. This is because an increase in Q with fixed swirl, increases the inner and outer velocity to keep the same ratio between both and a constant S_g. The velocity profiles in Figure 5-10 have all a similar radial gradient before the peak value for each of the flows.

In general, a similar effect on flame displacement is generated by an increase in Q or a decrease in S_g: the flame moves downstream. Nevertheless, the different characteristics of both flowfields produce different flame shapes, as previously observed in Figures 4-8 and 4-12.

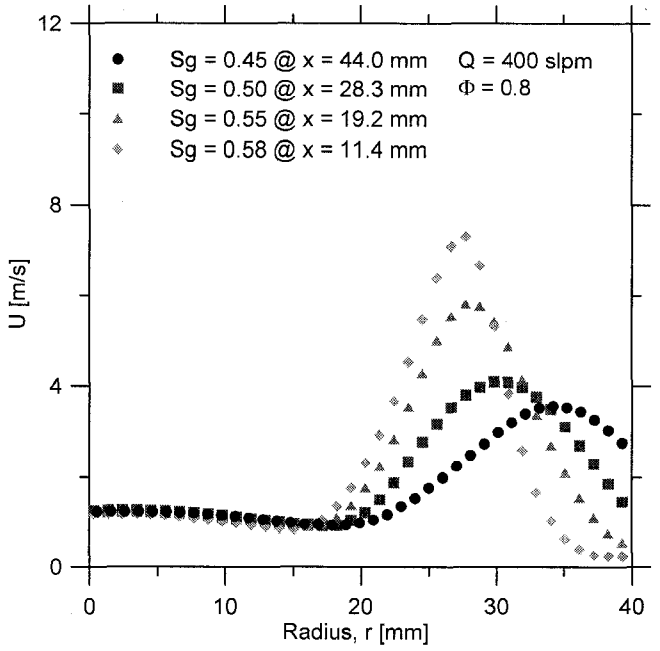

Figure 5-8 Radial variation of the velocity component, U, for different S_g

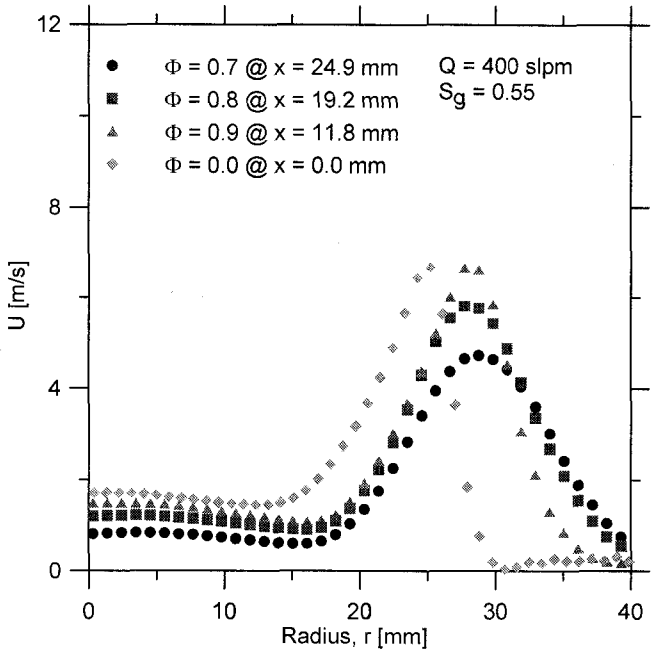

Figure 5-9 Radial variation of the velocity component, U, for different Φ

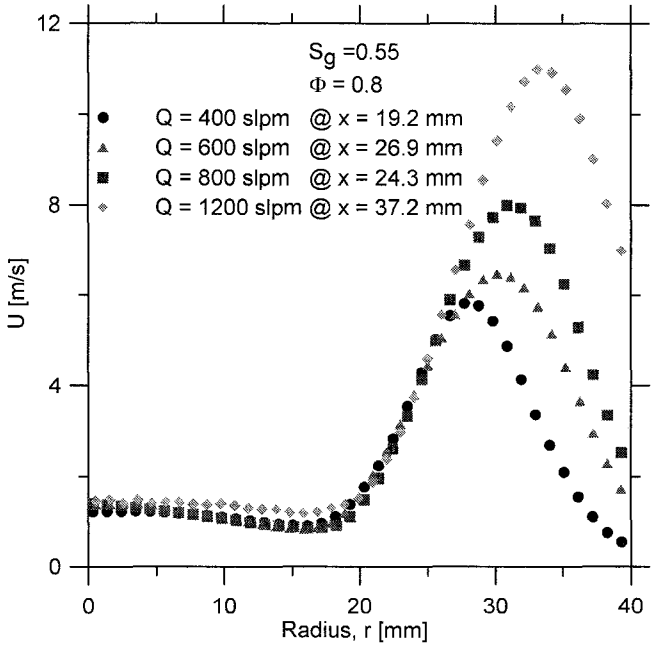

Figure 5-10 Radial variation of the velocity component, U, for different Q

Figures 5-11, 5-12, and 5-13 show the turbulence velocity component u' vs. radius at the x-coordinate of the respective anchor Point II.

Figure 5-11 illustrates, for constant Q and Φ, a similar value for u' in the central region for all cases. There is a change in inner velocity for different values of S_g, however, it seems that the magnitudes of these changes are not high enough to affect u'. Close to the boundary region between inner and outer flow there is a sudden increase in u'. In this region, the change in the ratio of velocities for the different values of S_g , has a major effect on u'. This is because in the central region turbulence is generated by a turbulence plate; in the external region it originates from the interaction between inner and outer flows, where strong velocity gradients exist. Also, as swirl increases, the curve for u' develops two peaks corresponding to shear layers created; one with the central core flow, and the other with the surrounding flow from the environment.

In Figure 5-12, for Q and S_g fixed, the major effect between reactant flows is the increase in u' in the outer region which correlates with an increase in combustion intensity.

In Figure 5-13, for constant S_g and Φ, an increase in Q magnifies u' along the whole flowfield; but the change is more noticeable in the outer region. This is because when Q increases while S_g is fixed, the difference between inner and outer velocities amplifies, in spite of the fact that their ratio is fixed. Then, the velocity gradient is greater which produce an increase in u'. The central region shows a clear positive correlation between Q and u'. However, in contrast with [45], their relationship is not linear. The effect of a change in Q on flame position, mainly through the variation in U and u', was outlined in

Chapter 4; while an increase in U displaces the flame downstream, an increase in u' has opposite effect due to the increase in S_T.

As described in Chapter 1 the value of S_T is a function of S_L and u'. For the case of Figure 5-4, Φ is constant and S_L is approximately constant as well. Then, if the value of u' is similar for homologous anchor points (e.g., among all anchor Points II), the resulting S_T is expected to be similar for all of them. As observed, the comparison of the mean velocity U, representative of S_T, for each of those points, results in a similar value of 0.95 m/s $\pm$ 0.05 m/s. In Figure 4-8, it is observed that the radial coordinate of anchor Points II is between 16 and 20 mm. For each of these coordinates the values of u', from Figure 5-11 is also similar, in the order of 0.36 m/s. These values of u' are almost twice the value of u' on the central core due to the shear layer created between inner and outer core. This affects the value of S_T, the shape and position of the flame, and stability limits.

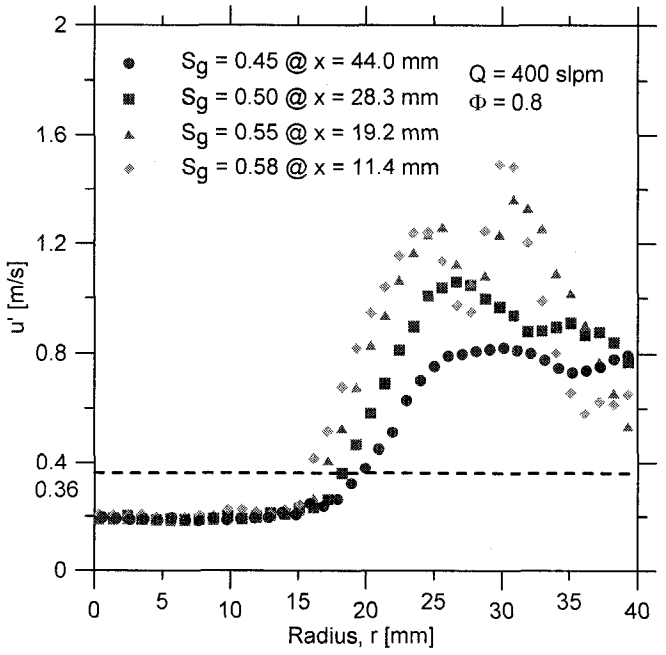

Figure 5-11 Radial variation of the turbulent velocity component, u', for several S_g

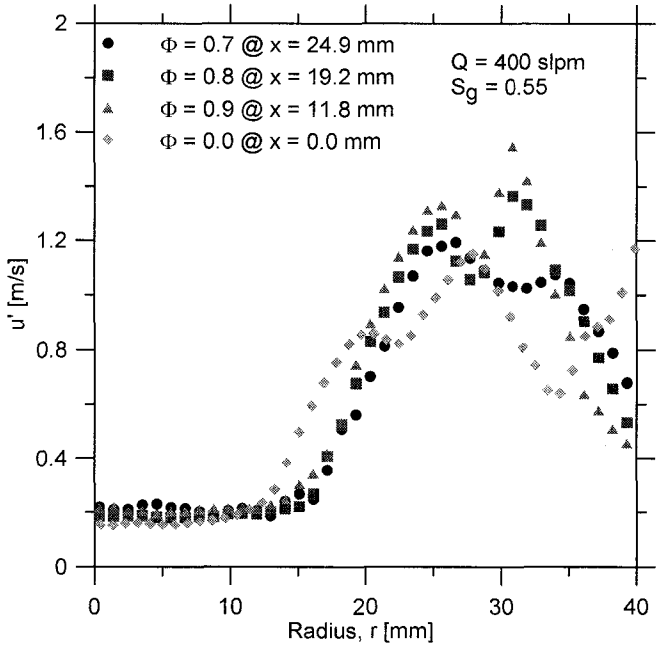

Figure 5-12 Radial variation of the turbulent velocity component, u', for several Φ

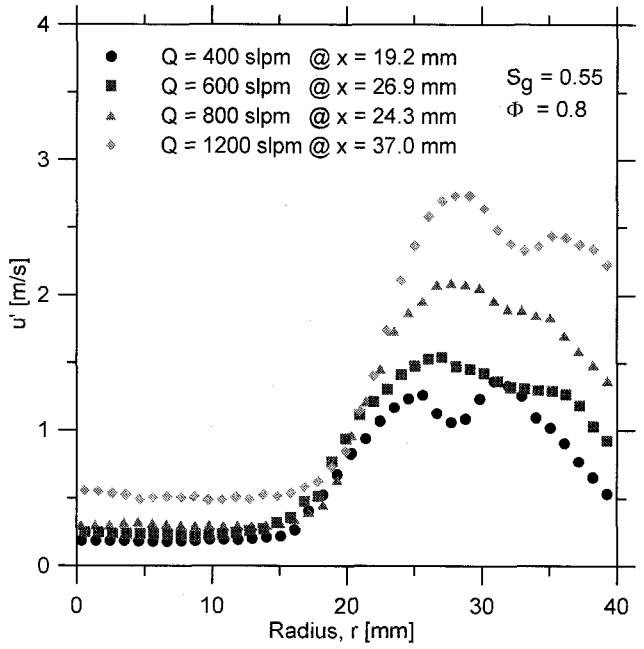

Figure 5-13 Radial variation of the turbulent velocity component, u', for several Q

The comparison of the results of the mean reactant velocity component U along the same flame front shows a higher value for anchor Point I (at the center) than for anchor Point II. This can not be explained only by the effect of the turbulence velocity component u', which is plotted in Figures 5-11 to 5-13, and is higher for anchor Point II than for anchor point I. Very likely other factors should be assessed in this comparison due to the different features of the flowfield between anchors points I and II. In Chapter 1, the expression for S_T from [27] includes the variables used to define the Karlovitz number; namely, turbulence intensity, integral length scale, laminar flame thickness, and laminar flame speed. It is believed that some of these variables may have an impact on the final result of S_T. Besides this, the value of S_L is not only dependent on Φ and the type of fuel, but also a function of the flow properties, which includes flame curvature, velocity gradients and recirculation as stated in [4].

The determination of the turbulent burning velocity is not completely elucidated yet. Filatyev et al. [63] show, for a Bunsen burner, that S_T is also a function of the mean velocity (measured as the mass flow rate of reactants divided by the burner exit area and the reactant density); besides being a function of turbulence intensity.

Scaling

Data collapse is a well known method of establishing scaling and determining associated parameters in problems showing self-similar attributes. In the current study, many attempts were tested based on this methodology. As it is shown in Chapter 4 by means of the stability maps for constant thermal input, constant total flowrate, and constant inner velocity, the swirl number S, represented by S_g, is not a definitive single scaling parameter. Likewise, through the stability maps for constant flowrates, it is concluded that a constant velocity criterion can not be used alone for scaling purpose either. The shear layer created at the boundary between the inner and outer flow is a function of the difference in velocities $[U_i - U_o]$, and affects the location of anchor Point II, flame position, and stability. If only S_g is kept constant, the ratio $[U_i/U_o]$ is constant, but a change in U_∞ affects $[U_i - U_o]$, and the shear layer. At U_∞ constant only, a change in S_g represents a change in $[U_i/U_o]$ and in $[U_i - U_o]$.

Cheng et al. [18] propose a constant velocity criterion for scaling the burner diameter to accept higher thermal inputs. However, the authors consider that the swirl number needed for stable operation should be scaled independently, using a constant residence time criterion. According to the results in this thesis for a vane type LSB, only the first

condition could be validated. Hence, for scaling the swirl number, the value of S_g is required from experimental results.

The scaling of a vane type burner for a certain fuel and thermal input power should consider geometrical similarity, constant velocity criterion, and swirl number for safe operation. Emissions limits are contemplated for the selection of Φ. Figure 5-14 and Table 5-1 illustrate three stability regimes: Q = 400, 800, and 1600 slpm that are determined in this study.

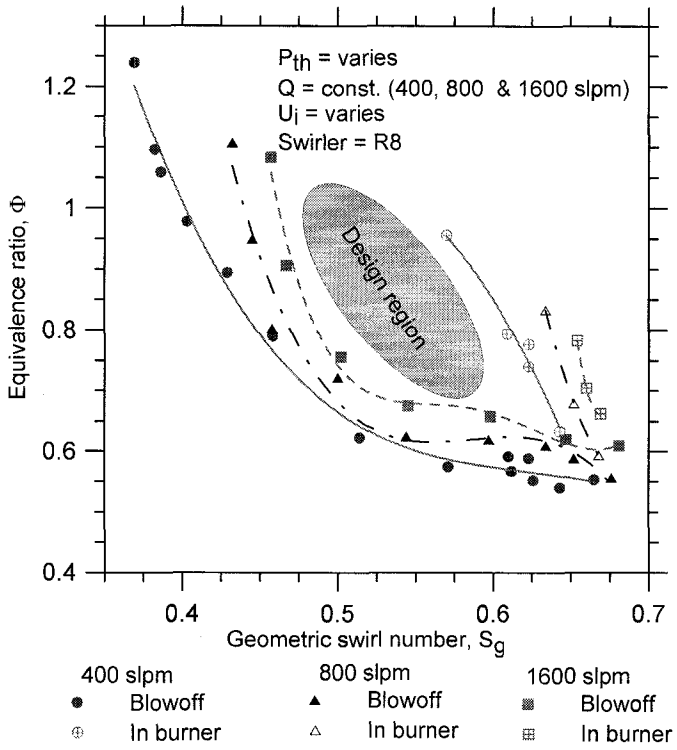

Figure 5-14 Stability regimes and design region; air-methane mixture

Table 5-1 Parameters for corresponding flowrates

Flowrate Q [slpm]	U_∞ [m/s]	Power range P_{th} [kW]
400	3.7	14 - 30
800	7.4	29 - 54
1200	14.8	63 - 107

Chapter 6: Conclusions

Stability limits (flashback and blowoff) of a low-swirl burner (LSB) were determined for a wide parametric range of flowrates, swirl number, S_g, and equivalence ratio, Φ. Although the swirl number was verified to be a critical parameter in describing the flow, it alone can not be used as a single scaling parameter.

Stereoscopic particle image velocimetry (PIV) was used to map the 3D velocity field and to quantify the mean flame position. Through numerical integration, the geometric swirl number S_g was verified as an appropriate surrogate for the actual swirl number S of the flow.

The results also confirmed that flames of the LSB stabilize as freely propagating turbulent flames. However, the volume expansion through the flame, rather than the swirling action of the flow, was shown to be responsible for creating the observed divergent flowfield. The flame then settles locally where the turbulent burning velocity S_T equals the normal velocity component of the reactants. Flowfield velocity measurements suggest that the major effect of swirl is through the change of mean axial velocities and turbulence intensities which directly influence the position of the flame and its stability limits. In the central core flow, the flame position moves away from the burner as the reactant velocity is increased and moves toward the burner as the turbulence intensity increases. At the interface between the central core flow and outer swirling

flow, the induced shear layer creates high levels of turbulence, which directly influence the location of the so-called anchor point of the flame. The idea that a change in swirl implies a major change in flow divergence was shown not to be true.

The swirl number needed for stable operation should be scaled independently using stability results obtained through experimentation. Attempts were performed to collapse the stability limit curves of constant thermal input power, for scaling purpose. While no universal scaling laws were found, through the analysis of Chapter 5 it was inferred that both the amount of swirl and the absolute difference between the inner and outer flow velocities are responsible for flame stability. For practical purposes, it is concluded that fixing S_g and total velocity through the burner is one of the valid approaches for scaling the burner, to accept higher thermal inputs.

References

[1] C. K. Chan, K. S. Lau, W. K. Chin and R. K. Cheng, "Freely propagating open premixed turbulent flames stabilized by swirl," *Proceedings of the 24th International Symposium on Combustion,* pp. 511-518, 1992.

[2] D. T. Yegian and R. K. Cheng, "Development of a lean premixed low-swirl burner for low NOx practical applications," *Combustion Sci. Technol.,* vol. 139, pp. 207-227, 1998.

[3] M. R. Johnson, D. Littlejohn, W. A. Nazeer, K. O. Smith and R. K. Cheng, "A comparison of the flowfields and emissions of high-swirl injectors and low-swirl injectors for lean premixed gas turbines," *Proceedings of the Combustion Institute,* vol. 30, pp. 2867-2874, 2005.

[4] S. R. Turns, *An Introduction to Combustion: Concepts and Applications.* McGraw-Hill, 2000.

[5] R. Stone, A. Clarke and P. Beckwith, "Correlations for the laminar-burning velocity of methane/diluents," *Combust. Flame,* vol. 114, pp. 546-555, 1998.

[6] J. Abraham, F. A. Williams and F. V. Bracco, "A discussion of turbulent flame structure in premixed charges," *SAE paper 850345*, 1985.

[7] R. Strehlow, *Combustion Fundamentals.* McGraw-Hill, 1985.

[8] E. E. Zukoski and F. E. Marble, "The role of wake transition in the process of flame stabilization on bluff bodies," *Combustion Research and Reviews,* pp. 167-180, 1955.

[9] D. Feikema, R. H. Chen and J. F. Driscoll, "Enhancement of flame blowout limits by the use of swirl," *Combust. Flame,* vol. 80, pp. 183-195, 1990.

[10] LaVision, *DaVis FlowMaster Software.* Goettingen, GmbH, 2006.

[11] International Energy Agency, *Key World Energy Statistics.* Paris, France, 2006.

[12] D. Littlejohn, A. J. Majeski, S. Tonse, C. Castaldini and R. K. Cheng, "Laboratory investigation of an ultra low NOx premixed combustion concept for industrial boilers," *Proceedings of the Combustion Institute,* vol. 29, pp. 1115-1121, 2003.

[13] J. A. Miller and C. T. Bowman, "Mechanism and modeling of nitrogen chemistry in combustion," *Progress in Energy and Combustion Science,* vol. 15, pp. 287-338, 1989.

[14] K. K. Kuo, *Principles of Combustion.* Second ed., John Wiley & Sons, 2005.

[15] C. K. Law, *Combustion Physics.* Cambridge University Press, New York, 2006.

[16] C. T. Bowman, "Control of combustion-generated Nitrogen oxide emissions: Technology Driven by Regulations," *Symp. Int. Combust.,* pp. 859-878, 1992.

[17] S. M. Correa and M. D. Smooke, "NO_X in Parametrically Varied Methane Flames," *Symp. Int. Combust.,* pp. 289-295, 1990.

[18] R. K. Cheng, D. T. Yegian, M. M. Miyasato, G. S. Samuelsen, C. E. Benson, R. Pellizzari and P. Loftus, "Scaling and development of low-swirl burners for low-emission furnaces and boilers," *Proceedings of the Combustion Institute,* vol. 28, pp. 1305-1313, 2000.

[19] A. H. Lefebvre, *Gas Turbine Combustion.* Taylor & Francis, 1999.

[20] I. Glassman, *Combustion.* Academic Press, 1996.

[21] B. Karlovitz, D. W. Denniston, D. H. Knapschaffer and F. E. Wells, *Symp. Int. Combust.,* pp. 613, 1953.

[22] B. Lewis and G. Von Elbe, *Combustion, Flames and Explosion of Gases.* Academic Press, Orlando Florida, USA, 1987.

[23] M. Metghalchi and J. C. Keck, "Burning velocities of mixtures of air with Methanol, Isooctane, and Indolene at high-pressure and temperature," *Combust. Flame,* vol. 48, pp. 191-210, 1982.

[24] N. Peters, *Turbulent Combustion.* Cambridge University Press, 2000.

[25] K. K. Kuo, *Principles of Combustion.* First ed., John Wiley & Sons, 1986.

[26] G. Damköhler, "The effect of Turbulence on the Flame Velocity in Gas Mixtures," *Zeitschrift Electrochame,* vol. 46, pp. 601-626, 1940, (English Translation NACA TM 1112, 1947).

[27] N. Peters, "The turbulent burning velocity for large-scale and small-scale turbulence," *J. Fluid Mech.,* vol. 384, pp. 107-132, 1999.

[28] T. Plessing, C. Kortschik, N. Peters, M. S. Mansour and R. K. Cheng, "Measurements of the turbulent burning velocity and the structure of premixed flames on a low-swirl burner," *Proceedings of the Combustion Institute,* vol. 28, pp. 359-366, 2000.

[29] A. M. Klimov, "Laminar flames in a turbulent flow," *Zhur. Priki. Mekh. Tekhn. Fiz.,* vol. 3, pp. 49-58, 1963.

[30] F. A. Williams, "Criteria for existence of wrinkled laminar flame structure of turbulent premixed flames," *Combust. Flame,* vol. 26, pp. 269-270, 1976.

[31] G. L. Borman and K. W. Ragland, *Combustion Engineering.* McGraw-Hill, 1998.

[32] J. M. Beér and N. A. Chigier, *Combustion Aerodynamics.* Applied Science Publishers Ltd, 1972.

[33] A. M. Kanury, *Introduction to Combustion Phenomena.* Gordon and Breach Science Publishers, 1975.

[34] T. A. Bovina, "Studies of exchange between the recirculation zone behind the flameholder and the outer flow," *Symp. Int. Combust.,* pp. 692, 1958.

[35] I. V. Bespalov, "Physical principles of the working process in combustion chambers of jet engines by Raushenbakh et al. translated from Russian," *Clearinghouse for Federal Scientific and Technical Inform., USA,* pp. 366, 1967.

[36] J. Jun and J. R. Gore, "Flow structure in lean premixed swirling combustion," *Proceedings of the Combustion Institute,* vol. 29, pp. 861-867, 2003.

[37] N. A. Chigier and J. M. Beér, "Velocity and static pressure distributions in swirling air jets issuing from annular and divergent nozzles," *Trans. ASME 86D, J. Basic Eng.,* vol. 4, pp. 788-796, 1964.

[38] M. R. Johnson, "Private communication," Carleton University, Ottawa, Canada, 2006.

[39] G. T. Kalghatgi, "Blow-out stability of gaseous jet diffusion flames .1. In still Air," *Combustion Sci. Technol.,* vol. 26, pp. 233-239, 1981.

[40] J. E. Broadwell, W. J. A. Dahm and M. Mungal, *Symp. Int. Combust.,* pp. 303, 1985.

[41] R. K. Cheng, "Velocity and scalar characteristics of premixed turbulent flames stabilized by weak swirl," *Combust. Flame,* vol. 101, pp. 1-14, 1995.

[42] B. Bedat and R. K. Cheng, "Experimental-study of premixed flames in intense isotropic turbulence," *Combust. Flame,* vol. 100, pp. 485-494, 1995.

[43] T. C. A. Hsieh, W. J. A. Dahm and J. F. Driscoll, "Scaling laws for NOx emission performance of burners and furnaces from 30 kW to 12 MW," *Combust. Flame,* vol. 114, pp. 54-80, 1998.

[44] I. G. Shepherd, R. K. Cheng, T. Plessing, C. Kortschik and N. Peters, "Premixed flame front structure in intense turbulence," *Proceedings of the Combustion Institute,* vol. 29, pp. 1833-1840, 2003.

[45] D. Littlejohn and R. K. Cheng, "Fuel effects on a low-swirl injector for lean premixed gas turbines," *Proceedings of the Combustion Institute,* vol. 31, pp. 3155-3162, 2007.

[46] S. Tavoularis, *Measurements in Fluid Mechanics.* Cambridge, New York: Cambridge University Press, 2005.

[47] S. B. Pope, *Turbulent Flows.* Cambridge University Press, New York, 2000,

[48] M. S. Mohamed and J. C. LaRue, "Decay power law in grid-generated turbulence," *J. Fluid Mech.,* vol. 219, pp. 195-214, 1990.

[49] Engineering Sciences Data Unit, "Blockage corrections for bluff bodies in confined flows," *Tech. Rep. Item no. 80024, Institution of Structural Engineers, London,* 1980.

[50] R. D. Mehta and P. Bradshaw, "Design rules for small low speed wind tunnels," *Aeronaut. J.,* vol. 83, pp. 443-449, 1979.

[51] G. K. Batchelor, *The Theory of Homogeneous Turbulence.* Cambridge University Press, England, 1970.

[52] B. Christopher and G. Comte-Bellot, *Turbulence.* CNRS, Paris, 2003,

[53] B. Deschamps, *Etude Spatiale et Temporelle de la Structure Dynamique et Scalaire des Flammes Turbulentes Premelangees de Methane – Air.* Universite d'Orleans, France, 1990.

[54] P. E. Roach, "The generation of nearly isotropic turbulence by means of grids," *International Journal of Heat and Fluid Flow,* vol. 8, pp. 82-92, 1987/6.

[55] R. Liu, D. S. Ting and G. W. Rankin, "On the generation of turbulence with a perforated plate," *Exp. Therm. Fluid Sci.,* vol. 28, pp. 307-316, 2004.

[56] J. F. Meyers, "Laser Velocimetry, Generation of particles and seeding," *NASA, Langley Technical Report Center, Virginia, USA*, 1991.

[57] M. Raffel, C. E. Willert and J. Konpenhans, *Particle Image Velocity: A Practical Guide.* First ed. Springer, 1998.

[58] R. J. Adrian, "Twenty years of particle image velocimetry," *Exp. Fluids,* vol. 39, pp. 159-169, 2005.

[59] Dantec Dynamics, "Particle Image velocimetry measurement principles," available from http://www.dantecdynamics.com, accessed September 12, 2007.

[60] LaVision, *DaVis 7.1 Software Manual.* Goettingen, GmbH, 2006

[61] R. D. Keane and R. J. Adrian, "Optimization of particle image velocimeters .1. double pulsed systems," *Meas. Sci. Technol.,* vol. 1, pp. 1202-1215, 1990.

[62] A. K. Prasad, "Stereoscopic particle image velocimetry," *Exp. Fluids,* vol. 29, pp. 103-116, 2000.

[63] S. A. Filatyev, J. F. Driscoll, C. D. Carter and J. M. Donbar, "Measured properties of turbulent premixed flames for model assessment, including burning velocities, stretch rates, and surface densities," *Combust. Flame,* vol. 141, pp. 1-21, 2005.

[64] E. M. Laws and J. L. Livesey, "Flow through screens," *Annu. Rev. Fluid Mech.,* vol. 10, pp. 247-266, 1978.

[65] J. Westerweel, "Fundamentals of digital particle image velocimetry," *Meas. Sci. Technol.,* vol. 8, pp. 1379-1392, 1997.

[66] A. K. Prasad, "Particle image velocimetry," *Curr. Sci.,* vol. 79, pp. 51-60, 2000.

[67] R. J. Adrian and C. S. Yao, "Pulsed laser technique application to liquid and gaseous flows and the scattering power of seed materials," *Appl. Opt.,* vol. 24, pp. 44-52, 1985.

[68] R. D. Keane and R. J. Adrian, "Optimization of particle image velocimeters .2. multiple pulsed systems," *Meas. Sci. Technol.,* vol. 2, pp. 963-974, 1991.

[69] R. D. Keane and R. J. Adrian, "Theory of cross-correlation analysis of PIV images," *Applied Scientific Research,* vol. 49, pp. 191-215, 1992.

[70] A. Melling, "Tracer particles and seeding for particle image velocimetry," *Meas. Sci. Technol.,* vol. 8, pp. 1406-1416, 1997.

[71] R. J. Adrian, "Particle image techniques for experimental fluid mechanics," *Annual Review of Fluid Mechanics,* vol. 23, pp. 261-304, 1991.

[72] R. J. Adrian, "Dynamic ranges of velocity and spatial resolution of particle image velocimetry," Meas Sci Technol, vol. 8, pp. 1393-1398, 1997.

[73] J. Westerweel, *Digital Particle Image Velocimetry - Theory and Application.* Delft University Press, The Netherlands, 1993.

[74] J. Westerweel, "Efficient detection of spurious vectors in particle image velocimetry data," *Exp. Fluids,* vol. 16, pp. 236-247, 1994.

[75] H. W. Coleman and W. G. Steele, *Experimentation and Uncertainty Analysis for Engineers.* Second ed., John Wiley & Sons, USA & Canada, 1999.

[76] ISO, *Guide to the Expression of Uncertainty of Measurement.* Second ed., International Organization for Standardization, Geneva, Switzerland, 1995.

Appendix A: Selection of screens for the settling chamber

Design principles

- A pressure loss coefficient K that goes from 2 to 2.8, preferably around 2.8 for uniformity [64], is considered to produce good results.
- To avoid a high value in the pressure drop, the screens should be located in an area of low velocity, since ΔP is inversely proportional to the square of the velocity.
- The spacing, M, between wires should be between 1 and 10% of the size of the incoming swirl [46]. The experimental swirls are estimated to be around 3 mm coming from the lead shot spaces in the arrestor. Then, the spacing should be between 0.03 and 0.3 mm.
- For the same ΔP, the use of two screens with finer meshes instead of one, has a better effect in producing uniform flow.
- The screen with higher solidity, σ, should be upstream [64].
- Solidity should be lower than 43% (Porosity, β, higher than 57%) to avoid flow instabilities. If this is not possible for all screens, the last screen must respect this limit.
- The screens should be clean and free of imperfection. Rust must be avoided.

- Regarding spacing, the following is considered:

  The distance between the screens should be such that the turbulence generated by the first screen decays before it reaches the second.

  For the pressure drop to be independent from one screen to the other, the spacing must allow a total static pressure recovery between them.

  The spacing between screens should be 20% of the screen diameter. The same spacing should be kept between the last screen and the nozzle inlet.

Selection of commercially available screens

Screens are generally identified by the pitch (number of wire per inch or mm). The manufacturer also provides the wire diameter and the opening. With this data the porosity, β, is calculated. With the average velocity at the exit of the burner and the ratio of the areas at the inlet and the exit of the nozzles, the average velocity in the settling chamber is obtained. With the fluid mixture density, viscosity, and the diameter of the wire, the Reynolds number, Re, is calculated. The maximum value for K (adding the contribution of all screens) was set to 2.8. The minimum for β was set to 0.57.

Two stainless steel screens have been selected. The first upstream with a mesh pitch # 30 (in inches) and the second downstream (with higher porosity) with a mesh pitch # 20. The final value for K was in the vicinity of 2.8. The position and the spacing respect the 20% diameter rule.

Appendix B: Nozzle contour calculation

According to Tavoularis [46] the profile of a contraction can be developed using two cubics (or other polynomial-type curves), with a joint point where both are matched tangentially. The curves should also match the axial direction at the inlet and outlet sections. The nozzle, (in this example the inner one), must provide a smooth connection between the central cylinder of the burner and the swirler, so as to avoid any major discontinuity or the separation of the fluid boundary layer. Boundary conditions are set at the end of each cubic and at the junction of both. The two equations for the cubics are

$$y_1 = a + bx + cx^2 + dx^3 \qquad \text{B-1}$$

$$y_1 = e + fx + gx^2 + hx^3 \qquad \text{B-2}$$

According to these experiments the following boundary conditions demonstrated to be of good fitting. For R_i as the radius at one end, R_o as the radius at the other end, and L as the total length, there are

At the ends

1. $x = 0 \Rightarrow y_1 = R_i$
2. $x = L \Rightarrow y_2 = R_o$

At the joint point for both curves $R_j = \dfrac{R_i + R_o}{2}$ is considered, then there are the following boundary conditions

3. $y_1 = R_j$

4. $y_2 = R_j$

5. $\left(\frac{dy_1}{dx}\right)_{x=\frac{L}{2}} = \left(\frac{dy_2}{dx}\right)_{x=\frac{L}{2}}$

6. $\left(\frac{d^2y_1}{dx^2}\right)_{x=\frac{L}{2}} = \left(\frac{d^2y_2}{dx^2}\right)_{x=\frac{L}{2}}$

Finally, at the ends again,

7. $\left(\frac{dy_1}{dx}\right)_{x=0} = 0$

8. $\left(\frac{dy_2}{dx}\right)_{x=L} = 0$

The joint point of both cubics is selected at a distance, L_1, on the middle of the length, L. All the conditions above provide the necessary information to form a system of eight equations with eight unknowns, which are the coefficients a, b, c, d, e, f, g, and h. For example, the application of condition 5 implies

$$b + 2cL_1 + 3dL_1^2 - f - 2gL_1 - 3hL_1^2 = 0$$

The values of R_i, R_o, and L are data from our configuration. With the values found for the coefficients of the polynomials, y_1 and y_2 are evaluated at 0.005" intervals. Figure B-1 depicts an inner nozzle external outline. The x-axis on the plot represents the central axis of the nozzle

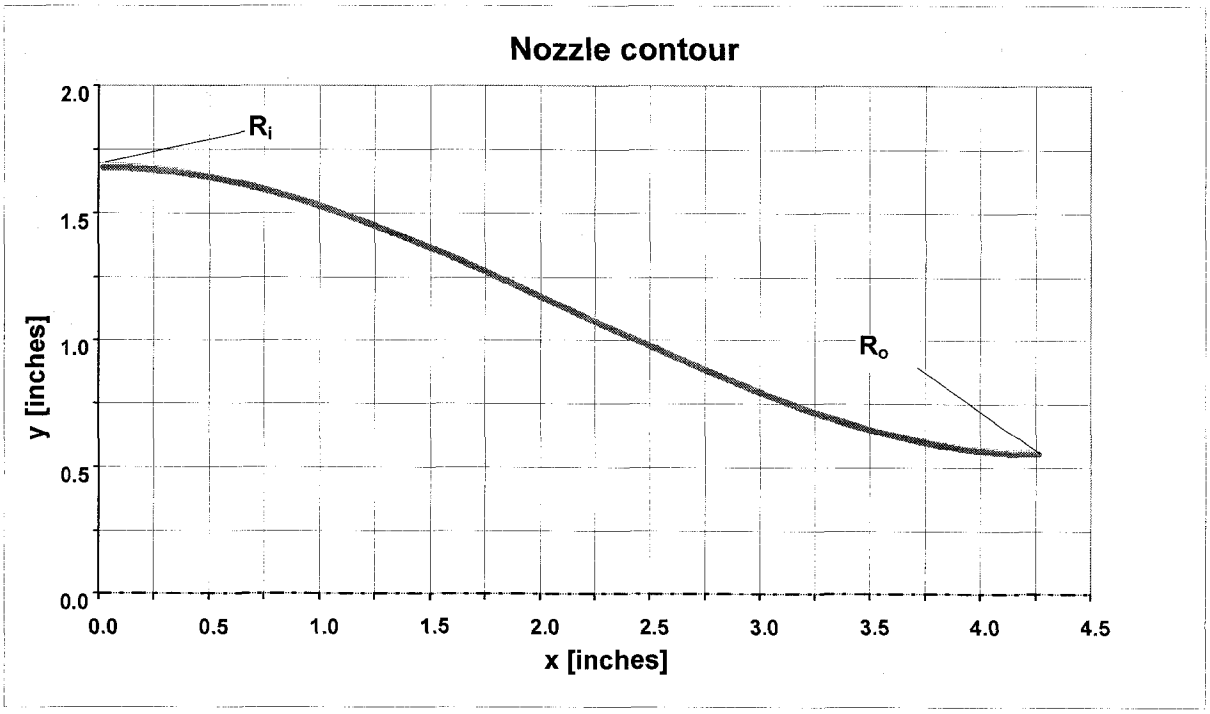

Figure B-1 Inner nozzle contour for the R-6 swirler

Appendix C: Mass flow controllers calibration and setup

Nine MFCs are available for these experiments. Six of them are selected at each time according to the ranges of the tests. The makes and models are

- Six Hasting: rated at 23.1, 100 (2 units), 500, 769 (2 units) and 2311 slpm of methane.
- Three Aalborg: rated at 150 and 250 slpm of methane and 800 slpm of air.

The standard output of the MFC is a 0-5 VDC signal, which is proportional to the flowrate. The following steps are followed:

- The lab is under controlled temperature (20 $\pm$ 2 ° C) and humidity (45 $\pm$ 10%).
- The MFCs are set in horizontal position.
- The pressure line is fitted with filters for water and solid particles.
- The connection lines and pressure regulators are selected in order to minimize changes in the upstream pressure.
- All connections are individually checked for leaks.
- Cables with BNC connectors are manufactured and individually tested.
- The working pressure is set in the range of 30 to 40 psig. This range is well below the limit established by the manufacturer to avoid significant error shifts.

These MFCs work under the principle that heat convected to or from a fluid is proportional to the mass flowrate, $\dot{m}$, of that fluid. They are equipped with a small sensing tube where the flow is proportional to the total mass flow passing through them. Power is applied to two heater coils (upstream and downstream) located around the sensing tube. Wheatstone bridges and control loops keep each heater at a fixed temperature with a $\Delta T = (T_{heater} - T_{ambient})$ above the ambient temperature. The gas temperature before entering the MFC is equal to the ambient temperature. For the Hasting models, the ΔT is set by the manufacturer to 48 °C. It can be shown that the differential power applied to the upstream and downstream heaters is

$$P_u - P_d = 2\dot{m}C_p \cdot (T_{heater} - T_{ambient}) \qquad \text{C-1}$$

where C_p is the specific heat of the working gas at constant pressure. The heat capacity of most of the gases is relatively constant over a wide range of temperatures. Then, by keeping both heaters at the same ΔT above the gas ambient temperature, the power difference is a function only of the mass flowrate. Errors due to changes in ambient gas temperature, as in conventional mass flow sensors, are prevented.

The differential power applied in each condition can be correlated to the mass flowrate for each gas, characterized by its own specific heat, so the MFC can be calibrated directly in mass flowrate units for each gas. By construction, (steel and aluminum blocks on the MFC body) the sensor can capture the actual incoming gas temperature. Nevertheless, it is recommended not to have an abrupt change in incoming gas temperature that can not be sensed immediately by the MFC. This would be the case of a gas coming from a tank at high pressure, where there is a sudden expansion and a

rapid fall in temperature. MFCs are provided with calibration curves for a particular gas, as different gases have different specific heat and densities.

Gas Conversion factors (GCF) are available in tables, and allow to use a MFC calibrated in one gas, with another gas. The reading multiplied by the respective GCF provides the actual flow of the processed gas. The GCF is obtained in different ways including experiments, and through calculation of specific heats. Nitrogen is used generally as the reference gas, so

$$GCF = \frac{C_{p\,N_2}}{C_{p\,Gas\ processed}} \qquad \text{C-2}$$

In this equation, molar specific heat is considered. Values of GCF for the same gas may differ according to various sources. Perhaps the best method to obtain the MFC calibration curve is to pass the gas to be used through the MFC, checking the mass of the gas that went through over discretized time intervals.

In this research, a bottle with the chosen gas is positioned on a high precision scale connected to a PC. The differences in the mass of the bottle and the time steps are registered by means of a code in LabVIEW. Calibration curves (voltage vs. mass flowrate) are obtained in each case and the calibration equation is deduced. The following graph presents an example where the calibration curve and the manufacturer calibration data are compared.

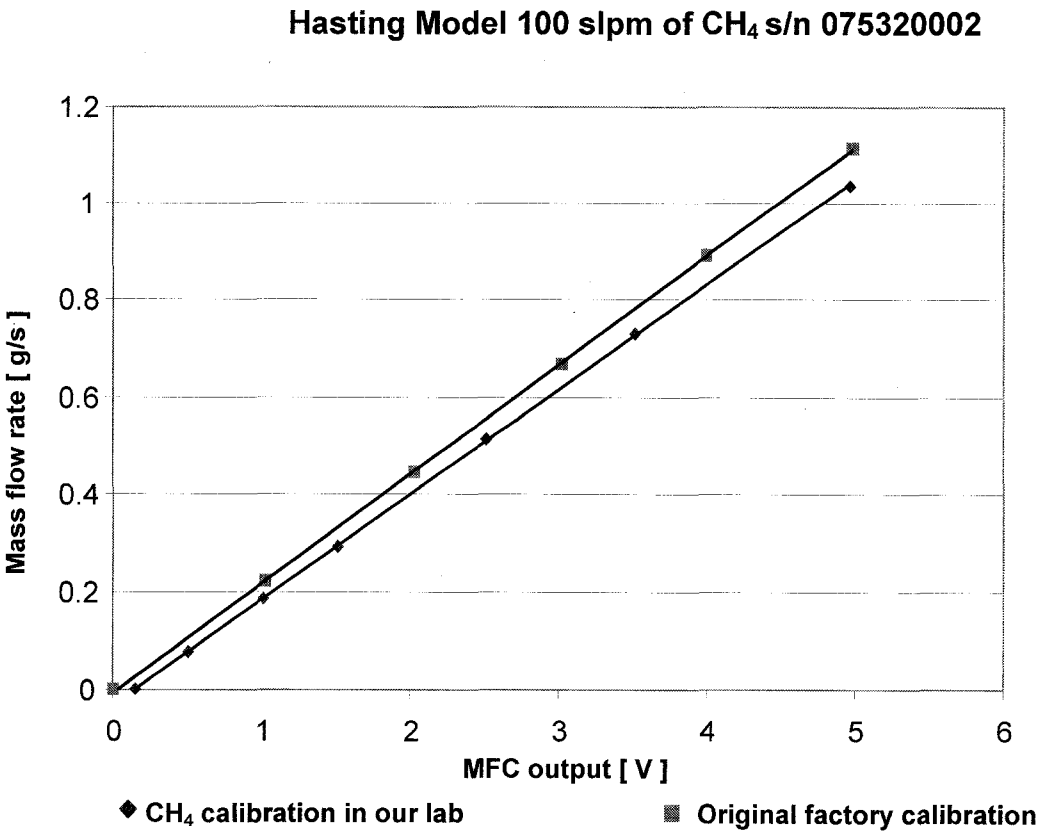

Figure C-1 MFC calibration curves

Appendix D: PIV setup

D.1 General arrangement

A rotational forward–backward scattering 3D (stereoscopic PIV) system has been employed for the determination of the reactant velocity field and the position of the mean flame front contour, as shown in Figure 3-26. In this case, since the two cameras are different models, the most sensitive was located to receive the backward scattered light. This corresponds to the position camera 2. For best results it is ideal for both cameras to receive the maximum amount of light that they are capable of processing before saturation. If not, one of them will be saturated with light and the other would be at low exposure, with poor correlation results.

Particle size

Particles for seeding the flow (known as tracers) must satisfy three conditions to be considered as ideal particles [65]:

- Tracer particles must follow the motion of the fluid.
- They must not alter the fluid flow.
- They must not interact with each other.

Besides this, another fact has to be taken into account [66]: in PIV it is not the flow that is captured optically, but the light scattered by these particles, so it is required that

- Tracers have to be good for light scattering purpose.

For the first set of conditions, the forces exerted on the particle by the fluid motion are considered. A difference in density between the particles and the fluid flow represents the existence of gravitational and inertial drag velocities. For spherical particles, under very low Reynolds number, the gravitational induced velocity U_g, derived according to Stokes drag law is

$$U_g = d_p^2 \frac{(\rho_p - \rho)}{18\mu} g \qquad \text{D-1}$$

where ρ_p and ρ represent the densities of the particle and the fluid, respectively, d_p is the particle diameter; μ is the dynamic viscosity, and g the gravitational acceleration. It can be observed that due to the term d_p^2, the particles should be as small as possible to follow the flow closely. Likewise, the velocity lag, U_s, of the particle in a continuously constant accelerating fluid can be represented by a similar equation where the value g is replaced by the fluid acceleration, a. Thus the lag velocity, U_s, is

$$U_s = U_p - U \qquad \text{D-2}$$

with U as the velocity of the fluid and U_p the particle velocity.

From a different perspective, the step response of the particle velocity, for a particle of much greater density of the fluid is considered [57]:

$$U_p(t) = U\left(1 - e^{\left(-t/\tau_s\right)}\right) \qquad \text{D-3}$$

where the relaxation time, τ_s, is a good measure for the capability of the particle to reach the velocity of the fluid, and is given by

$$\tau_s = d_p^2 \frac{\rho_p}{18\mu} \qquad \text{D-4}$$

Similar conclusions can be obtained from these two equations: the smaller the particle, the shorter will be the time response to match its velocity to the fluid velocity.

Regarding the light scattering condition for tracer particles, it is known that in the Mie's regime ($d_p >> \lambda$) the average intensity of the light scattered increases with $(d_p/\lambda)^2$, while in the Rayleigh scattering regime ($d_p << \lambda$) the scattered light increases with $(d_p/\lambda)^4$ [46, 67]. In these cases λ is the incident light wavelength. Thus for imaging, the larger the particle, the stronger is the scattered light. Hence, in practice there is a trade-off for choosing d_p.

Seeding density

In general, the more particle pairs detected in the interrogation window (IW), the better the correlation value between images. For each IW, only one velocity vector is detected as the average displacement of the whole pattern of particles detected in that IW, for the successive exposures. One way to determine if the amount of particles in the IW is significant, is to verify the following condition for the particle image density, N_I [46, 68]:

$$N_I = C \Delta z_o \frac{D_{IW}^2}{M^2} >> 1 \qquad \text{D-5}$$

where D_{IW} is the IW size, C is the particle density number (particles / volume), Δz_o is the length of a cylindrical volume in the flow containing the particle (the light sheet thickness), and M is the lens magnification factor (ratio of image and object diameter).

It can be demonstrated that the amplitude of the correlation peak is a direct function of this product [65, 69]

$$N_I \cdot F_I \cdot F_o \qquad \text{D-6}$$

where F_I expresses the in-plane loss of particle pairs and F_o expresses the out-of-plane loss of particle pairs. For a value of $N_I \cdot F_I \cdot F_o > 5$ the detection probability is above 95% [10]. As a rule of thumb, according to the manufacturer LaVision [10], it is necessary a minimum of 3 or 4 particles pairs per IW. However, for strong correlations, 10 pairs are recommended. The limit to high density is provided by the lack of contrast between particles. The appearance of particles that overlap, when actually are only close to each other, is due to diffraction, where a random interference pattern (known as speckle) is observed. Normally, the image of two or more particles overlaps if their distances on the image plane are less than d_e, which is the particle image diameter on the recording plane. The value of d_e is a function of the size of the particle d_p, the effect of light diffraction on the lens, and the magnification, M, [46]. To avoid overlapping, the particle source density, N_S, should be

$$N_S = C\Delta z_o \frac{\pi d_e^2}{4M^2} << 1 \qquad \text{D-7}$$

As stated by Westerweel [65], it must be noted that increasing seeding density enhances the detectability of the displacement-correlation peak; however, it does not improve the estimation precision, which is determined by the value d_e/D_{IW}.

In general, seeding should be homogeneous along the field of view to have meaningful results. In these experiments, the software control panel allows the variation

of the seeding independently, in the inner and outer flow, to balance both sections. Good seeding can be verified during setup by checking the correlation peak detected.

Resolution and errors – Peak locking

In digital cameras, the word resolution refers to the size d_x of one pixel [46]. According to Westerweel [65], for d_e/d_x <<1 the error in measurement is mainly a bias error, such as peak locking. This is perceived as an error in the final value of the velocity vectors toward integer values. This happens when the particle images are too small, e.g. less than one pixel. A probability density function (PDF) curve can be used to check whether or not the velocity field presents this effect. For values of d_e/d_x >>1 the random errors (which increase with particle image diameter) dominate. The final estimation error has a minimum at $d_e/d_x \sim 2$, and the typical relative measurement error is 1% for a displacement of 1/4 of the IW.

Interrogation window size

Experience shows that good values of the relationship D_{IW}/d_e are in the range of 20 to 30 [46]. Then, for $d_e = 2$ pixels, a good IW size is between 32 and 64 pixels per side. The IW size provides the "spatial" resolution (number of velocity vectors per unit of length) in the flowfield. As mentioned in Chapter 3 the displacement, $\overline{\Delta X}$ of the particle should be close to 25% of the IW, between exposures.

Selection of seeding particles

For these experiments, olive oil is used. Previously, it has been widely used with good results. The classical method with Laskin nozzles immersed in the seeding fluid is used.

As mentioned in Chapter 3, dampers (sometime called impactors) guarantee that only small particles of 1 to 5 μm are allowed. This size, along with the selection of the field of view (FOV), related to the magnification M, satisfies the requirements $d_e = 2$ pixels. In this study, it is required to determine the velocity field and the position of the flame front, since this is directly related to stability. Hence, as the olive oil particles are consumed rapidly (olive oil boils at 299 ° C) as they approach the flame, the position without seeding is defined as where the flame starts.

Melling [70] provides comprehensive data about seeding, including the ability of olive oil particles to follow the change in the flow. This is useful for turbulence measurements. For this type of oil, the frequency response for particles of 1 μm is 10 kHz and for particles of 3 μm is 1 kHz.

Figures D-1, D-2 and D-3 show images of tracer particles and flow seeding with and without the presence of flame.

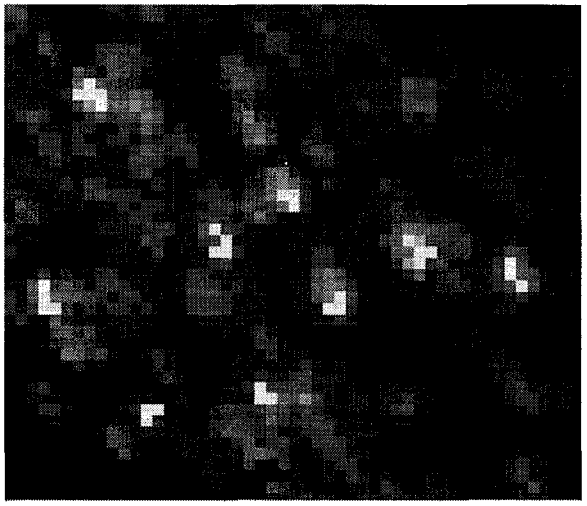

Figure D-1 Images of tracers

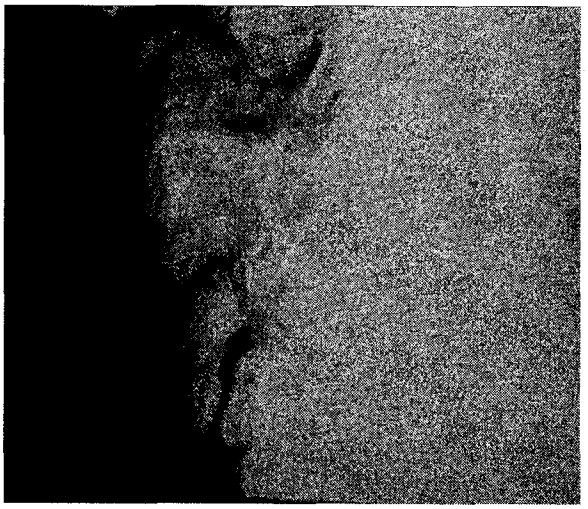

Figure D-2 Seeded flow without the presence of flame

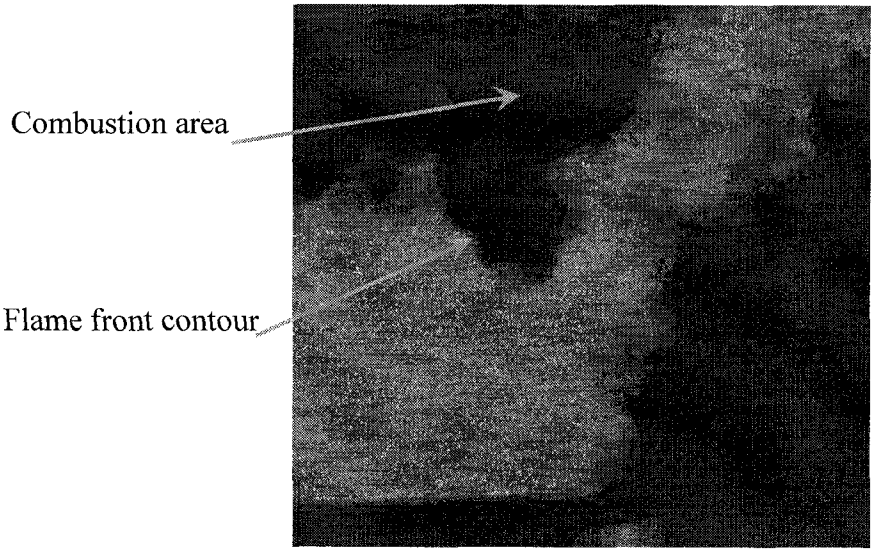

Figure D-3 Seeded flow in the presence of flame

Particles disappear once they make contact with the flame front

D.2 Calibration

In the PIV system, the image is affected by factors such as lens magnification, distortion and perspective view. To determine the actual distance between points in the object plane, it is necessary to calibrate the system to compensate for those factors. The process that compensates only for the magnification effect is called scaling. The process that

corrects for the other two factors is known as image dewarping or correction; hence, an image dewarping function is required to map the camera images to a "world" coordinate system, free of distortion.

In the particular case where the camera viewing direction is perpendicular to the object plane and there is no distortion, just a scaling factor between length (e.g. in mm) in the object plane and pixels on the camera is required. In the case of stereoscopic PIV, the 3D velocity vectors are obtained from their projections in 2D provided by each of the cameras. Then, it is mandatory to establish the viewing directions of both cameras with respect to the light sheet position, which will be incorporated in the calculations. In summary, the image scale [pixel/mm] obtained by this process, allows the results to be scaled into units (e.g. velocity in m/s) that correspond to true dimensions (world dimensions).

Stereoscopic Calibration

In this context, the same place (same field of view) is looked at, but from a different angle with each camera. Since the velocity vectors are reconstructed at each point from both images, it is required to have the same coordinate references on both cameras. This means that the image points for the origin ($z = 0$) will be in the same pixel location in the dewarped images of both cameras. This is accomplished by having one dewarping function for each camera and by mapping each function onto each other, to have a common coordinate system with the same scaling. The standard for calibration is a 3D plate with equally spaced dots used as references. The geometry and dimension of the

plate are incorporated as data into the calculations. In this case, the calibration plate is set on the middle plane right above the exit of the burner.

The field of view (FOV)

The size of the FOV for each camera increases, as the camera moves away from the object. The further from the object plane, the larger the FOV and the lower the resolution, since for the same size pixel a larger image is captured. So both the FOV and the pixel size are related to the resolution, which is observed in Figure D-4. The upper pair shows that going to a larger pixel size would make impossible to detect the movement of the particle, because it would take place inside one pixel. In the lower pair of sketches, for the same pixel size the camera draws back to be able to capture a larger image, but it loses resolution, since the movement is now limited to one pixel.

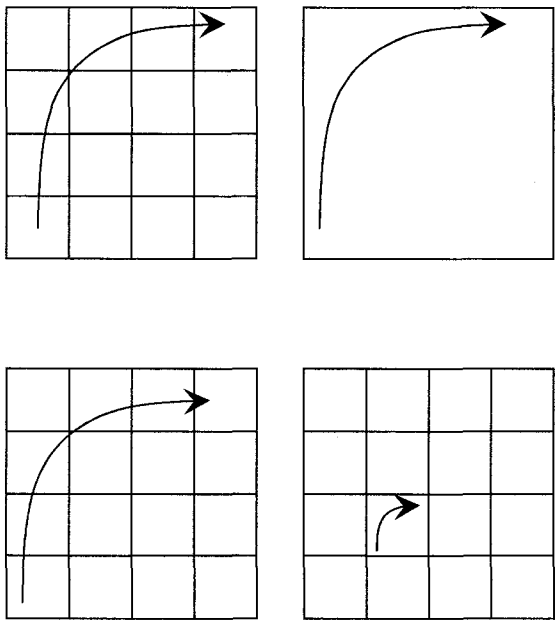

Figure D-4 Effect of pixel size and field of view on the resolution

In the case that the particle image size, d_e, generated is far from the 2 pixels recommended, the option is to modify the FOV. For these experiments a final FOV of 85 mm is chosen. Under this limitation, half of the total image of the flow is taken, from the central axis of the burner. This is considered acceptable due to the symmetric features of the burner.

System setup

In 3D, two types of systems are distinguished according to the orientation of the camera axis: the translation system, which has both cameras' axes parallel to each other; and the rotational system, where both axes are rotated so they intersect the object plane at the same system axis. The last system, as in this case, has the advantage of a higher degree of accuracy compared to translational systems [62]. This is due to the fact that the angle, θ, between the camera axis and the perpendicular to the object plane, can be increased further without major drawbacks in lens performance. This is also useful to determine the out-of-plane components. However, the magnification is no longer uniform over the FOV, and particles are not generally in focus in a FOV with a short depth of field.

To compensate for this, the Scheimpflug criterion is applied. For this, the image plane is rotated by an angle α, so that the three planes (object, lens, and image plane) intersect in a common line. An adaptor is mounted between the lens of each camera and the CCD plane to meet the criteria.

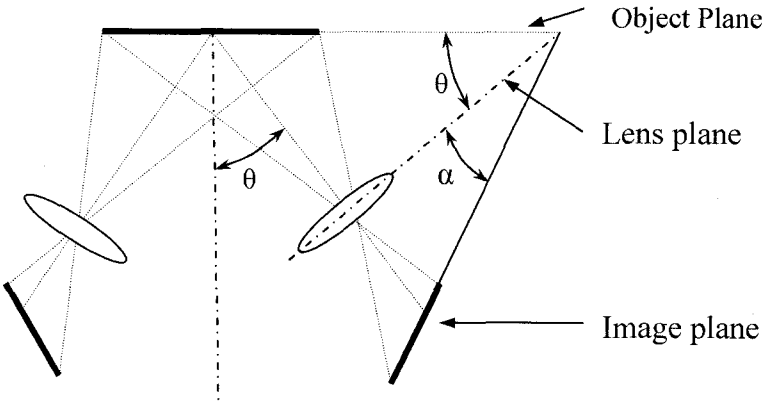

Figure D-5 Rotational PIV system with Scheimpflug criterion

For maximum overlap it is recommended that the vertical edges of both images match. However, it is demonstrated that the Scheimpflug criteria increases the problem of magnification. In the case this problem is significant, and to avoid using the Scheimpflug criterion, an increment of the depth of field can be considered so the particles are in focus. Adrian [71] provides the thickness of the depth of field with a formula by P. W. Offutt:

$$\delta(z) = 4\left(1 + M_n^{-1}\right)^2 f^{\#2}\,\lambda \qquad \text{D-8}$$

where M_n is the camera magnification, λ is the wavelength of the laser, and $f\#$ is the f number of the lens. A larger $f\#$ produces a larger depth of field, with less out of focus particles, but due to less scattered light captured, a lower amount of particles is acquired.

The forward - backward scattering light arrangement (both cameras on the same side of the plate) is, in general, easier to calibrate compared to the backward - backward scattering system (one camera on each side of the plate). However, given that one camera receives more light (forward scattering) than the other; the $f\#$ of each camera may be different. If different cameras are used, the less sensitive one is to be located in the forward scattering position.

While setting up the calibration plate the following is considered:

- Both images must be in focus.
- The overlapping area between both cameras has to be maximized.
- The cameras should be symmetrically located with respect to the object plane. To balance for errors in both directions, in-plane (XY) and out-of-plane (Z), θ should tend toward 45° [62]. However, as a large angle can create magnification problems, in this research an angle $\theta = 28°$ is used.
- The light sheet must be parallel to the calibration plate.
- The calibration plate should cover all the FOV.
- Given that the spatial calibration maps the calibration of camera 2 onto the calibration of camera 1, the reference marks (dots) should be almost at the same pixel position in the images from camera 1 and camera 2. So during calibration the central dots match in both images. This is not the case for the rest of the marks, since the images are distorted in different direction with respect to each other (one increases as the other decreases as they approach the edges).

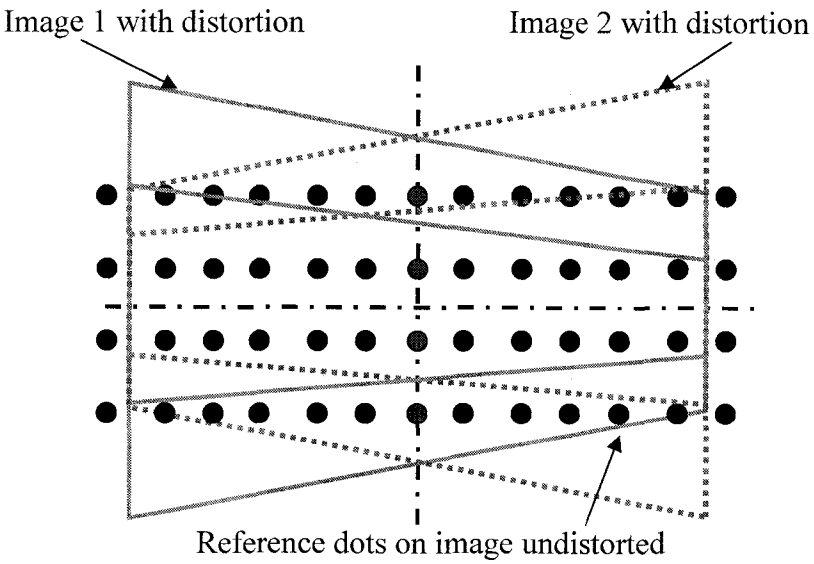

Figure D-6 Imaging from both cameras during calibration

In this system (LaVision) the steps followed are

1. Definition of the experimental setup

   This case corresponds to 3D stereoscopic PIV.

2. Definition of the coordinate system (right or left handed) and number of views

   There is the option to take many views of the calibration reference plate to increase accuracy. According to the mapping dewarping model, called pinhole or polynomial, the minimum number of required views are one and two, respectively.

3. Selection of the calibration plate

   This setup includes a Type 20 LaVision 3D calibration plate. A 2D plate should be avoided, since it is prone to errors because it requires displacement during 3D calibration.

4. Image acquisition

   All the calibration plate images for all cameras and all views are taken.

5. Marks definition

Three marks for the initiation of the mark search are chosen. They must be the same for all cameras and all views and located on the front plane of the calibration plate.

6. Marks search

The program searches for the rest of the marks. Generally it is enough if 20-30 marks could be found. However, in these experiments around 45 marks are captured for each camera, as shown in Figure D-7.

7. Mapping functions fit

In this step the dewarping mapping function is fitted to the set of marks previously identified. A pin-hole or polynomial calibration functions is chosen. The average deviation of the dewarped marks positions is obtained. A value lower than 1 pixel is acceptable, a value lower than 0.3 pixels is excellent. Values higher than 2 pixels should be rejected. In this study, all the measurements included values from 0.3 to 0.5 pixels. It is recommended to use the pinhole calibration, since by doing this the program can use the self calibration function. This utility adjusts the coordinate system and the camera calibration so that the plane $z = 0$ mm is exactly in the middle of the light sheet. This is independent of the fact that both planes of the plate must be in the light sheet.

8. Validation

In the final step all images are dewarped. By inspection, the result of the calibration is verified; e.g. the summed up images the marks must coincide.

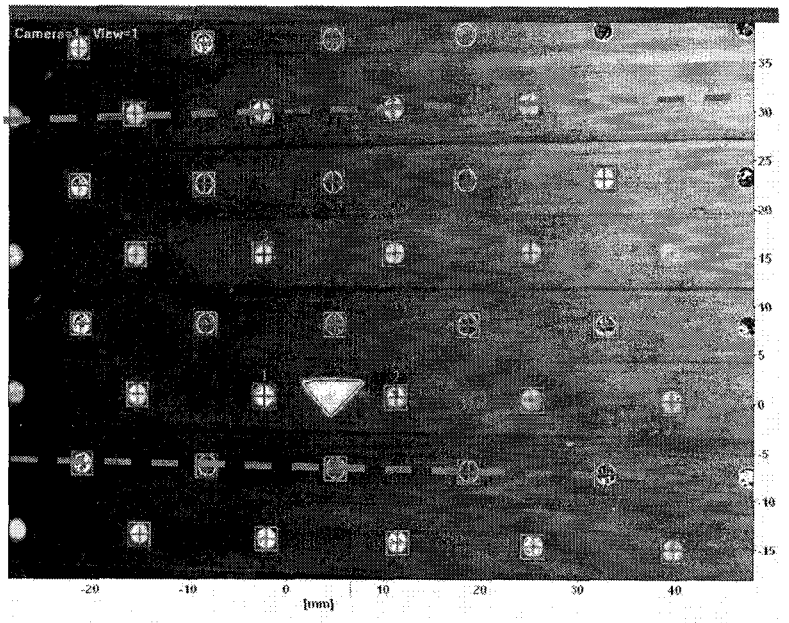

Figure D-7 Marks found on a calibration plate image

Considerations regarding the orientation of the reference plate

- Both planes of the plate are contained in the light sheet.
- The light sheet passes through the center of the burner.
- The light sheet is parallel to the plate.

The first condition is checked by inspection during calibration. After this, the plate is rotated 90° to verify that the light sheet impact the center of the plate, correcting accordingly through iteration. The lack of parallelism of the light sheet with respect to the plate can be detected by the light diffraction on a wall behind the plate. When the condition is corrected, there is practically one light image on the wall.

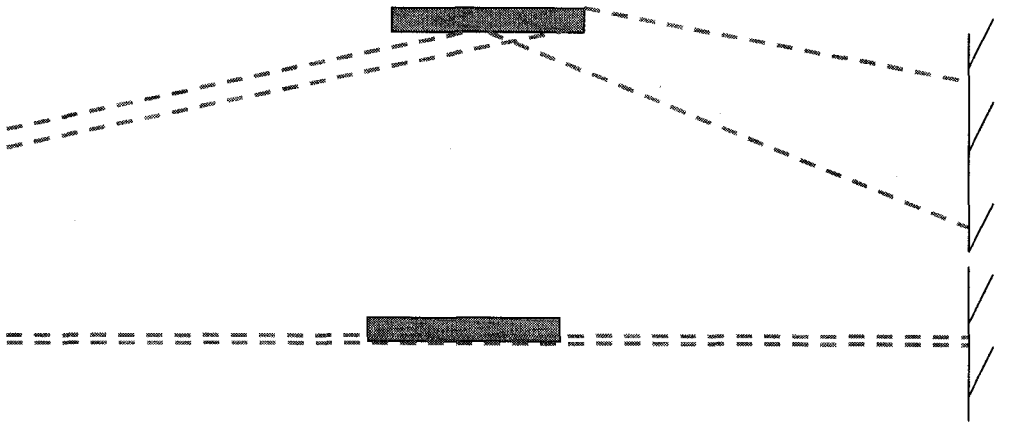

Figure D-8 Sheet light orientation during calibration

Final calibration adjustment (self calibration)

Since the position of the plate has an intrinsic error (the light sheet is never perfectly parallel and is not exactly overlapped with the plane z = 0 of the calibration plate), the software can correct this. The particle in the light sheet is originally considered at the position z = 0. However, due to the discrepancies, each camera detects a different position as shown in the Figure D-9 recreated from [10]. The distance between both is represented by a vector called "disparity vector". Through a recursive procedure with the LaVision software, it is possible to compensate for the differences.

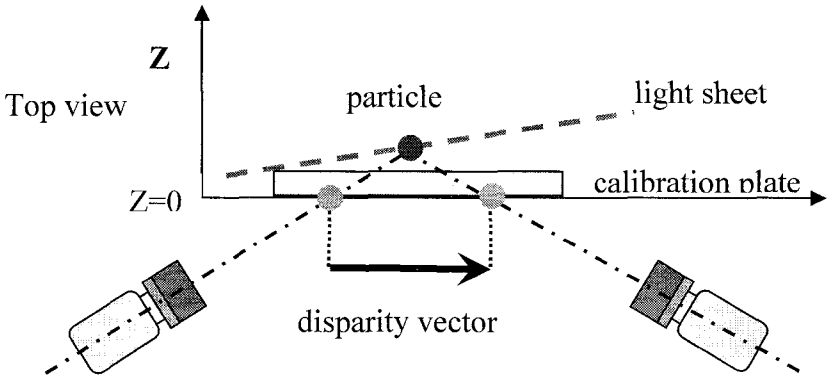

Figure D-9 Correction for light sheet misalignment, from [10]

D.3 Experiment setup

Physical alignment of the laser beams

The laser lamps are mounted one next to each other, inside the laser casing. The beams pass through a series of special crystals and mirrors until they leave the laser enclosure. Both beams must be collimated in such a way that they are overlapped, that is, the light sheet projected is exactly in the same spatial position for both pulses. If this is not the case, then, the images would correspond to different zones of the flow field. To verify this alignment, a set of two pictures with the minimum possible lag time between them are taken, which for this system is less than 0.5 μs. The images should be almost equal. If not, the mirrors must be aligned inside the laser casing.

Synchronization of the laser pulse with the camera

It is possible that the lasers flashes are not illuminating the correct frame e.g. both pulses are on the second frame. This can be corrected by switching off the second laser and changing the initial trigger delay until only the first frame is exposed by laser 1. With the second laser on, only the second frame should be exposed. The iterative procedure is repeated until laser 1 is only in the first frame and laser 2 in the second frame.

Determination of the delay "*dt*" between both exposures

This is of utmost importance, particularly in stereoscopic PIV given that the movement of the particle needs to be captured also on the plane perpendicular to the light sheet. It is common to call the vector components in-plane for the velocity components on the XY

plane (aligned with the light sheet) and out-of-plane for the Z component, (perpendicular to the light sheet). The *dt* selection is directly related with the light sheet thickness.

2D components

Since the approach to obtain the best *dt* is iterative, a general knowledge of the velocity field is an important step to reduce the length of this process. By knowing the approximate value of the velocity field, (i.e. through the flowrate and the area at the exit of the burner), an initial value of velocity is considered as a datum. The image scale of the system can be calculated as the ratio of the field of view size to the number of pixels per side on the CCD. This value is also determined by the software of the calibration system. For this example

$$\text{Image scale} = \frac{85}{1600} = 0.053125 \frac{\text{mm}}{\text{pixels}}$$

As was mentioned, the IW size provides good results in the order of 32 to 64 pixels per side. With the vane sector for the swirler R8 equal to 5 mm wide, the spatial resolution, *R*, for an IW of 32 pixels is determined. The value of *R* can be obtained as the product of the interrogation window size, D_{IW}, in pixels; and the image scale. Hence *R* is

$$R = 32 \cdot 0.053125 = 1.7 \text{ mm}$$

Then, there will be one vector per IW, which is every 1.7 mm, that is, almost three vectors along the vanes zone. The particle should move 25% of the IW, which represents in true world coordinates

$$\overline{\Delta X} = \frac{1.7}{4} = 0.425 \text{ mm}$$

and the delay dt for this displacement corresponds to the general form, $dt = \overline{\Delta X}/\overline{V}$. For an estimated U velocity component of 3 m/s, the value of dt is

$$dt = \frac{0.425 x 10^{-3}}{3} = 0.000141\ s = 141\ \mu s$$

For these tests a spreadsheet from [38], that contains all data including optics features, is used to determine the initial value of dt. With this dt, the first set of images are taken and analyzed for the strength of the correlation peaks. A strong peak indicates good time selection (along with other parameters, e.g. illumination, seeding, etc.). Two to three sets of measurement define the final dt.

3D components

In this case it is critical that the amount of particles lost in the Z direction, is lower than 30% [57, 72]

$$\frac{W\,dt}{\Delta z_o} \leq 0.3 \qquad \text{D-9}$$

This approximates the appropriate thickness of the light sheet, Δz_o. With the value of the average exit velocity, and the vane geometry, an initial value for W is estimated. This, along with dt from the 2D case, provides an initial value close to 1 mm for Δz_o.

Another limitation is that the light sheet thickness must contain both planes of the calibration plate, in our case they are apart 1.5 mm. So the initial Δz_o is set to 2mm. The first set of velocity values calculated through PIV is used as an input to determine a new value for the light sheet thickness. If the light thickness happened to be small (too many particles lost in Z), the possibilities are to either increase Δz_o or reduce dt. The last

possibility should be avoided, because it will yield less stable results. Therefore Δz_o is set to 3 mm in order to obtain good results. It should be said that a light sheet too thick reduces the maximum light intensity available, given that the same laser energy is spread over a wider area.

D.4 Results

The first objective with 3D PIV in this research was to determine the 3D velocity field. The next was to scrutinize the stabilization mechanism and to calculate the swirl number, *S*, through numerical integration. Finally, the remaining objective was to obtain the mean flame front contour.

Mean flame front contour

The flow and the flame are considered statistically stationary over a certain period of time for one set of fixed parameters. Sets from 600 to 1000 images are taken to define one condition of the flow (with or without flame). The FOV of 85 mm allows the capture of one half of the flame. The steps to detect the mean flame position are

1. Frame extraction

   From the1000 sets of 4 images each (two images for each camera for double frame double exposure), one image of each of all sets (e.g. image 1 of 4) is extracted.

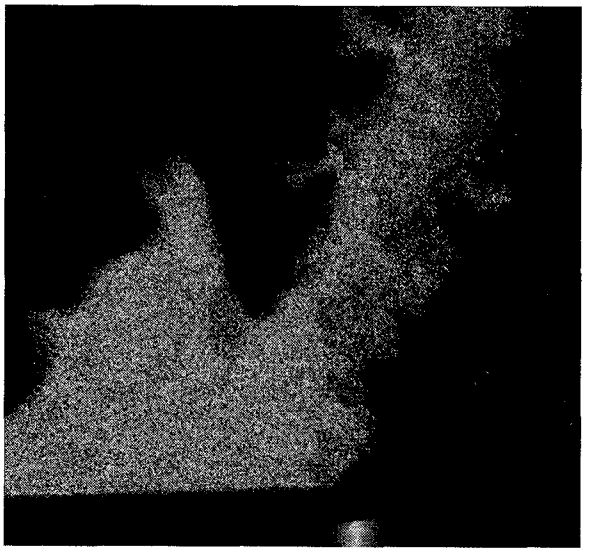

Figure D-10 Raw image

2. Image correction

   The image captured by the camera is distorted. A raw image is transformed to a true image with world coordinates.

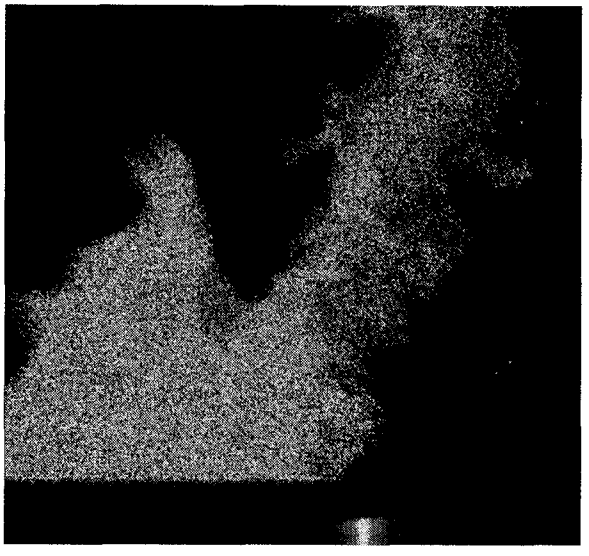

Figure D-11 Corrected image

3. Linear filtering (e.g., 9x9 smoothing)

   This filter eliminates high frequency noise. Mathematically is a matrix that calculates the new value of the pixel intensity as a linear combination of the intensities values of

the pixels in the surrounding area, including the value of the central pixel itself. For the simplest case (3x3) the filter matrix is

$$A = \frac{\begin{bmatrix} a1 & a2 & a3 \\ b1 & b2 & b3 \\ c1 & c2 & c3 \end{bmatrix}}{divisor} \qquad \text{D-10}$$

This matrix, multiplied by the matrix of the intensities of the pixel itself and the 8 surrounding pixels, provides the final matrix from which the terms for the linear combination are obtained. The new pixel filtered intensity is

$$I_{ij}^{*} = \frac{\begin{bmatrix} a1\,I_{i-1,j-1} & a2\,I_{i,j-1} & a3\,I_{i+1,j-1} \\ b1\,I_{i-1,j} & b2\,I_{i,j} & b3\,I_{i+1,j} \\ c1\,I_{i-1,j+1} & c2\,I_{i,j+1} & c3\,I_{i+1,j+1} \end{bmatrix}}{divisor} \qquad \text{D-11}$$

Equation D-11 can be rewritten as

$$I_{ij}^{*} = \left[a1\,I_{i-1,j-1} + a2\,I_{i,j-1} + a3\,I_{i+1,j-1} + b1\,I_{i-1,j} + ... + c3\,I_{i+1,j+1}\right] / divisor \qquad \text{D-12}$$

When the divisor is the sum of all the filter matrix elements a1, a2 .....c3, the average image intensity stays the same. When a smoothing effect is needed, all the coefficients are set to 1 and the divisor, 9. The position of the flame is considered to be the boundary line between seeded flow with no flame, and flow with no seeding; because the oil is consumed by the flame. The difference between both areas is still not rigidly defined. There are some areas (small pockets) on the no flame zone where there is no seeding but there is no flame. The smoothing filter has a positive effect on

making the no flame area homogeneous; hence, a threshold of image intensity is defined in the next steps.

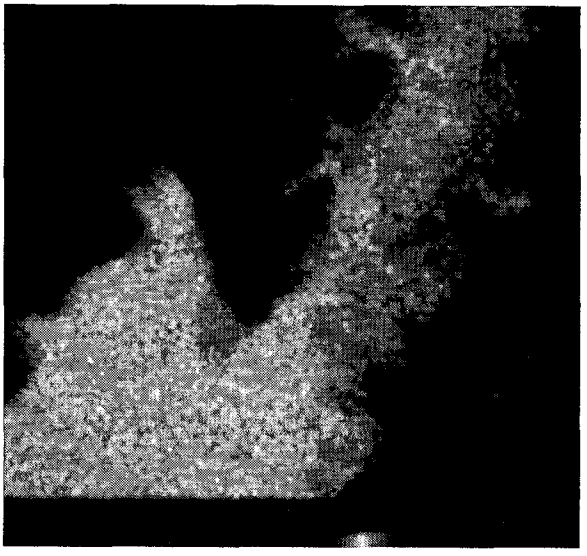

Figure D-12 Image after filtering

4. Binarization

In order to set a threshold on the reactant area, a "jump" in image intensity (above 100 counts) from the no seeding to seeding presence is detected by inspection. Then, the image is "binarized" imposing a value of 1 where the image intensity is above 100 counts and a value of 0 below that intensity.

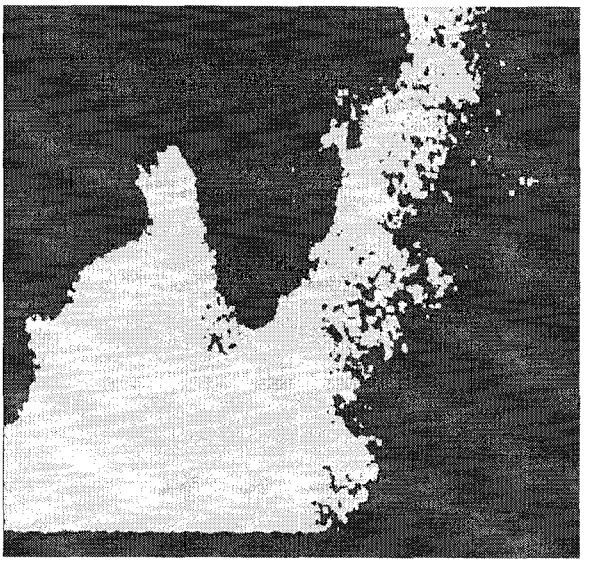

Figure D-13 Image after first binarization

5. Averaging

The average of 1000 images is calculated, which is combined into one image. Since the flame images are different from one another, the final result is comprised of areas with intensities going from 0 up to 1. For example if at a certain location there is no flame 375 times (and there is seeding) , then 375 out of 1000 times there are values of intensity equal to 1. Then, the final value of intensity for that location is 375/1000 = 0.375.

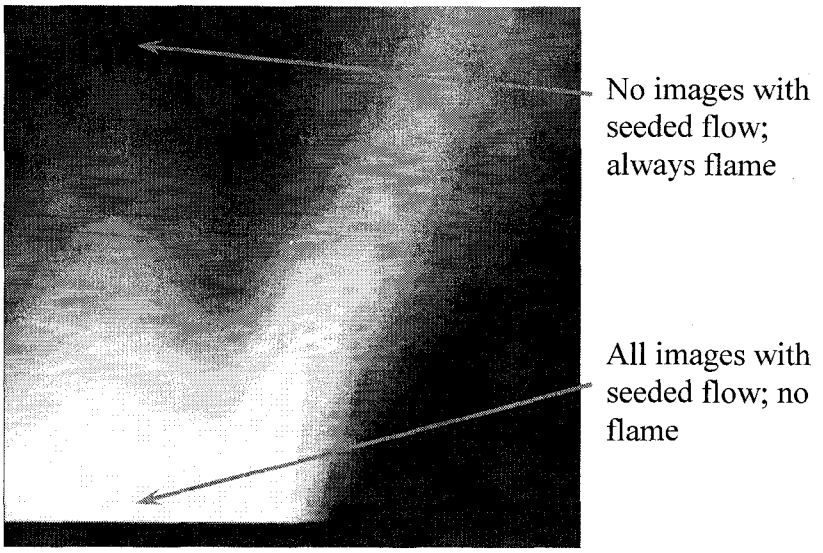

Figure D-14 Images averaging

6. Second binarization

The position of the mean flame front contour is considered the one that correspond to the median. That is, out of 1000 images, it is the position of the image 500. This is done using the intensities, given that at a location where there are 1000 images of seeded flow, the intensity is 1 and no image implies intensity 0. If each image corresponds to a thousandth of the maximum intensity, the intensity of 0.5 is the location for the overlap of 500 images. Hence, a threshold of 0.5 for the binarization is defined; a value of 0 for intensities below 0.5, and 1 for intensities above, are imposed. The image has two distinctive zones: 0 for the region with flame and 1 without flame. The border is the mean flame front contour.

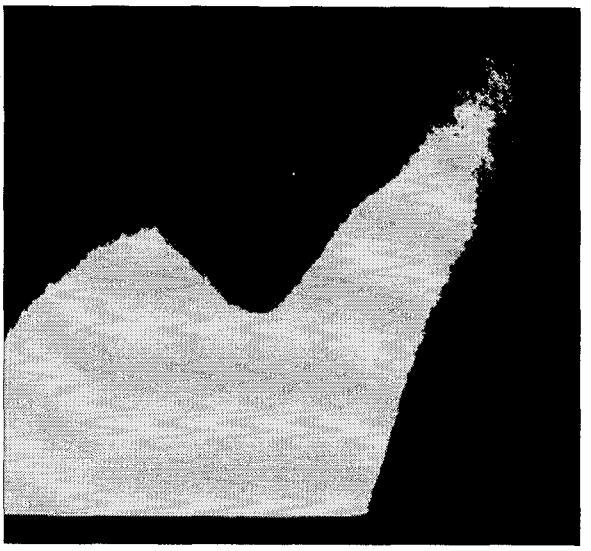

Figure D-15 Image after second binarization

7. Laplace edge detection

This filter improves the definition of the flame position. Here the intensities of the surrounding pixels are subtracted from the central pixel. For a homogenous area, the result is zero. However, where a discontinuity in intensity is detected, the Laplacian filter provides a non-zero value. The final result is the edge between the flame and no flame zones. An example of this filer is described in Equation D-13.

$$Laplace\ Filter = \frac{\begin{bmatrix} -1 & -1 & -1 \\ -1 & +8 & -1 \\ -1 & -1 & -1 \end{bmatrix}}{divisor} \qquad \text{D-13}$$

The software assigns a value of 1 to the divisor for this type of filter

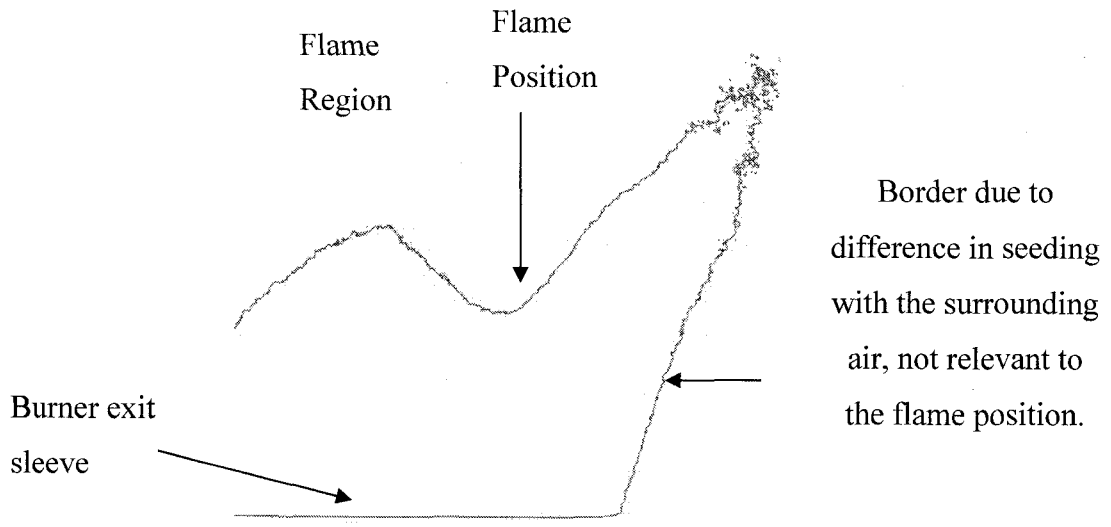

Figure D-16 Final flame position

Velocity field calculation

Overlap

The IW size is defined by the user and it defines the spatial resolution of the velocity field (one vector per IW). The image is divided accordingly e.g. a display of 1024 x 1024 pixels with an IW of 64 x 64 has 1024/64 =16 IWs per side. An overlap of 50% allows to obtain an extra vector between both IWs, increasing the resolution. For the example previously shown, the final spatial resolution is 0.85 mm.

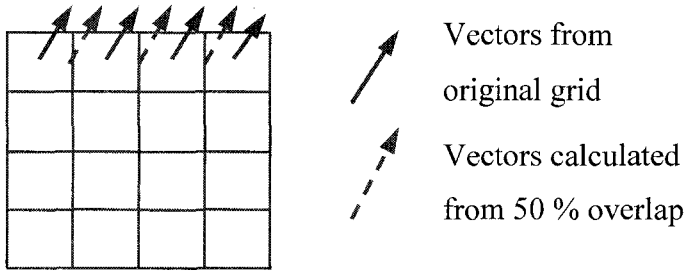

Figure D-17 Vector calculation with 50% overlap

Iterations

In the multipass case, the information from the first pass is used to shift the IW in the new pass, to capture more particle pairs. This improves the correlation and the signal-noise ratio. A final refinement is the multipass with decreasing IW size. While the window shift is improved from one pass to the other, the final computation is done over a smaller IW, but with similar amount of particles due to optimization in the shifting. In this study, a double pass with 50% overlap, initial IW size of 64 x 64 and final IW size of 32 x 32 is selected.

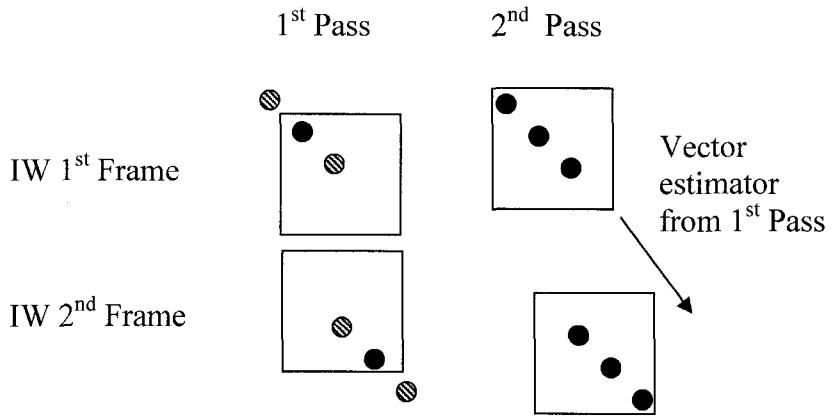

Figure D-18 Multipass iteration to increase accuracy

Vector Post-processing

It is critical in PIV to filter "spurious vectors" that do not represent the velocity field; e.g. one vector in opposite direction or several times higher in magnitude than is supposed to be. Different options are available:

1. Vector range

   A range is specified beyond which no vectors are considered valid.

2. Peak ratio condition

$$Q = \frac{P1 - min}{P2 - min} > 1 \qquad \text{D-14}$$

where *min* is the lowest value on the correlation plane and *P1* and *P2* are the first and second highest correlation peaks. Q values close to unity indicate a probably false vector. A value of Q higher than 2 could remove good vectors [73, 74]. It is a good practice to check the value of the correlation map during the initial measurements, to confirm that the parameters chosen, such as the delay *dt* between light pulses, produce accurate results.

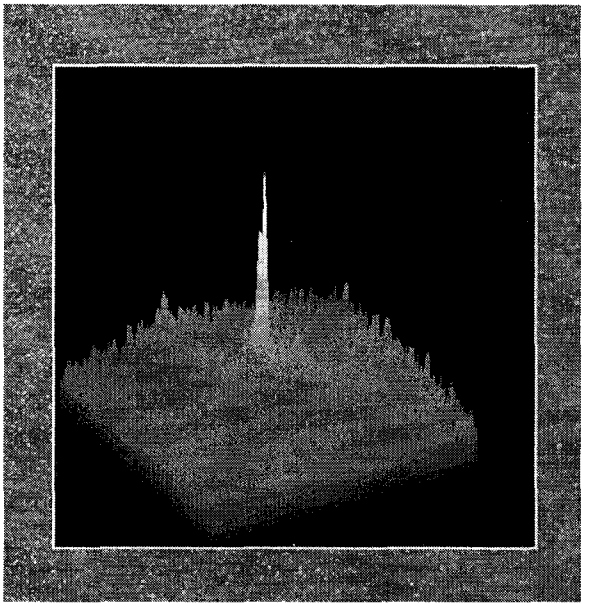

Figure D-19 Correlation map at one point of the flowfield

3. The median filter

A median vector (average of the two central elements) is computed from the 8 neighboring vectors and is compared with the central vector velocity, $\overline{V}$. The vector $\overline{V}$ must satisfy the following condition to be accepted:

$$\left(\overline{V}_{median} - \overline{V}_{rms}\right) \leq \overline{V} \leq \left(\overline{V}_{median} + \overline{V}_{rms}\right) \qquad \text{D-15}$$

where $\overline{V}_{rms}$ is

$$\overline{V}_{rms} = \sqrt{\frac{1}{N-1}\sum_{i=1}^{N}\left(\overline{V}_i - \overline{V}_{median}\right)^2} \qquad \text{D-16}$$

The advantage of the $\overline{V}_{median}$ is to avoid an average distorted by big outliers.

Final processing

From each group of 1000 sets of images, one final velocity field is obtained. When the final average is computed, extra filtering is applied; e.g. accepting those vectors inside an interval of certain dispersion characterized by the rms.

Appendix E: Uncertainty of measurements

Uncertainty of measurements can be defined as the interval within which the true value of a measurable property lies with a certain probability [46]. In this study, for the planning stage, the propagation of the uncertainty of measurement was evaluated according to the following equation [75, 76]:

$$U_r^2 = \left(\frac{\partial r}{\partial X_1}\right)^2 Ux_1^2 + \left(\frac{\partial r}{\partial X_2}\right)^2 Ux_2^2 \ldots + \left(\frac{\partial r}{\partial X_j}\right)^2 Ux_n^2 \qquad \text{E-1}$$

where the result, r, of the experiments, is a function of n measured variables, X_i, such as

$$r = f(X_1, X_2, \ldots, X_n) \qquad \text{E-2}$$

For stability limit points (blowoff, flashback and in burner conditions) a series of repeatability tests were conducted and the random component of uncertainty, P_i, was determined. This was combined with the bias contribution, B_i, to obtain the total uncertainty value for a confidence level of 95% [75]:

$$U_{95} = \sqrt{B_i^2 + P_i^2} \quad \text{for } N \geq 10 \qquad \text{E-3}$$

where N is the number of measurements. For the equivalence ratio, Φ, sets of 40 measurements were taken for each of the limit points at fixed experimental conditions. The values of Φ were processed statistically to calculate the random component of the

uncertainty. For all three conditions, a final combined uncertainty of $U_{95} = \pm 3\%$ was determined.

For PIV measurements, the average was evaluated to define the minimum amount of images required to calculate certain parameters, namely, the mean axial velocity component, U, and the turbulent velocity component u'. Figures E-1 and E-2 show the average of the variables U and u' respectively, at certain (x,r) coordinate on the flowfield, as a function of the number of images, n. The coordinate system origin $(x,r) = (0,0)$ is at the center of the burner exit plane.

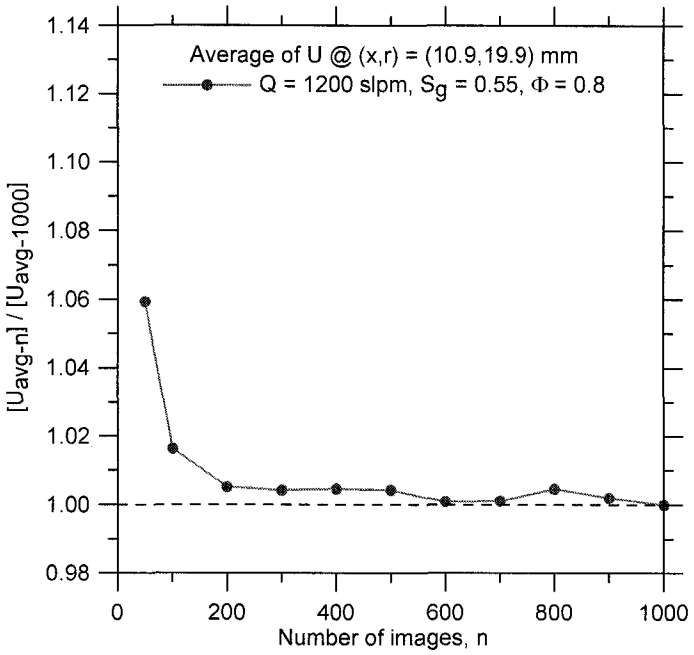

Figure E-1 Normalized average of the axial velocity component, U

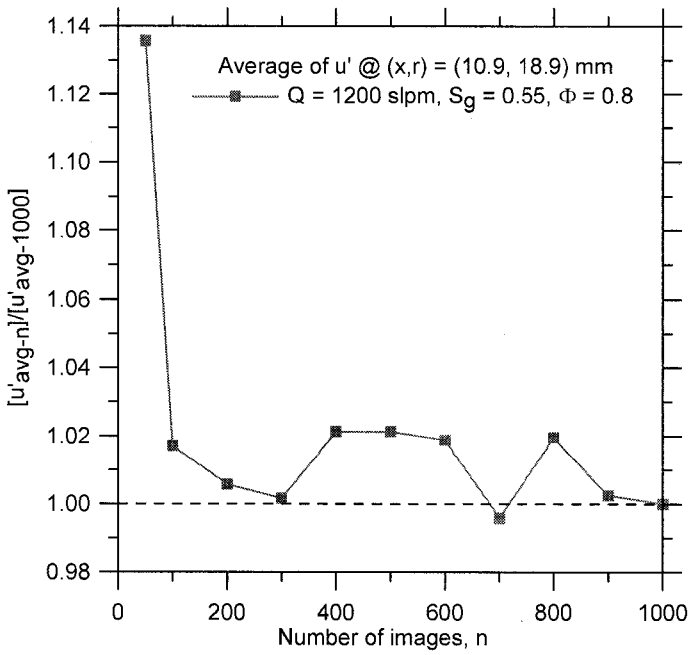

Figure E-2 Normalized average of the turbulent velocity component, u'

A measurement of the mean axial velocity component, U, was performed with hot wire anemometry, at the origin of the coordinate system. When compared with the value obtained through PIV the difference was 4%. The test conditions corresponded to non-reacting flow ($\Phi = 0$), $Q = 400$ slpm, and $S_g = 0.50$.

The average exit velocity of the burner was obtained first through the flowrates given by the flowmeters (MFCs), divided by the exit area. Then, the same velocity was calculated by integrating radially the velocity field determined by PIV and the difference was between 8 and 9%. These tests conditions corresponded to non-reacting flows ($\Phi = 0$), Q = 400, 800, and 1200 slpm, S_g = 0.55. These calculations were performed over one half of the exit plane, due to our field of view constrains.

Finally, as mentioned by Prasad [66], PIV measurements contain errors from various sources. Some of them can be minimized by selecting adequate experimentation

condition; i.e. errors due to particles that do not track adequately the flow. However, other errors are always present; i.e. by random correlations between particle images not belonging to the same pair.